THE UNIVERSITY *of* EDINBURGH

Red Supergiant Stars in the Local Group and Beyond

Lee R. Patrick

Doctor of Philosophy
The University of Edinburgh
April 2016

Summary

Red Supergiant (RSG) stars are the brightest stars at infrared wavelengths. Their intrinsic brightness combined with the fact that dust does not obscure observations at these wavelengths, makes these objects very attractive to study in the infrared. To make best use of future facilities that are specialised for these wavelengths, the tools to study RSGs must be developed today. The aim of this thesis is to further the understanding of RSGs by focusing on measuring their chemical properties in different galaxies.

To do this, I develop an analysis technique that uses observations of RSGs to estimate their properties. Using this analysis technique, I measure the chemistry and dispersal of a young cluster of stars in the Large Magellanic Cloud (LMC), one of the closest galaxies to the Milky Way. I measure the mass of the cluster using the dispersal of the stars and show that what is found is consistent with other methods. I prepare for future studies of more distant clusters by showing that if I simulate this cluster at a much larger distance, the chemical properties estimated are consistent.

Building on this, I measure the chemical properties of 11 RSGs in a dwarf irregular galaxy with a turbulent history (NGC 6822, 10 times further away than the LMC). I present weak evidence for variations in the distribution of the chemical elements in this galaxy, which requires further study. In addition, I connect the young and old star populations in this galaxy with a surprisingly simple model.

I then present observations of 22 RSGs in a large galaxy, four times more distant than NGC 6822, which is located outside of our Local Group of galaxies. I am able to rule out that the target RSGs are in binary systems and I estimate the properties of the targets using the analysis routine presented, where I find good agreement with previous studies of young stars in this galaxy.

I conclude my thesis by summarising the main results and present a first-look calibration of the relationship between two fundamental determinants of galaxy evolution: mass and chemical abundance. In addition, using ∼80 RSGs, with surface temperatures estimated in a consistent way, I show that the temperature of RSGs does not appear to depend upon their chemical properties, in disagreement with current models.

Abstract

Red Supergiant (RSG) stars are the most luminous stars in the infrared sky. Their intrinsic luminosities combined with the low dust extinction observed in this regime makes these objects very attractive to study in the near-infrared (IR). In addition, RSGs are necessarily young objects, as they are tracers of recent star formation in extra-galactic systems. As the next generation of telescopes will be optimised for study in the near-IR, it is clear that, in the coming years, RSGs will play a prominent role in the way that astronomers probe the local Universe and out to larger distances with space-based observations. Therefore, it is vital to better our understanding of these objects now and develop the tools that will allow us to take full advantage of the suite of instrumentation that will become available in the near future. This thesis aims to further the understanding of RSGs by focusing on quantitative studies of near-IR spectroscopic observations.

To this end, I develop an analysis technique that uses spectroscopic and photometric observations to estimate stellar parameters of RSGs. The observations are compared with synthetic spectra extracted from stellar model atmospheres, where departures from local thermodynamic equilibrium have been calculated for the diagnostic spectral lines. This technique is tested thoroughly on synthetic and real observations and is shown to reliably estimate stellar parameters in both regimes when compared with input parameters and previous studies respectively.

Using the analysis routines developed in Chapter 3, in Chapter 4 I measure the chemistry and kinematics of NGC 2100, a young massive cluster (YMC) of stars in the Large Magellanic Cloud, using near-IR spectroscopic observations of 14 RSGs taken with the new K-band multi-object spectrograph (KMOS). I estimate the average metallicity to be -0.43 ± 0.10 dex, which is in good agreement with previous studies. I compare the observed location of the target RSGs on the Hertzsprung–Russell diagram with that of a Solar-like metallicity YMC and show that there appears to be no significant difference in the appearance of the RSGs in these two clusters. By combining the individual RSG spectra, I create an integrated-light cluster spectrum and show that the stellar parameters estimated, using the same technique as for individual RSGs, are in good agreement with the average properties of the cluster. In addition, I measure – for the first time – an upper limit of the dynamical mass of NGC 2100 to be $15.2 \times 10^4\,\mathrm{M}_\odot$, which is consistent with the literature measurement of the photometric mass of the cluster.

In Chapter 5, I present observations of RSGs in NGC 6822, a dwarf irregular with a turbulent history, observed with KMOS. The data reduction process with KMOS is described in detail, in particular where the reduction has been optimised for the data. Stellar parameters are estimated using the technique presented in Chapter 3 and an average metallicity in NGC 6822 of -0.55 ± 0.13 dex is found, consistent with previous measurements of young stars in this galaxy. The spatial distribution of metallicity is estimated and weak evidence is found for a radial metallicity gradient, which will require follow-up observations. In addition, I show that the metallicities of the young and old populations of NGC 6822 are well explained using a simple closed-box chemical evolution model, an interesting result, as NGC 6822 is expected to have undergone significant recent interactions.

In Chapter 6, I present multi-epoch KMOS observations of 22 RSGs in the Sculptor Group galaxy NGC 55. Radial velocities are measured for the sample and are shown to be in good agreement with previous studies. Using the multi-epoch data, I find no evidence for radial velocity variables within the sample. Stellar parameters are estimated for 10 targets and are shown to be in good agreement with previous estimates.

I conclude this thesis by summarising the main results and present a first-look calibration of the relationship between galaxy mass and metallicity using RSGs. By comparing the RSG metallicity estimates to metallicities estimated from $\sim$50 000 Sloan digital sky survey galaxies, I show that the absolute metallicities of the two samples disagree. A more quantitative analysis requires additional RSG observations.

In addition, using $\sim$80 RSGs, with stellar parameters estimated in a consistent way, I show that there appears to be no dependence of the temperature of RSGs upon metallicity. This is in disagreement with current evolutionary models, which display a temperature change of $\sim$450 K over the studied range in metallicity.

Finally, I outline potential areas for future work, focusing on follow-up studies that have been identified as a result of the work done in this thesis.

Declaration

I declare that this thesis was composed by myself, that the work contained herein is my own except where explicitly stated otherwise in the text, and that this work has not been submitted for any other degree or professional qualification except as specified.

Parts of this work have been published in Patrick et al. (2015, 2016).

(*Lee R. Patrick, April 2016*)

Acknowledgements

To acknowledge the contribution of everyone who has helped me complete this thesis in the last three and a half years would, no doubt, contribute significantly to the page count of this thesis. To keep this reasonably concise, I would like to first acknowledge all of the help I've received from the people who do not have a specific mention in this section. All of the friends and work colleagues who have encouraged and spurred me on over the last few years: your contribution is not forgotten and is certainly appreciated.

I would like to thank my supervisor, Chris Evans, for providing excellent support from the outset and keeping me focused on the important tasks in hand, as well as his meticulous quality control, which have improved this thesis greatly. Throughout the course of this thesis, I have had some fantastic opportunities to go observing and attend productive conferences, which is all thanks to Chris' drive and enthusiasm. Chris has been a great supervisor and friend, always using his skills and knowledge to keep me optimistic and striving for the next result.

I would also like to thank all of my collaborators, in particular Ben Davies and Rolf-Peter Kudritzki, for their help and hard work, particularly at some strange times of the day (night, depending upon your time-zone). In addition, I would like to thank my fellow students who have provided support on a huge range of different topics, which has saved me countless time and effort.

On a personal level, I would like to thank Melanie Woodward, who has not only, made this journey of a PhD with me, but also made it so much more enjoyable. Mel has helped me celebrate the highs and helped me get back on the horse during the more trying times. However, Mel has not only contributed to this thesis on a personal level. The quality of writing in this thesis (I'm not ashamed to say) is high. I'm not ashamed to say that because it is down to the fact that Mel is an excellent editor and has spent hours studying and commenting on this thesis, improving the style, readability and flow greatly.

I would like to thank my fellow students for supporting me on a personal level. The "Golden Age" of U4, which I was lucky enough to be a part of, along with Fergus Cullen and Sandy Rogers, will live long in my memory.

Finally, I would like to thank my family who have steered me in the right direction and provided continued support throughout the years.

Contents

List of Figures

List of Tables

Chapter 1

Introduction

1.1 Shaping the Universe with Massive Stars

Understanding how stars form and evolve is fundamentally important to understanding the physical processes that govern the Universe. As congregations of stars are built up they form heavily structured galaxies where the complex internal interactions between stars and gas, as well as the underlying stellar population, are vitally important to the chemical and dynamical evolution of the galaxy (e.g. Conselice, 2014). Stars die to produce black holes and massive stars are good candidates for producing the recently observed gravitational wave signature (Abbott et al., 2016; Loeb, 2016; Woosley, 2016). Fundamentally, stars are at the heart of almost every area of study in astrophysics. From active galactic nuclei to exoplanets, solar system bodies to high-redshift galaxies; an understanding of stars and stellar evolution is vital in understanding these different phenomena.

Stars form with various masses ranging from the hydrogen fusion limit of $\sim$0.08 $M_\odot$ (Burrows et al., 1997; Chabrier & Baraffe, 2000) to an uncertain upper mass limit in excess of $\sim$100 $M_\odot$ (e.g. Figer, 2005; Eldridge, 2012; Wu et al., 2014) and up to $\sim$300 $M_\odot$ in extreme cases (Crowther et al., 2010). Massive stars (defined here as stars with initial masses $>8\,M_\odot$, e.g. Smith, 2014, and expanded upon in Section 1.2) are probably the most important type of star with respect to how they shape their surrounding environments throughout their lives and distribute chemical elements in their deaths. Massive stars drive the

ionisation of their surrounding birth cloud and are good candidates for the reionisation of the Universe (e.g. Haiman & Loeb, 1997; Ciardi & Ferrara, 2005; Fan, Carilli & Keating, 2006). During the short lifetime of a massive star (detailed in Section 1.2) massive stars material is expelled from their outer layers in strong winds at various evolutionary stages throughout their lives. These winds help to distribute nuclear processed material throughout their parent galaxies and pollute the interstellar medium (ISM) with heavy elements.

In any given star-forming galaxy, the massive star population dominates the light output across the full spectrum of light. Ultraviolet and optical light is dominated by hot massive stars (Kennicutt, 1998; Kennicutt & Evans, 2012) with temperatures of up to 50 000 K (e.g. Bestenlehner et al., 2011). In contrast, the infrared light is dominated by the cool ($\sim$4000 K) evolutionary products of these hot massive stars, i.e. red supergiant stars (RSGs), which can be as luminous as entire galaxies in the near infrared (near-IR).

Given that massive stars are extremely luminous, they can be identified in extragalactic systems at large distances. Indirectly, by ionising their surrounding birth cloud, massive stars are used to study galaxy populations at early epochs of the Universe (Pettini & Pagel, 2004). In the more local Universe, massive stars can be used to probe the structure and chemical evolution of galaxies in great detail (Evans et al., 2007; Kudritzki et al., 2008; Evans & Howarth, 2008; Kudritzki, 2010; Evans et al., 2011b; Castro et al., 2012).

In this thesis, I expand and develop the methods by which we can study massive stars (in particular RSGs) in extragalactic environments. The study of RSGs in external galaxies spans two key astrophysical topics: stellar evolution and galaxy evolution. By using RSGs as abundance probes, I have been able to map the spatial distribution of metals in external galaxies, as well as gain insight into the underlying physical principles that are used within evolutionary and atmospheric models.

In the coming years, RSGs will play a more central role in the study of extragalactic systems owing to their extreme brightness coupled with the fact that their peak luminosity is in the near-IR. Given the intrinsic advantages of reduced dust extinction in the near-IR, this is particularly poignant when considering that the next generation of ground- and space-based telescopes will be optimised for study in this wavelength regime.

1.2 The Lives of Massive Stars

Stellar evolution is critically dependent upon the initial mass of the star. A $10\,M_\odot$ star has a very different evolutionary path to that of a solar-mass star. A star's formation, subsequent evolution and eventual fate all depend upon how much mass it is able to accumulate during its formation. Therefore, an understanding of how massive stars are able to gather their mass is crucial to the understanding of how these objects evolve and end their lives. To this end, I provide an outline of the main process by which star formation occurs (focusing on massive stars) in Section 1.2.1. Section 1.2.2 describes the evolution of a massive star after the onset of hydrogen-burning in the core until the final stage of evolution before the star ends its life. This leads onto Section 1.2.3, which reviews the eventual fate of massive stars.

1.2.1 Birth

Low- and high-mass star formation occurs with giant molecular clouds (GMCs) consisting mainly of molecular hydrogen. Molecular hydrogen, to opposed to ionised hydrogen, has sufficient cooling channels to provide the correct density ($10^5\,cm^3$) and temperature (10–20 K) conditions to form stars. GMCs are regions consisting of large clumps of interstellar material that have become over-dense with respect to the surrounding interstellar medium. These clouds are typically 10^4–$10^7\,M_\odot$, extend over 50–100 pc and represent the densest parts of the interstellar medium (Fukui & Kawamura, 2010). In a high-mass molecular cloud, high- and low-mass star formation takes place. Studies suggest that, as the mass of the cloud decreases so does the mass of the largest stars (Fukui & Kawamura, 2010; Weidner, Kroupa & Bonnell, 2010); however, other studies suggest that this may not be a universal property (e.g. Bressert et al., 2012).

Within GMCs, over-dense regions continue to grow and eventually fragment into smaller cores. If these dense cores consist of a region where the local mass is greater than the associated Jeans mass for the region, the region is unstable to gravitational collapse. As the region collapses into a protostellar core, the optical depth increases, which gives rise to a large increase in temperature (Zinnecker & Yorke, 2007). The collapse proceeds until the radiation pressure exerted by the core is able to resist the gravitational collapse. The system is now in

hydrostatic equilibrium and evolution proceeds though accretion. The collapsed core accretes matter from a surrounding disk that has condensed around the protostar. Meanwhile, the core of the protostar contracts and increases the temperature of the core towards hydrogen-burning temperatures. A larger protostar can accrete a larger amount of additional material from its surroundings and in turn grows to become a more massive star. In lower mass stars, accretion ceases before the star reaches the MS; however, a more massive star can perturb a larger amount of material and hence continues to accrete matter even after the hydrogen-burning phase has begun in its core. The ignition of hydrogen ends the period of formation, as the star now has a central energy source that governs the evolution for the remainder of time spent on the main sequence (MS). However, massive stars have one more crucial role to play in the process of star formation. Massive stars end their lives as supernovae, ejecting fusion products back into the environment from which they were born. The surrounding gas is shocked and compressed by this mass ejection event, which can be the catalyst needed to produce more star formation in these environments (triggered star formation).

This is a very simplistic, qualitative overview of the formation of massive stars. In reality, the exact processes governing these main stages of formation are complicated by various factors; for example, the effect of turbulence has been completely neglected in this discussion but has a vital role in many phases of star formation (McKee & Ostriker, 2007). The relative importance of each of the processes involved is not well understood. As of yet, there is no universal theory of how star formation proceeds in massive stars.

There are several crucial differences between low- and high-mass star formation.[1] Massive stars have larger temperatures and hence produce a large amount of ionising photons. This means that the accretion disk and outer envelope surrounding the massive star is photoevaporated and dissociated through interactions with these high-energy photons. As alluded to previously, massive stars continue to accrete matter while on the hydrogen-burning MS (Zinnecker & Yorke, 2007) whereas lower mass stars ($<0.2\,M_\odot$) spend at least 10 Myr evolving towards hydrogen fusion (Luhman, 2012). A key difference in the star formation across a large mass range is the role of accretion. In lower mass star formation, accretion does not form significant amounts of the final mass of the star (Bonnell, Clark & Bate, 2008), whereas, in higher mass star formation, accretion is generally

[1]The opinion in the literature seems to suggest that low-mass star formation continues as normal until around $\sim 20\,M_\odot$ (Zinnecker & Yorke, 2007; Crowther, 2012), above this, star formation must take into account various complicating factors (see text).

accepted as playing a key role in accumulating the mass of the star (Kraus et al., 2010).

Exactly how accretion acts is subject to much debate. Accretion is likely to proceed via competitive accretion (Bonnell et al., 2001). This is where a large fraction of the star is accreted from its surrounding material. In this scenario, the amount of material available for accretion is limited only by the surrounding environment. A star at the centre of the potential well of the surrounding gas cloud will be able to accrete more material than a star on the outskirts and hence will grow larger. As the star grows larger, it is able to accrete more and more matter. Eventually, neighbouring stars will be forced to compete for the surrounding gas and, in this scenario, the largest star (i.e. the star at the centre of the potential well) will be able to accrete a larger amount of material (for a useful economical analogy – the rich get richer – see Section 4.2 of Zinnecker & Yorke, 2007). In competitive accretion theory, the mass of the star is determined entirely by the environment in which it resides and not by the initial conditions of the collapse.

Other theories of massive star formation in this context include those presented by Yorke & Sonnhalter (2002), where accretion occurs onto the protostar via a disk that is produced as a result of the monolithic collapse of the gas cloud (into the protostar). In this scenario, the mass of the star is limited to the combined total of the protostar and the accretion disk (Zinnecker & Yorke, 2007). However, this theory has difficulty explaining the observed multiplicity and clustering of massive O stars (Zinnecker & Yorke, 2007; Kennicutt & Evans, 2012; Sana et al., 2012).

An alternative path (which can explain the formation of the most massive stars) is through stellar collisions. Massive star formation can proceed through stellar collisions during the merging of star clusters, where stellar densities are highest, resulting in very massive stars concentrated at the centre of clusters (Fujii & Portegies Zwart, 2013).

1.2.2 The Circle of Life

All stars spend the majority of their active lives fusing hydrogen to helium in their cores on the hydrogen-burning MS. On the MS, all stars remain in a stable state of hydrostatic equilibrium and hence their evolution in terms of luminosity

and temperature is small (Kippenhahn, Weigert & Weiss, 2012). Once massive stars exhaust their core hydrogen fuel, various stages of nuclear burning succeed, including core helium- and carbon-burning. During this evolution, the surface temperature decreases and stars appear increasingly redder at later stages of their evolution. This evolution is typically characterised on a Hertzsprung–Russell (H-R) diagram, which relates the surface temperature and luminosity of a star and can be used to illustrate how the appearance of stars change throughout their lives. Figure 1.1 displays a H-R diagram that shows stellar evolutionary models of stars of various masses in black lines. Initial masses (in Solar units) of some of the important distinctions in stellar evolution are labelled at the start of their respective models. The $7\,M_{\odot}$ evolutionary model is labelled with five red points indicating important transitions in its evolution. Each model begins at the onset of hydrogen fusion within the core of the star (point 1) and when viewed in comparison with other models, at different initial masses, forms the MS of stellar evolution. Once stars exhaust their fuel in the core they cool and evolve off the MS (towards the right in Figure 1.1) and depending upon their masses, go on to fuse heavier elements in their cores. The models shown in Figure 1.1 end at the exhaustion of carbon burning in the core (if applicable; point 5).

During core hydrogen-burning, stars more massive than $1.1\,M_{\odot}$ fuse hydrogen to helium through the carbon–nitrogen–oxygen (CNO) cycle. In this case, convection is induced in the core owing to the large temperature gradient established as a result of the high temperature dependence of the rate of the CNO cycle (T^{14}). As a result of convective mixing, the core can be described as homogeneous during the hydrogen-burning phase (Kippenhahn, Weigert & Weiss, 2012). Convection is an important feature of this stage of evolution, because it increases the MS lifetime as more material is available for fusion.

Some of the main issues with the current theory of convection are characterising the size of the convective overshoot region and the effects of semi-convection on stellar evolution. Convective overshooting acts to increase the mixing of material beyond the convective boundary, within a stable region. As a convective cell is accelerated towards the boundary of the convective layer, its momentum carries the cell beyond this region into a region of convective stability. This has several consequences for the evolution of the hydrogen-burning phase, which are direct results of convective overshooting increasing the amount of fuel available for consumption within the convective core. How large an evolutionary effect convective overshooting produces is not well constrained.

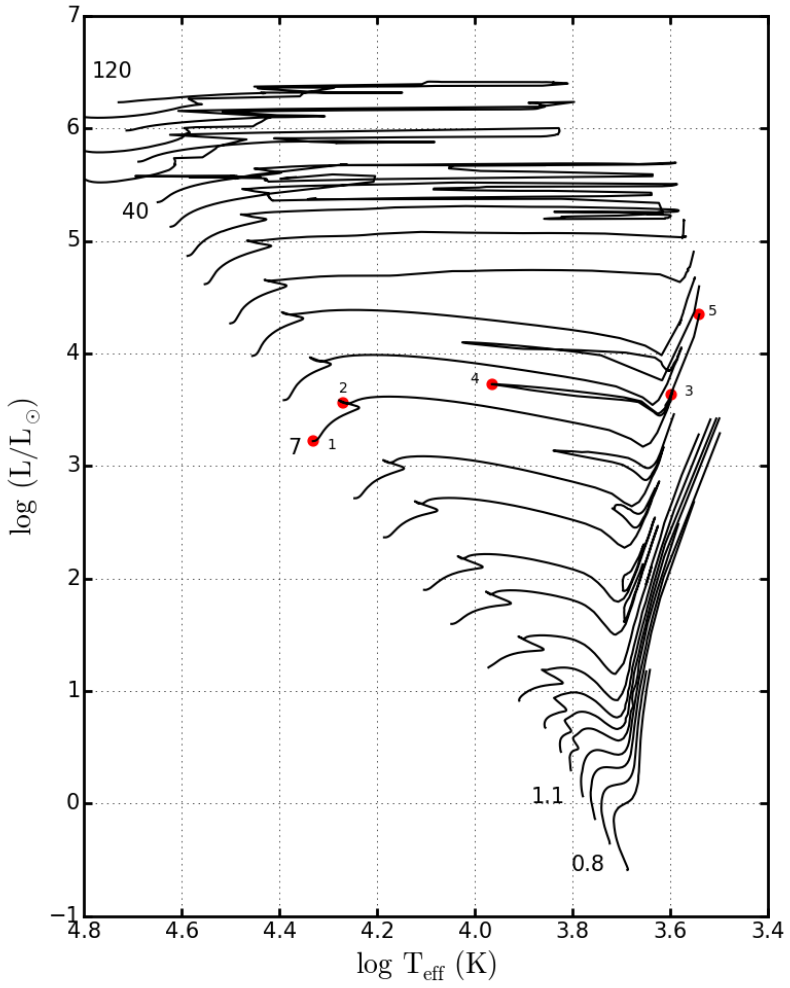

Figure 1.1 *Hertzsprung–Russell (H-R) diagram displaying the surface temperature (increasing to the left) against luminosity of stellar evolutionary models in the mass range $0.8 < M/M_\odot < 120$, using evolutionary models from Ekström et al. (2012). Each line represents a model at Solar-like metallicity computed without stellar rotation. Initial masses of some important transition regions are given to the left (i.e. the start) of the models. Red points on the $7 M_\odot$ track mark important changes within a stars lifetime: 1. onset of hydrogen fusion (start of model), 2. exhaustion of fuel in the core, 3. onset of helium core fusion, 4. blue loop, 5. end of core carbon fusion (end of model). Stars spend most of their lives on the left of this diagram on what is commonly known as the main sequence of stellar evolution. After exhausting the hydrogen fuel in the core, the star becomes more extended and hence cools and is said to appear "redder" (towards the right of the diagram). See text for more details on these phases of evolution.*

Convective overshooting is characterised by the parameter α in units of the local pressure scale height (H_P) (Kippenhahn, Weigert & Weiss, 2012). Various authors have placed constraints upon α by using observational techniques including, for example, measuring the width of the MS (Schroder, Pols & Eggleton, 1997; Brott et al., 2011). These studies find values of $\alpha = 0.1$–0.6 (e.g. Brott et al., 2011, who found $\alpha = 0.335$).

In addition to the uncertainties surrounding the convective overshooting problem, as the opacity in massive stars is dominated by electron scattering (Böhm-Vitense, 1992), outside a fully convective core, semi-convection occurs. Semi-convection is a discrepancy between the two criteria for convection outside a fully convective zone where a chemical gradient (∇_μ) is established. Semi-convection acts to smooth out the chemical gradient outside the fully convective regions and can determine how the star evolves and ends its life after this phase (e.g. Langer, El Eid & Baraffe, 1989).

As the star evolves and more hydrogen is consumed, the mass of the convective core decreases (Kippenhahn, Weigert & Weiss, 2012). Eventually, the star consists of a pure helium core surrounded by a hydrogen-burning shell. The maximum mass of the helium core, with respect to the total stellar mass is determined by the Schönberg–Chandrasekhar (SC) limit ($q_{SC} \geq \frac{M_c}{M_{tot}}$; usually derived as $q_{SC} \sim 0.1$), above which an inert helium core is unstable to gravitational collapse. In stars in the mass range $3 < M/M_\odot < 12$, the SC limit is usually reached at the end of the hydrogen-burning phase (point 2 in Figure 1.1; Salaris & Cassisi, 2005). At this point, the helium core collapses, increasing the core temperature and density sufficiently that core helium-burning can occur, halting the collapse in the process. In more massive stars ($>12\,M_\odot$), core helium-burning can smoothly proceed without the need for core collapse, as the central temperature in these stars is sufficiently high (10^8 K).

During this phase of evolution, hydrogen-burning proceeds within a shell outside the core. For stars that exceed the SC limit during core contraction the outer hydrogen envelope will expand owing to the "mirror principle" of shell fusion (e.g. Ball, Tout & Żytkow, 2012).[2] As the outer envelope expands, the effective temperature decreases. In Figure 1.1, the star moves to the right (towards redder colours), where massive stars evolve into the RSG phase and lower mass stars evolve onto red giant branch stars. This phase of evolution proceeds on a Kelvin–

[2]This principle is not well understood, but its effects appear to be a universal feature of shell fusion (Sugimoto & Fujimoto, 2000; Stancliffe et al., 2009; Ball, Tout & Żytkow, 2012).

Helmholtz timescale, which for a $7\,M_\odot$ star is around 5×10^5 yr (Kippenhahn, Weigert & Weiss, 2012), i.e. incredibly short on an evolutionary timescale. For stars above $8\,M_\odot$, the evolution towards the red is halted as core helium-burning switches on (point 3 in Figure 1.1).

Lower mass stars evolve onto the red giant branch during core collapse and their redward evolution is halted by the Hayashi limit, which is a limit on the temperature of a fully convective star. These stars then evolve up the Hayashi limit, increasing their luminosity until the core contracts sufficiently that helium ignites in a degenerate core creating a thermonuclear runaway reaction. Once the core helium has been ignited, the degeneracy in the core is lifted and the star evolves onto the Horizontal Branch where core helium fusion occurs. As the core helium is depleted the star evolves onto the asymptotic giant branch (AGB) where the luminosity is increased significantly. The main source of energy is now either the helium fusing shell (early AGB stars) or, later, the hydrogen fusing shell (thermally pulsing AGB stars).

For stars with masses between $8 < M/M_\odot < 12$, the contraction of the inert helium core heats the core sufficiently that helium fusion is ignited surrounded by a hydrogen fusing shell. The new energy source then causes an expansion in the core that, owing to the mirror principle of shell fusion, results in the contraction of the outer envelope towards higher temperatures. This is the beginning of the so-called "blue loop" phase of evolution, which is depicted between points 3 to 4 in Figure 1.1.

The blueward evolution is halted when an inert carbon core is established as a result of helium fusion. As the star now has no energy source in the core, the core contracts, resulting in the expansion of the outer envelope (again owing to the mirror principle) and the star moves from point 4 to 5 in Figure 1.1. This process may repeat for each new energy source within the core. The appearance of blue loops in stellar evolutionary models depends critically on the treatment of convection and of the chemical composition of the star(among other factors; see Chapter 31 of Kippenhahn, Weigert & Weiss, 2012).

The blue loop phase of evolution is important as, during this period, the star crosses the "instability strip" of the H-R diagram on an observable timescale. Stars on the instability strip are vibrationally unstable and pulsate as their radii and luminosities periodically change. Stars in this phase of evolution can be used as a direct test of stellar evolution where the most massive examples of

pulsationally unstable stars are the Cepheid variables, which have masses up to $\sim$20 $M_\odot$ (Ekström et al., 2012, and references therein). Stars above this limit do not become Cepheid variables.

In massive stars above 12 $M_\odot$, core helium-burning is thought to ignite when the star appears as a blue supergiant (BSG) (Meynet et al., 2011; Ekström et al., 2012; Langer, 2012; Saio, Georgy & Meynet, 2013). The redward migration of BSG stars is dictated by an intermediate convective zone (Meynet et al., 2011) present in the atmosphere of the star, and is more gradual than the redward evolution of less massive stars.

Stars more massive than around 40 $M_\odot$ never become RSGs (Massey, 2003; Meynet et al., 2011; Ekström et al., 2012) and, hence, there is a peak luminosity of RSGs in any given population (Humphreys & Davidson, 1979). As these massive stars evolve towards the red edge of the H-R diagram, their luminosities approach that of their Eddington luminosities; this induces large mass-loss episodes. As a result, these stars halt their evolution towards the RSG phase and evolve towards the blue and consequently into Wolf–Rayet (WR) stars (Crowther, 2007; Vink, 2009), see 60 $M_\odot$ track and above in Figure 1.1.

As suggested above, in specific cases, not all of the helium-burning phase is spent as a RSG. The length of time spent during the RSG phase depends upon how core helium-burning ignites. If a star begins its helium-burning lifetime as a BSG and subsequently evolves into the RSG phase, naturally, the length of time spent as a RSG will be shorter. In addition to this, stars with masses in the range of $25 < M/M_\odot < 40$ are thought to evolve back from the RSG phase to the BSG phase while still burning helium in their cores (Ekström et al., 2012).

This evolution of massive stars between the BSG and RSG phase seeds the idea that stars in these stages of evolution will fall into two categories:

i stars that begin helium-burning in the RSG or BSG phase, or

ii stars that begin helium-burning in a different evolutionary state and have since evolved into either the RSG or the BSG regime.

Distinguishing these objects observationally is challenging. Saio, Georgy & Meynet (2013) used radial pulsations to distinguish between models of BSGs, which "roughly agree" with observations of NGC 300 and in the Galaxy. However,

an analogue to this has not been identified in RSGs. Castro et al. (2012) argued, based on the nitrogen enrichment of their population of observed BSGs, that these stars are in the process of evolving towards a RSG phase. The ratio of BSG to RSG is used as a test of stellar evolutionary models which has been an issue for some time (Langer & Maeder, 1995) and is known to be affected by rotation (Maeder & Meynet, 2001; Ekström et al., 2012) and binarity (Eldridge, Izzard & Tout, 2008).

Regardless of how extended the external envelopes in these stars are, core helium-burning proceeds through the triple alpha process, via the reaction $3\alpha \rightarrow {}^{12}\mathrm{C} + \gamma$. However, as the number density of ^{12}C increases, the reaction $^{12}\mathrm{C}(\alpha+\gamma)^{16}\mathrm{O}$ is of increasing importance, although the exact rates at which these reactions proceed is not well constrained. This process of nuclear burning is highly temperature sensitive (even more so than the CNO cycle); therefore, convection within the core is once again established. In addition to this, massive red helium-burning stars also have large outer convective envelopes (Kippenhahn, Weigert & Weiss, 2012) and, as a result of this, the star appears near the Hayashi limit for a fully convective star in the H-R diagram. The Hayashi limit is a limit on the coolest surface temperature a star can have, as beyond this, the star is no longer in hydrostatic equilibrium (Hayashi & Hoshi, 1961). The convective envelope dominates the evolution of all but the most massive RSGs ($30 < \mathrm{M/M_\odot} < 40$), which do not not appear as close to the Hayashi limit as their lower mass counterparts (see Figure 1 in Saio, Georgy & Meynet, 2013).

At the end of the core helium-burning phase, a massive star contains a carbon/oxygen core surrounded by a helium-burning shell, which is in turn surrounded by a hydrogen-burning shell. At this point, the situation in the core now resembles that of the stage before core helium-burning. An inert carbon/oxygen core contracts and heats up, which ignites the core fuel. Stars with initial masses greater than around $8\,\mathrm{M_\odot}$ are able to fuse carbon in their cores in a stable fashion. In order for lower-mass stars to do so, a degenerate carbon core is required. Whether or not stars are able to begin core carbon-burning in a stable manner is usually the physical basis for distinguishing between intermediate- and high-mass stars. During this process, carbon fuses to form an unstable form of ^{24}Mg which then decays through three channels:

i $^{24}\mathrm{Mg}^* \rightarrow {}^{23}\mathrm{Mg} + n + \gamma$,

ii $^{24}\mathrm{Mg}^* \rightarrow {}^{20}\mathrm{Ne} + \alpha + \gamma$,

iii $^{24}\mathrm{Mg}^{*} \rightarrow\ ^{23}\mathrm{Na} + p + \gamma$.

Oxygen does not fuse at this stage of the evolution of the star and, therefore, the length of time a star spends fusing carbon depends strongly on the amount of carbon processing present in the helium-burning phase and, hence, the reaction $^{12}\mathrm{C}(\alpha + \gamma)^{16}\mathrm{O}$.

Once the carbon fuel has been exhausted in the core, shell carbon-burning proceeds. The cycle of core contraction with new core reactants begins and subsequent neon-, oxygen- and silicon-burning phases follow in the core (Woosley, Heger & Weaver, 2002). As each new fuel in the core is exhausted, shell burning follows. Fusion reactions cease with ^{56}Fe as fusion reactions beyond this point are no longer energetically favourable.

Eventually, this leads to an "onion structure" star, with an inert iron core surrounded by layers of lighter elements fusing in shells. These fusion reactions proceed on such a short timescale that the outer envelope does not have the time to react to the changing conditions in the core. This effectively "freezes out" the outer envelope and the spectral type of the star does not change significantly during this period (Meynet et al., 2011).

1.2.3 Death

Massive stars ($>8\,\mathrm{M}_{\odot}$) end their lives as core-collapse supernovae (CCSN). These violent explosions distribute elements synthesised within massive stars during their nuclear-burning lifetime, in addition to the material synthesised during the explosion event. Observationally, CCSN are broadly classed as type II, type Ib and type Ic based on the presence (II) or absence (I) of H in their spectra.[3] This classification is purely observational rather than as the result of an underlying physical distinction.

There are several different types of CCSN that occur as a result of the different conditions present in the cores of massive stars; for an in depth review, see Janka (2012). Massive stars produce SNe through four main CCSN channels: electron-capture SNe, iron-core SNe, gamma-ray burst SNe and pair-instability SNe. Different products of stellar evolution produce different types of CCSN. Iron-core

[3]Type Ib and type Ic are often grouped as type Ibc, as the differences between these two types are difficult to distinguish see, for example, Eldridge et al. (2013).

SNe accounts for the majority of observed CCSN (Smartt, 2009; Janka, 2012; Eldridge et al., 2013; Smith, 2014) and are thought to be produced by RSGs in the mass range 8–20 $M_\odot$ (Poelarends et al., 2008; Smartt, 2009).

As mentioned in the previous section, massive stars conclude their nuclear-burning lifetimes with inert iron cores. Owing to a lack of energy generation, the core contracts and heats up. As the temperature reaches 10^{10}K, photons in the core of the star now have enough energy to photo-dissociate iron-group elements into α particles. The increasing density forces electrons into nuclei which merge with protons to create a neutron-rich environment. As densities approach nuclear density, core contraction halts as a result of the repulsive force of the strong interaction (Janka, 2012). The in-falling outer layers crash into the core and the resulting shockwave disrupts the entire star and produces the SN.

The exact mechanism that produces the SN explosion is subject to intense research, the subtleties of which will not be detailed here. For more details, see, for example Janka (2012), Burrows (2013) and Foglizzo et al. (2015).

In recent years, many SN progenitors have been discovered by reviewing extensive archival data available in the Local Volume as well as through extensive dedicated SN surveys. These studies (or a quick review of the Central Bureau for Astronomical Telegrams list of SNe[4]) reveal that type II-P SNe are by far the most numerous type of CCSN ($\sim$ 60%) and RSG stars are firmly established as their progenitors (Smartt, 2009, and references therein). However, CCSN are observed in a variety of different types and, hence, RSGs are not the only type of massive star that end their lives as SNe. Figure 1.2 illustrates the many possible channels towards SNe; this includes RSGs, BSG and WRs. In addition, luminous blue variable (LBV) stars are being established as a part of this list (e.g. Smartt, 2009; Groh, Meynet & Ekström, 2013).

1.3 Observations of RSGs at Home and Abroad

RSGs are massive, bright, evolved stars located in recent star-forming environments. As mentioned above, any star with an initial mass $8 < M/M_\odot < 40$ is expected to spend a portion of its life cycle as a RSG (Meynet & Maeder, 2000; Massey, 2003; Crowther, 2007; Meynet et al., 2011). As RSGs are so luminous,

[4]http://www.cbat.eps.harvard.edu/iau/cbat.html

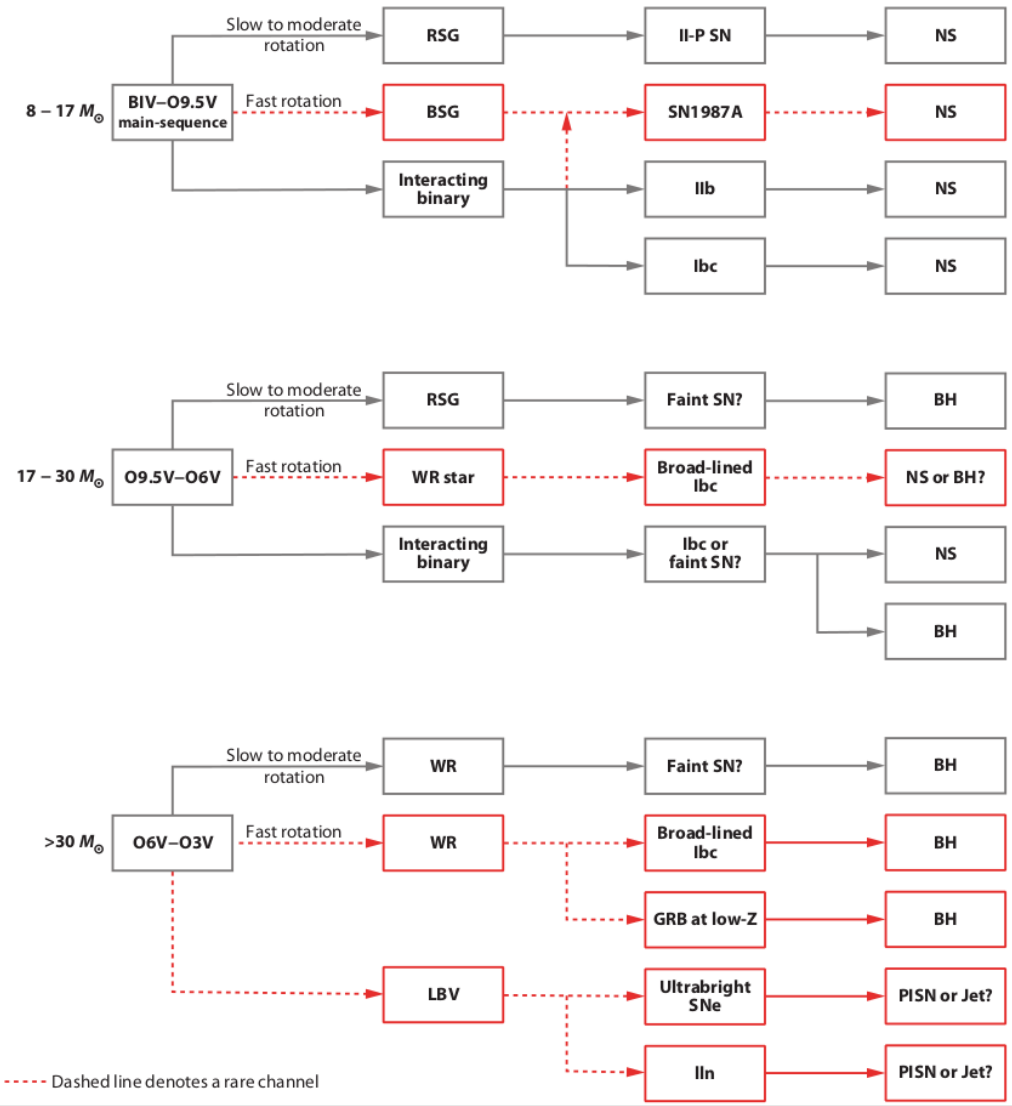

Figure 1.2 *The evolutionary diversity of the end points of massive stars and their associated observed supernova classification. Figure reproduced from Smartt (2009). Acronym definitions: RSG, red supergiant; BSG, blue supergiant; LBV, luminous blue variable; WR, Wolf–Rayet; NS, neutron star; BH, black hole; GRB, gamma-ray burst; PISN, pair-instability supernova. Note that, in Smartt (2009) and hence in this illustration, the upper-mass limit of a star that becomes a RSG is 30 $M_\odot$ rather than the 40 $M_\odot$ adopted here.*

these objects can be studied in external star-forming galaxies supplemented of course by more detailed studies of individual stars within our own Galaxy. However, before one can study RSGs, they need to be accurately identified and classified. In Section 1.3.1, I deal with how this can be achieved and then highlight some of the key observational results from Galactic and extragalactic studies of RSGs in Section 1.3.2.

1.3.1 Identification and Classification of RSGs

The classification of stars is based on the morphology of their optical spectra, with particular focus on the absorption lines of hydrogen and other elemental features such as helium and calcium. RSG stars have spectral type K or M, classified as such based on the appearance of strong molecular lines arising from their cool atmospheres. Additionally, cool MS dwarfs and evolved giant stars also have spectral type K or M. To distinguish between these populations of stars, luminosity is taken into account. The luminosity of a star (L) is given by the following equation (which in Chapter 3 is defined as one of the fundamental equations of a star):

$$L = 4\pi R^2 \sigma_{SB} T_{\rm eff}^4, \tag{1.1}$$

where R is the radius of the star, $T_{\rm eff}$ is the effective temperature of the star and σ_{SB} is the Stefan–Boltzmann constant.

For a given spectral type, the effective temperature of a star is roughly constant; therefore, luminosity is dependent solely upon the radius of the star. The largest and most luminous stars, the supergiants, are labelled as class I, giants as class III and dwarf or MS stars, with the smallest radii and hence the lowest luminosity, as class V.

In general, spectral features that are sensitive to luminosity are directly related to the physical size of the star rather than a product of the luminosity. Supergiants have large extended atmospheres; hence, their radii are considerably larger than the more compact dwarfs and giants. This distinction in physical size of stars results in various characteristic spectral features, which are used to determine luminosity class. In the optical regime, there are various different luminosity class indicators. For K-type stars, the ratio of the Y II (4376 Å) line with Fe I

(4383 Å) or the morphology of the Ca II H and K lines (for early K-type stars), are some of the most prominent (Gray & Corbally, 2009). While, for M-type stars, a system of molecular TiO bands centred on 5000 Å or the negative luminosity effect of the Ca I (4226 Å) line are clear indicators of luminosity (Gray & Corbally, 2009). In the infrared, the 0–0 band of the CN molecule is the main luminosity discriminator at $\sim$1.1 μm for both K- and M-type stars (Gray & Corbally, 2009).

Distinguishing between dwarfs, giants and supergiants for a given spectral type is important, as these stars are different in terms of their stage of evolution and mass. RSG stars are young, evolved stars that are fusing helium or heavier elements in their cores. In contrast, dwarf M- and K-type stars are low-mass stars that are still in the core hydrogen fusion stage. Giant M- and K-type stars are evolved stars of various masses and ages currently on the red giant branch. The exact divide between AGB stars, the youngest and most luminous type of red giant star, and RSG stars is – like all classification sequences that attempt to bin a continuous range of data – somewhat ambiguous and great care must be taken to separate these classes of stars.

The most effective method of classifying stars is to obtain spectroscopic observations that cover some of the important diagnostic luminosity indicators, with sufficient resolution to distinguish between unique observational signatures. In the optical regime, RSGs spectra are dominated by absorption from TiO, which can be seen in all the M- and K-type spectra (illustrated in Figure 1.3). However, spectroscopic observations are expensive. In the absence of spectroscopic observations, the selection of stars, in general, is made based on broad band photometry. Isolating a population of stars using photometric selection techniques is important, as photometry can target a large number of stars with a relatively small amount of observing time, which can be used to optimise follow-up observing programmes to target specific types of stars.

Colour–magnitude diagrams (CMDs), which are essentially an observational form of the H-R diagram, are often used to isolate particular types of stars. Colour is defined as the difference between two magnitudes at different wavelengths. Essentially, a colour traces the shape of the spectrum of the star (which is defined to first order by the effective temperature), and the brightness of a star in a given filter (magnitude) can be used to approximate luminosity. Therefore, theoretically, a CMD should allow for the separation of a population of stars with distinct luminosities and temperatures in the same way as a H-R diagram. The situation is simplified in the case of the RSGs, as these stars are expected to be

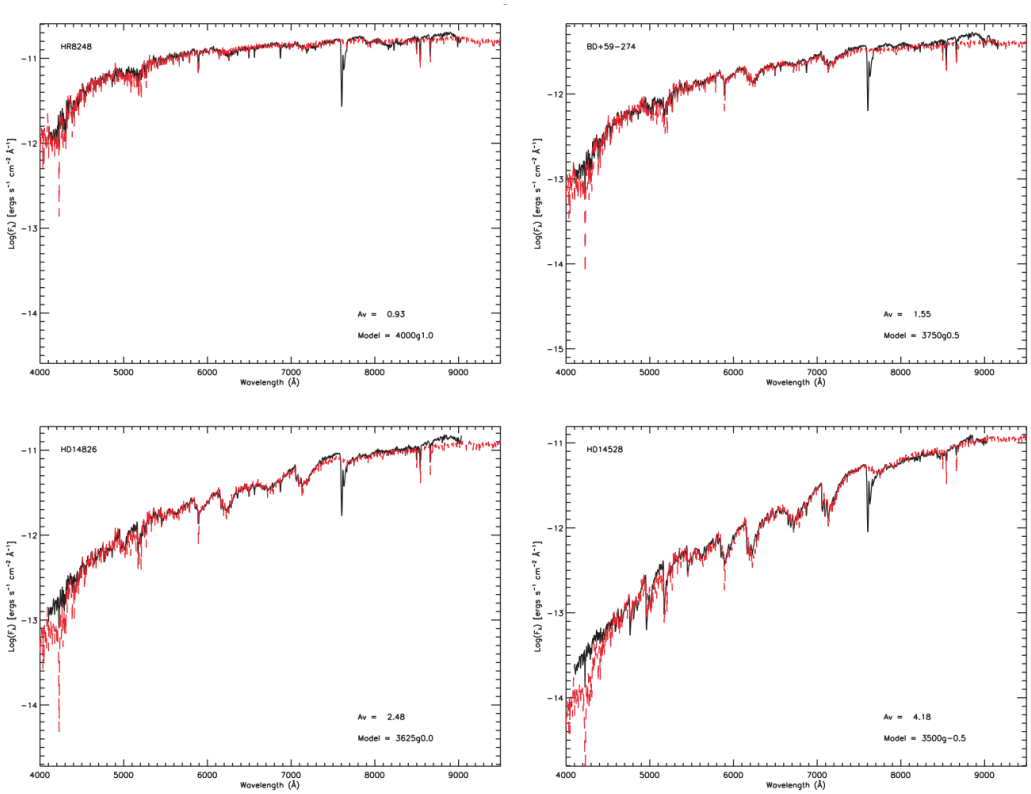

Figure 1.3 *Optical spectra of four Galactic RSGs from Levesque et al. (2005), with wavelength in Ångstrom on the abscissa shown against the logarithm of observed flux on the ordinate, illustrating that these spectra are dominated by the broad absorption from the TiO molecule. Observed spectra are shown in black with an associated best-fit model spectrum in red. The A_V value shown in each figure refers to the amount of "reddening" applied to each model spectrum to fit the observations and the number below this indicates the best-fit model effective temperature in Kelvin and the logarithm of the surface gravity in c.g.s. units. (For a discussion on how this apparent change in temperature in the optical is related to the appearance of the TiO features in optical spectra of RSGs, see Chapter 5.) The four panels shown here demonstrate the varying appearance of the TiO features present in RSGs, from top to bottom, left to right: HR 8248 (K1 I), BD +59°274 (M1 I), HD 14826 (M2 I) and HD 14528 (M4.5 I).*

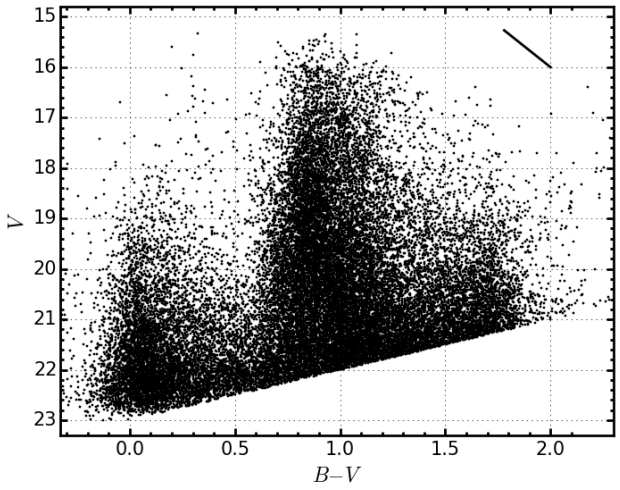

Figure 1.4 *Optical colour–magnitude diagram (CMD) of NGC 6822, in which the apparent V-band magnitude V, is plotted against $B-V$ colour. This figure illustrates how CMDs can be used to separate stars based on spectral type. Redder colours generally indicate later spectral types (however, these colours can be strongly affected by interstellar and circumstellar extinction). This figure also demonstrates that CMDs have inherent degeneracies between different populations of stars.*

among the brightest in a stellar population. However, this method assumes that the sample consists purely of one population of stars at a fixed distance. When a population of stars is distributed over a significant range of distances, a brighter star with a larger distance is degenerate with a nearby fainter star. In addition, dust extinction can affect the colours of stars, which can cause a star with a bluer colour that is significantly extincted by dust to appear as a redder star with a smaller contribution from extinction.

An example of an optical CMD is given in Figure 1.4, which shows photometry the dwarf irregular galaxy NGC 6822 (at a distance of 0.46 Mpc; this galaxy is discussed in detail in Chapter 5). In this figure one can see large-scale structures arising as different types of stars distinguish themselves based on their properties. However, this figure also demonstrates some of the potential issues with using these types of diagrams to select targets. The large feature at $B-V \sim 1.0$ is attributed to foreground contaminants. RSGs are found on this figure at the tip of the reddest plume with $B-V > 1.5$.

To break the degeneracy between luminosity and distance as well as distance and reddening, one can use colour–colour diagrams (CCDs; not to be confused

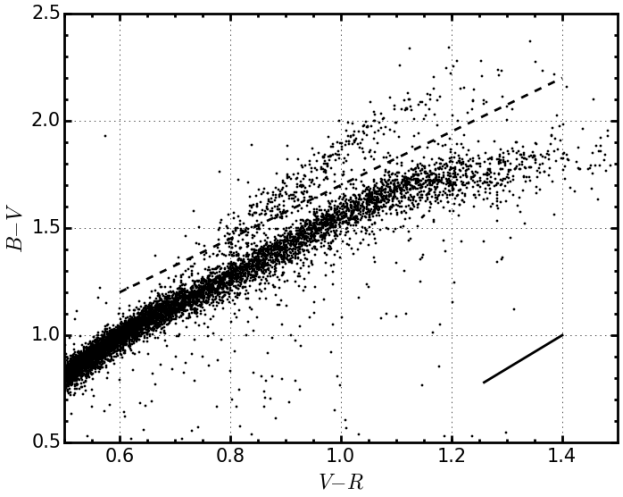

Figure 1.5 *Optical colour–colour diagram of NGC 6822. This figure illustrates the surface gravity dependence of the $B-V$ colour at a given $V-R$ colour. The dashed line separates the population of RSGs (above the line) from stars with similar spectral types.*

with charged coupled device that uses the same acronym). The use of multiple colour diagnostics can isolate stars to a greater degree than CMDs. Massey (1998) showed, that, at a given $V-R$ colour, the $B-V$ colour of a star is sensitive to the surface gravity. Therefore, RSGs can be isolated from other stars of similar $B-V$ colours owing to their low surface gravity. An example of such a CCD is shown, again for NGC 6822, in Figure 1.5, where one can clearly see the distinction between low surface gravity RSGs (with slightly redder $B-V$ colours) and the high surface gravity foreground dwarf stars.

The selection of RSGs is typically done using a $B-V$, $V-R$ CCD, as this diagram has had much success in selecting RSGs and is known to contain a small number of contaminants (e.g. Massey, 1998; Massey & Olsen, 2003; Levesque et al., 2005, 2006; Levesque & Massey, 2012; Patrick et al., 2015). However, a potential issue with this method in extragalactic systems is that RSGs are known to reside in dense regions and/or clusters with many bluer, younger stars. When viewing these stars in the optical, the colours from RSGs could potentially be contaminated to bluer colours by the blue stars that also reside nearby. In a $B-V$, $V-R$ diagram, this contamination would affect the completeness of the population of RSGs selected. A potential solution to this problem would be to select RSGs based on their near-IR colours, which is where these stars are brightest and hence would be less subject to contamination to nearby blue objects.

Working in the near-IR, authors have used the J, $J-K$ CMD (e.g. Nikolaev & Weinberg, 2000; Cioni et al., 2006; Neugent et al., 2012; Patrick et al., 2015) as well as the psuedo-colour $Q = (J-H) - 1.8 \times (H-K)$ (e.g. Comerón & Pasquali, 2005; Clark et al., 2009; Negueruela et al., 2010, 2011; González-Fernández & Negueruela, 2012; Messineo et al., 2012; González-Fernández et al., 2015), which is not affected by interstellar extinction, to select RSG and red giant stars and much work has been done in identifying contaminants and developing the parameter space in which these populations reside.

In the mid-IR, authors have used the $[3.6] - [4.5]$ CMD to distinguish between RSGs and various types of red giant stars (Blum et al., 2006; Britavskiy et al., 2014, 2015; Boyer et al., 2015; Williams et al., 2015) and using these longer wavelengths has proved a useful tool to study the dust properties of these cool stars (Beasor & Davies, 2016).

1.3.2 Galactic and Extragalactic Studies

The intrinsic brightness of RSGs, particularly in the near-IR, makes these stars popular candidates for observations within and without the Galaxy. Studies of Galactic RSGs are used to test theories of stellar evolution and estimate fundamental stellar parameters such as radii, masses and distances. Galactic RSGs are also a natural starting point for extragalactic studies of larger populations of RSGs. Extragalactic observations have identified populations of RSG stars in a large range of galaxies within the Local Group and (in rarer cases) out to larger distances (e.g. Elias, Frogel & Humphreys, 1985; Humphreys & Graham, 1986; Massey et al., 2006, 2007; Groenewegen et al., 2009; Massey, 2013; Gazak et al., 2015, and see Chapter 6). These studies provide important results on RSGs in different environments.

RSGs are intrinsically rare within stellar populations given that the initial mass function of galaxies naturally produces fewer high mass stars and the consequently short lifetimes high masses imply. Within the Galaxy, there are examples of prominent individual RSGs such as α Orionis (Betelgeuse), VY Canis Majoris and Antares, which have gained considerable attention for countless years.[5] In addition to individual RSGs, there are examples of Galactic (and extragalactic) young massive clusters (YMCs) whose light output is dominated by RSGs and

[5]Rappenglück (2003) suggested that cave markings in Germany dating to around 30 000 BCE represented the constellation Orion, of which Betelgeuse is part.

contain tens of these objects (Gazak et al., 2014b). Examples include the h and χ double cluster and more recently discovered clusters such as RSG clusters 1, 2 and 3 and Alicante 8 (RSGC01, RSGC02, RSGC03; Figer et al., 2006; Davies, B. et al., 2007; Clark et al., 2009 respectively; Negueruela et al., 2010) each containing a large concentration of RSGs.

Research into individual Galactic RSGs typically is concentrated on estimating structural or dynamical properties of atmospheres or on circumstellar material surrounding these stars, where one can test detailed stellar evolutionary and atmospheric models against high-quality observations (e.g. Clark, Negueruela & González-Fernández, 2014). A useful reference to obtain an overview of what research is being conducted on individual RSGs in the Galaxy is Kervella, Le Bertre & Perrin (2013), namely, the conference proceedings for an entire workshop centred on Betelgeuse.

Observations of Galactic RSGs reveal that they have large mass-loss rates ($10^{-(6\pm1)}\,\mathrm{M_\odot\,yr^{-1}}$; Danchi et al., 1994; Richards, 2013; Shenoy et al., 2016) and extended circumstellar environments (Smith et al., 2001; Wright et al., 2014), which may contain masers (e.g. Schuster, Humphreys & Marengo, 2006; Zhang et al., 2012). Mass loss during this phase of evolution is critical for the understanding of subsequent evolutionary stages as well as understanding SN progenitors. For example, the remnant of SN 1987A displays loops, which are thought to have originated in mass loss events during the RSG phase of evolution of its progenitor star (Humphreys, 2013, and references therein). Galactic RSGs act as an important sample to study and understand the mechanisms and rates of mass loss, as extragalactic observations are unable to resolve the structures that can be seen in nearby Galactic stars.

One of the main uncertainties with studies of Galactic stars is the relatively poorly constrained distances, e.g. Betelgeuse ($197 \pm 45\,\mathrm{pc}$; Harper, Brown & Guinan, 2008) and VY CMa ($\sim 1300 \pm 120\,\mathrm{pc}$; Wittkowski et al., 2012; Zhang et al., 2012), which are partly attributed to variations of surface structure affecting the stellar photocentre (Chiavassa et al., 2011). However, this effect is likely to be on the 0.1 AU scale and cannot account sufficiently for the large error in the distance determination. In order to (partially) remove the distance uncertainty problem, RSGs can be observed in Galactic clusters of known distances (e.g. Humphreys, 1978; Mel'Nik & Efremov, 1995; Gazak et al., 2014b). This technique is useful to study large populations of RSGs, which can be used to test theories of star formation and models of RSGs and their atmospheres.

Extragalactic studies of RSGs have the advantage that it is possible to accumulate large samples of RSGs, at a fixed distance, with which to test stellar evolution theories and estimate stellar parameters. By using the different environments available in the Local Group, studies of extragalactic RSGs can probe a wide range of host galaxy parameter space. For example, M31 ($Z > 1.0Z_{\odot}$ in the central regions), a massive, metal-rich spiral galaxy, and the Wolf–Lundmark–Melotte (WLM; $Z = 0.1Z_{\odot}$), a dwarf irregular, metal-poor galaxy, both contain a significant population of RSGs.

Through an analysis of RSGs in different metallicity environments, some authors have reported that the average spectral type of a RSG population is dependent upon metallicity (Elias, Frogel & Humphreys, 1985; Massey & Olsen, 2003; Levesque & Massey, 2012), where lower metal abundances give rise to earlier average spectral types. In addition to this, RSGs can be used to measure abundances in Local Group galaxies, which yield important results by mapping metallicity gradients. This work had typically been done using high-resolution spectra at near-IR wavelengths (Cunha et al., 2007; Davies et al., 2009a,b). However, in order to optimise these studies, Davies, Kudritzki & Figer (2010) adapted a method for determining the chemical properties of BSG stars in the optical (Kudritzki et al., 2008; Kudritzki, 2010), to RSGs in the near-IR.

These studies exploit the fact that, even though RSGs are evolved objects, for massive stars, the hydrogen-burning lifetime is short (just over 25 Myr for a $8\,M_{\odot}$ star and consequently shorter for higher-mass stars; Ekström et al., 2012). Therefore, RSGs are in actual fact still remarkably young stellar objects (<30 Myr old, as subsequent generations of nuclear fusion are significantly shorter than the time scale for hydrogen fusion). Given the fact that these stars are very young, in general, they have not had the time to travel a significant distance from their birth place. Therefore, their chemical composition must closely match that of their surrounding environment. This means that studies of RSGs in extragalactic environments can probe the present day metallicities of their surrounding environments, which are comparable to H II region studies (see Section 1.4).

In addition to their young ages, RSGs are also intrinsically attractive objects to study at near-IR wavelengths. From a technological point of view, the next generation of optical-infrared telescopes (e.g. European Extremely Large Telescope, Thirty Metre Telescope, James Webb Space Telescope) will be optimised for studies in the near-IR; therefore, in order to make the best use

of these facilities in the future, we must refine and optimise our observational strategy on facilities today.

There are also many intrinsic properties of RSGs that make them desirable objects to study in the near-IR. As noted earlier, RSGs are among the most luminous objects in any star-forming galaxies and, given their cool atmospheres, the peak luminosity for RSGs is $\sim$1.1 μm. Coupled with this is the fact that near-IR observations are less affected by dust obscuration, which is important, as by definition, RSGs are dusty objects owing to their high mass-loss rates. Therefore, near-IR observations are the optimal wavelength to observe RSG stars at large distances.

Measurements of the temperatures of RSGs have also provided insight through using observations of extragalactic RSGs in the near-IR. The temperatures of RSG stars have been subject to debate for many years, which again is a product of their complex atmospheres and surface structures. There are many methods to estimate the effective temperature of a RSG star, the most popular of which is to fit the spectral energy distribution (SED) of the star with 1D model atmospheres (Levesque et al., 2005, 2006). However, Davies, B. et al. (2013) demonstrated that observations fitting models around the BVRI region, where molecular TiO bands dominate the absorption, result in a systematically lower temperature compared with fitting the line-free continuum regions of the SED. This is as a result of the TiO molecular line forming higher in the atmosphere of the star than the continuum. This means that fitting the TiO region and assuming that the best-fit effective temperature is representative of the entire SED is not a good assumption. Davies, B. et al. (2013) advocate using the entire SED *except* those regions dominated by the TiO absorption features. Estimating temperatures of extragalactic RSGs will be an important test for stellar evolution models and an excellent way in which to test models at different metallicities and in different environments. Patrick et al. (2015) highlighted the interesting result that the temperature of RSGs in different environments appears to be insensitive to the metallicity of the RSG. (This result is presented and commented upon in Chapter 5.)

In summary, I have highlighted some of the ways in which one can take measurements of RSGs both at home (in our own Galaxy) and abroad (in external galaxies). I have demonstrated that, owing to various factors, studies in the near-IR can have a significant impact on the understanding of RSGs and their environments. RSGs, and massive stars in general, play a key role in distributing

material throughout their host galaxies and our understanding of the physical processes that affect these environments is key to furthering studies of galactic chemical evolution.

1.4 Galaxy Chemical Evolution as Probed by RSGs

The evolution of galaxies is a vast area of study that can be broadly split up into three main fields: dynamical, thermal and chemical evolution. The chemical evolution of galaxies governs the origin and distribution of elements within the host galaxy. This evolution principally depends upon galaxy and star formation, where the initial distribution of the chemical elements is defined by how the galaxy is formed. Star formation acts to alter these quantities by creating, redistributing and removing chemical elements from the interstellar medium (ISM).

The lowest mass stars remove elements from the ISM by storing their gas and never evolving off the MS. Stars massive enough to evolve off the MS eject some mass during an AGB phase, but subsequently end their lives by removing elements from the ISM as passively cooling white dwarf stars. More massive stars undergo large amounts of mass loss during all phases of their evolution and end their lives by exploding as CCSN, both of which act to alter the chemical composition of their surrounding gas clouds.

It is important to take into account all three of these processes when studying how galaxies chemically evolve over time. However, quantifying contributions from these processes is complicated by a minefield of caveats and uncertainties.

Extragalactic observations of fundamental properties of galaxies play important roles in refining theories of galaxy formation and evolution. The mass–metallicity relationship (MZR; Lequeux et al., 1979) of galaxies links two fundamental parameters of galaxies. The stellar mass represents the amount of gas that star formation has removed from the ISM, whereas the present day galaxy metallicity represents how star formation has altered the initial ISM. Various authors have shown that galaxy mass is proportional to metallicity (Tremonti et al., 2004; Kewley & Ellison, 2008; Maiolino et al., 2008); Figure 1.6 shows such a result. This relationship can be interpreted by considering multiple factors. In low-mass galaxies, outflows and SNe have a greater effect on the amount of material ejected from the host galaxy into the intracluster medium, owing to their shallower

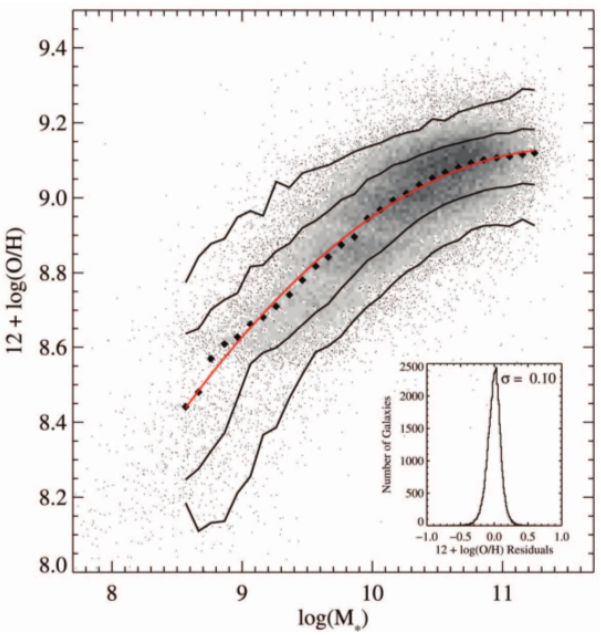

Figure 1.6 *The mass–metallicity relationship presented in Tremonti et al. (2004) where the gas metallicities of 53 000 galaxies from the Sloan Digital Sky Survey were measured using nebular emission lines and where the gas mass is measured using Hα luminosity. This figure shows that there exists a fundamental relationship between galaxy mass and metallicity.*

potential wells (e.g. Tremonti et al., 2004). Additionally, low-mass galaxies represent an early stage in Galactic evolution and, hence, these galaxies have not had time to process their gas into stars. As the host galaxy evolves, subsequent episodes of star formation increase the metal content of the galaxy (e.g. Maiolino et al., 2008, and references therein).

MZR observations have typically relied upon ratios of strong oxygen emission lines (usually [O II], [O III] relative to Hβ) from H II regions to estimate metallicities of individual galaxies. This technique is used owing to its applicability over a large distance range: Charlot & Longhetti (2001) use this technique in nearby galaxies, whereas Maiolino et al. (2008) estimate metallicity using this method in galaxies at $z > 3$. However, these measurements are known to be highly dependent upon the calibration method used (Kewley & Ellison, 2008; Kudritzki et al., 2008; Bresolin et al., 2009). In order to provide an independent calibration of this method, BSG stars have been used to determine metallicity and abundance gradients in external galaxies (Kudritzki et al., 2012). In addition to using BSGs, this thesis describes and builds on a method that uses RSGs as abundance probes of external galaxies, which can be used to calibrate the MZR by building up large

numbers of observations of RSGs in external galaxies.

Independent calibration of the MZR is essential to study how galaxies chemically evolve. The MZR has been shown to exist in the Local Universe as well as at earlier epochs within many different types of galaxies (e.g. Zahid, Kewley & Bresolin, 2011; Andrews & Martini, 2013; Cullen et al., 2014; Steidel et al., 2014; Yabe et al., 2014; Sanders et al., 2015) and is thought to be a ubiquitous property of galaxy formation.

1.5 Motivation and Outline

This thesis aims to develop and expand the use of RSGs as abundance probes in external galaxies with the eventual goal of independently calibrating the MZR of galaxy evolution. By using state-of-the-art model stellar atmospheres and high-quality spectroscopic observations of RSGs, in this thesis I will demonstrate the ability of this analysis method to study large populations of RSGs in external galaxies, not only measuring fundamental stellar parameters in a wide range of different environments, but also using RSGs as probes of how metals are distributed within external galaxies.

In addition, this thesis forms the basis on which all studies of RSGs with the K-band multi-object spectrograph (KMOS) will be founded upon. As I continue to learn about this instrument and make the most of the observations that have been obtained, I find that KMOS can be used not only for chemical studies of galaxies, but also to study the kinematics of populations within these galaxies.

RSGs have enormous potential to become important indicators of galaxy metallicity and this project has allowed me to become involved in the early phases of this project. In addition, with the coming generations of facilities and the realisation that near-IR studies have unique insights and qualities, near-IR spectroscopy (in general) will also become an increasingly prominent tool in the toolbox of the astronomer. Developing these analysis techniques and techniques of observation today is fundamental for making the best use of upcoming observatories. The aim of this thesis is to contribute significantly to this development.

This thesis is organised as follows. In Chapter 2, I describe the principles of spectroscopy and go on to describe KMOS, the instrument that is used for every

spectroscopic observation in this thesis, and detail the complex data products from this type of instrument.

Chapter 3 outlines the underlying physical principles that are used when constructing stellar model atmospheres and describes the state-of-the-art models that are used to analyse RSG spectra. This leads on to a description of the analysis technique that is used to measure stellar parameters of RSGs and tests this method on various different data-sets.

Chapter 4 describes observations of 14 RSGs within NGC 2100 (d $\sim$ 0.05 Mpc), a YMC in the Large Magellanic Cloud (LMC), where the chemistry and kinematics of the star cluster are assessed. Using the analysis routines described in Chapter 3, stellar parameters are estimated and compared to previous results. An upper limit to the line-of-sight velocity dispersion is measured for the cluster and the dynamical mass is estimated for the first time. By combining the individual RSG spectra, I demonstrate that this analysis technique can be used to estimate the integrated properties of unresolved clusters at larger distances at LMC-like metallicity.

Chapter 5 describes observations of 18 RSGs in NGC 6822 (d $\sim$ 0.5 Mpc), a dwarf irregular galaxy in the Local Group with a turbulent past. I test different strategies for reducing these data and quantify the spatial variations in metallicity within this galaxy, finding a suggestion of an abundance gradient. I demonstrate that using a simple, closed, chemical evolution model, the young and old populations of NGC 6822 are well explained: an important result, as NGC 6822 displays evidence for recent interactions. In this chapter, I also highlight the result that the temperature of RSGs does not appear to depend upon metallicity, something that is not predicted by evolutionary models.

Chapter 6 presents observations of 22 RSGs in NGC 55 (d $\sim$ 2 Mpc), a large spiral galaxy outside the Local Group of galaxies. Stellar parameters are estimated using the technique described in Chapter 3 and I discuss how to optimise the data reduction strategy to obtain results from a challenging data set. Using the multi-epoch properties of these observations I estimate the binary fraction of this sample and find it consistent with 0% binarity. Spatial variations in metallicity are examined and the evolution of NGC 55 is commented upon.

Finally, Chapter 7 presents concluding remarks and provides a first-look at the calibration to the MZR using RSGs in the Local Universe. I build upon this first look calibration by outlining the future work that I will take in this direction.

Chapter 2

Spectroscopy and the K-band Multi-Object Spectrograph

2.1 Opening Remarks

This chapter initially describes the basic design of a spectrograph and outlines some of the more commonly used spectroscopic techniques, in Section 2.2. I then describe integral field spectroscopy, a more complex spectroscopic technique, in Section 2.3, which leads to Section 2.4, where I describe KMOS. KMOS data and the data reduction process is detailed in Section 2.5. Finally, I conclude the chapter in Section 2.6.

KMOS warrants an individual chapter in this thesis as all of the spectroscopic observations presented in the proceeding chapters are observed with this instrument.

2.2 Introduction to Spectroscopic Techniques

Spectroscopy is the study of the dispersion of light into its constituents and has been at the forefront of astronomy for roughly the last 150 years. Sir Isaac Newton demonstrated the principles of spectroscopy (and coined the term "spectrum") using light from The Sun in his seminal "Opticks" work (Newton, 1704). By using the groove spacings on a diffraction grating, Thomas Young first quantified the

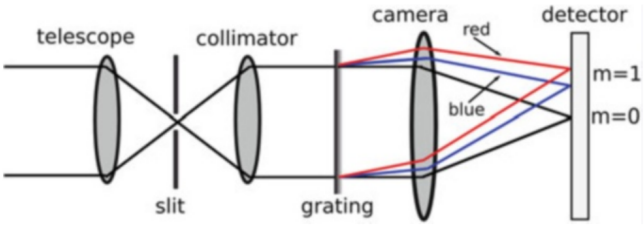

Figure 2.1 *A simple spectrograph detailing the five basic elements of a simple spectrograph: slit, collimator, dispersive element, camera and detector. Credit: Lawrence (2014).*

wavelengths of different colours of light (Young, 1802). The simple set-up of a spectrograph, which has – more or less – been used since the early spectroscopic experiments, consists of five basic elements:

i slit,

ii collimator,

iii dispersive element,

iv camera and

v detector.

A simple spectrograph is illustrated in Figure 2.1. In Newton's demonstration a small hole in the window blinds was used as a slit, and a screen as a detector. The slit in modern spectroscopic observations can take various forms. Today, the most widely used type of spectoscopic observation is long-slit spectroscopy. Using a long slit, a spectrum is taken for each spatial pixel, on the detector, along the length of the slit. This is demonstrated in Figure 2.2, where the final panel shows that each pixel illuminated within the slit produces a spectrum. This can be thought of a 2-dimensional spectroscopy, which is particularly useful when attempting to take a spectrum of an extended object (rather than a point source).

An alternative to using a long-slit to remove contamination from other sources is to use a small hole or fibre to select the target flux. By precisely drilling a hole in a metal plate, a slit is created that can be used to select the target flux. One of the advantages of using this method is that more than one object can be selected for a single exposure. By creating multiple slits within a single plate, spectroscopy of multiple objects can be obtained where contamination from other sources is

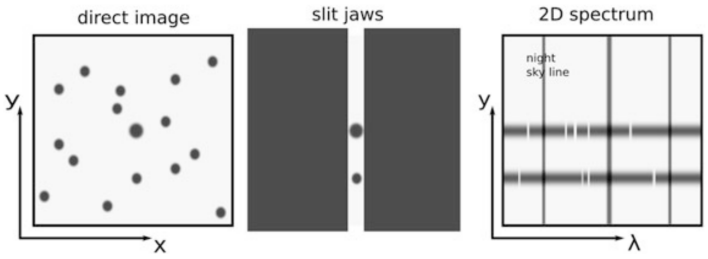

Figure 2.2 *Three panels demonstrating long-slit spectroscopy. The left panel shows an image of a field-of-view. The central panel illustrates that the long slit selects only the slit width in the x-axis and the full y-axis range. The right panel shows that for each pixel in the y direction, a spectrum is obtained. Credit: Lawrence (2014).*

minimised. The introduction of optical-fibres positioned within holes upon the plate provided a simple way in which to detach the heavy spectrograph from the telescope. Fibres can be led to an instrument housed within a separate platform (often a Naymsyth platform), which has the advantage that the instrument will not suffer from the changing gravitational force as the telescope moves. In addition, the conditions within the instrument room can be controlled. This is particularly important for near-IR spectrographs and detectors, where thermal radiation is important to minimise. Figure 2.3 details the principles of multi-object spectroscopy using optical-fibres.

However, using a plate with several holes has some drawbacks. These include, the time taken to create the slit mask, the lack of flexibility while observing and the operational costs of creating a new mask each time a different field is to be observed (Parry & Gray, 1986). These reasons, in addition to improved computing power, led to the development of instruments that were able to automatically position fibres (Tubbs, Goss & Cohen, 1982). Most modern fibre-fed spectrographs have automatic fibre-positioning technology which is broadly split up into two approaches:

i Each fibre has a magnetic button attached and a single robot is charged with moving each fibre sequentially. This is an effective method to place large numbers of fibres, but does however, take a significant length of time for each configuration.

ii Each fibre is mounted upon a computer-controlled arm. This method is generally less time consuming but increases the instrument build cost.

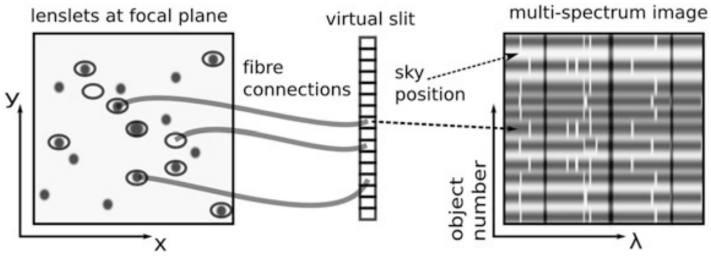

Figure 2.3 *Three panels demonstrating multi-object spectroscopy. The left panel shows an image of a field of view. The central panel illustrates that each fibre in this simple multi-object spectrograph can be positioned at any point throughout the field of view and is rearranged into a pseudoslit. The right panel shows that for each pixel in the y direction, a spectrum is obtained. Credit: Lawrence (2014).*

As a variant on the five basic elements of a spectrograph, slitless spectroscopy is also a feasible option, which is not discussed in detail here. For a thorough overview on slitless spectroscopy see Cullen (2014).

A key element to any spectrograph is the dispersive element. In Newton's original experiments this took the form of a glass triangular prism. A prism disperses light based on the wavelength dependence of the refractive index of glass: differential refraction. This produces a low-resolution spectrum spanning a large spectral range.

Typically in modern spectrographs the dispersive element is a diffraction grating. A diffraction grating disperses light owing to the principles of the interference of light when passed through multiple slits. The most simple example of this is a Young's double slit experiment where monochromatic light strikes two slits of width a, with separation d, at wavelength λ. The intensity pattern, along with Young's sketch of wave interference, for two narrow (where a $\rightarrow$ 0) is shown in Figure 2.4.

When one now considers that real diffraction gratings have slits of finite widths (rather than the a $\rightarrow$ 0 case considered above), the intensity pattern is modulated by the intensity pattern from a single slit (see bottom panel of Figure 2.4). However, the angular positions of the fringe maxima remain in the same fixed positions. As the number of slits is increased the maxima become narrower and more intense. The angular positions of the maxima are defined by,

$$sin\,\theta_{max} = \frac{m\lambda}{d}, \tag{2.1}$$

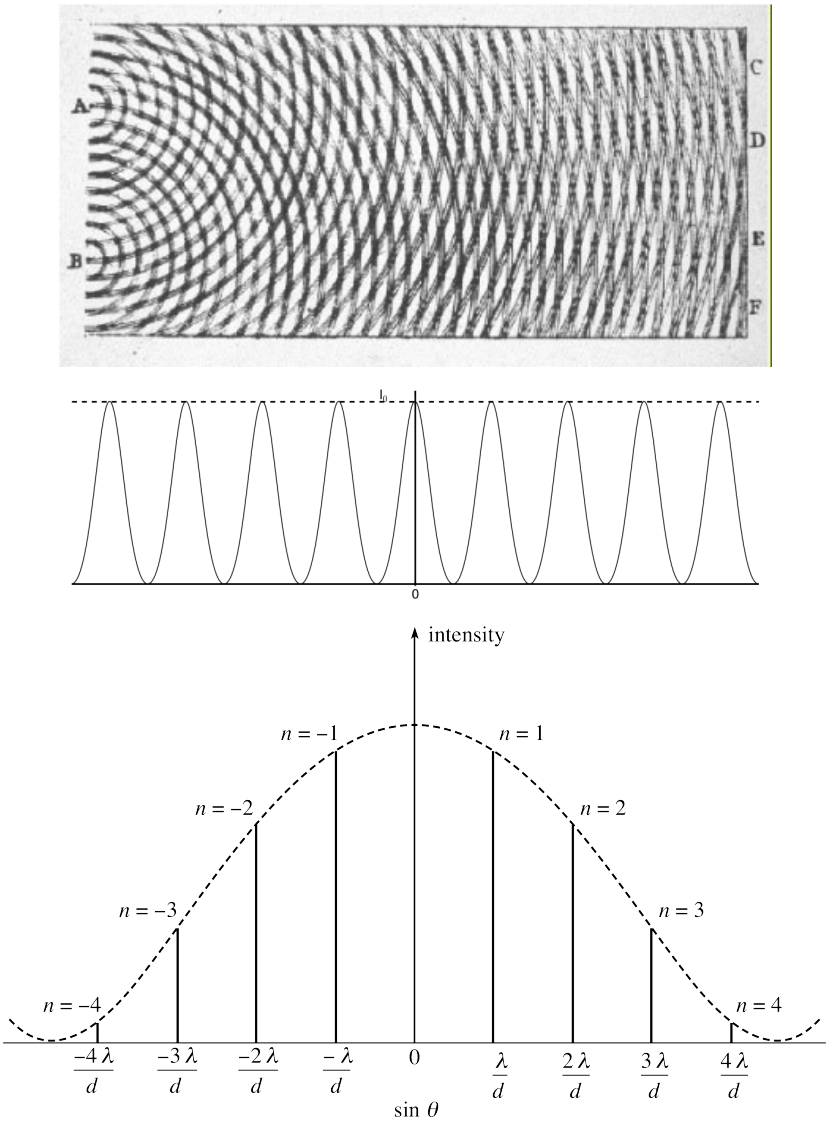

Figure 2.4 *Top: A double slit interference pattern from Thomas Young's original experiments. Middle: An intensity pattern for an idealised double slit experiment where the slit width (a) tends to zero. Each maxima represents a different spectral order (m). Bottom: An intensity pattern from a diffraction grating with more than 1000 slits where the slit separation is four times the slit width and the slits are of finite width. In this panel the single slit modulation is highlighted with the dashed line. Note that the intensity of the central maximum is proportional to the number of slits. Image credit (bottom panel): Open University.*

where m is an integer and refers to the fringe order ($m = 0$ for the central undispersed peak). Unlike the fringe maxima, the fringe minima between each maxima is proportional to N, their positions are given by,

$$sin\,\theta_{min} = \frac{m'\lambda}{Nd}. \tag{2.2}$$

Therefore, the angular width of the principle maximum between the first two zero positions ($\Delta\theta$ or W) is obtained by defining,

$$W = \Delta m' \frac{d\theta}{dm'}, \tag{2.3}$$

and by differentiating equation 2.2,

$$W = \frac{2\lambda}{Nd\,cos\,\theta}. \tag{2.4}$$

The Rayleigh Criterion states: "Two point sources are regarded as just resolved when the principal diffraction maximum of one image coincides with the first minimum of the other" (Rayleigh, 1880). By the application of this criterion one can define the spectral resolution in terms of the angular separation as,

$$W = \frac{\lambda}{Nd\,cos\,\theta}. \tag{2.5}$$

which does not depend upon the fringe order. Typically, the spectral resolution is quoted in terms of the smallest wavelength which can be separated in the spectrum. This is given by converting the angular width into the corresponding wavelength width using $\Delta\lambda = \Delta\theta\, d\lambda/d\theta$ which gives,

$$\Delta\lambda = \frac{\lambda}{Nm}, \tag{2.6}$$

more commonly quoted as the ratio of the operating wavelength to the spectral resolution,

$$R = \frac{\lambda}{\Delta\lambda} = Nm, \tag{2.7}$$

where R is the spectral resolving power (or often incorrectly, the resolution).

Separation of the spectral orders is an important consideration in diffraction grating spectroscopy, which can be taken into account by using a broadband blocking filter to limit the spectral range to a single order only. In principle, higher spectral resolving power can be obtained by viewing higher spectral orders, however, both the intensity of the spectra and spectral range are diminished. Typically low spectral orders are used in astrophysical observations.

Diffraction gratings have many intrinsic advantages over glass prisms, when used for quantitative spectroscopy, and are generally preferred. However, they are used in tandem for some applications. For example, Echelle spectrographs, working in higher orders to achieve higher resolving power, make use of an additional dispersive element, which is often a prism, to spatially separate different orders so that they can be simultaneously recorded on the detector.

Even though prisms are used less regularly than diffraction gratings in modern astronomical spectroscopy they still have important applications. A prim can be combined with a diffraction grating attached to the face of a prism (i.e a grism) to obtain spatially extended spectroscopy over a large spectral range. The upcoming near infrared spectrograph (NIRSpec) instrument, on the James Webb Space Telescope (JWST), will contain a prism (in addition to several diffraction gratings) to obtain low-resolution spectroscopy of a very large spectral range (0.6–5.3 μm).

2.3 Integral Field Spectroscopy

The overall goal of integral field spectroscopy (IFS) is to obtain a spectrum of everything (targets and their surroundings) within a given field-of-view (FoV). This concept builds on the idea that a long-slit spectrograph obtains spectra for targets within the extent of the slit. A natural extension of this technique would be to use a long-slit spectrograph to obtain a spectrum for each pixel within a 2-D FoV on the sky.

There are many intrinsic advantages to having a specifically designed instrument to perform this task rather than simply repeating observations with a long-slit spectrograph. These advantages include,

i eliminating slit-losses,

ii accurate target acquisition is not required,

iii the target position can be recovered from data,

iv reduced radial velocity errors from positional issues in the slit when comparing target and reference object,

v the velocity field is recovered without biases.

In addition, potentially the most compelling argument is that to perform IFS with a long-slit spectrograph one is required to take N exposures all of length t_{exp}, however, using IFS, a spectrum for each spaxel is obtained with a single exposure. Therefore efficiency on-sky is increased.

2.3.1 Techniques of integral field spectroscopy

IFS may be achieved using a variety of different and novel methods. Potentially, the simplest of these is (and most cost effective in the short term) to take multiple exposures using an existing spectrograph over a small FoV. Another, conceptually simple, approach is to take photometric data of the same field using multiple narrow-band filters which can be stitched together to create effectively low-resolution spectra of a FoV (e.g. GTC-OSIRIS; Méndez-Abreu et al., 2011).

There are three main techniques which are more commonly used to generate spectra over a 2-dimensional FoV. The difference between the techniques is in the way in which they split up the image. A spectrograph specialised for IFS adds an additional element to the five basic elements of a spectrograph outlined previously: an integral field unit (IFU). An IFU splits up the image obtained by the telescope into elements, or slices, that are constructed into a slit and dispersed by the dispersive element. In this section I will detail each of these techniques in turn and conclude by providing a comparison between them.

A lenslet array splits the input image using a tight array of small lenses (Bacon et al., 1995). The lenses then focus the light of each sub-field separately that are then dispersed. This technique limits the length of the spectrum measured on the detector. To improve this, the spectra are tilted about the optical axis to minimise overlapping of spectra, which leads to inefficient packing of the resulting

spectra on the detector. The top row of Figure 2.5 illustrates IFS using a lenslet array to split the image.

Fibre arrays use a tightly packed bundle of fibre-optic cables to split the telescope image. The fibres then reposition the image onto a linear slit. The middle row of Figure 2.5 illustrates this process. As the fibre cables are intrinsically cylindrical objects, light is lost between fibres in the focal plane. To minimise the light lost, this technique can be improved upon by using an array of lenses, to focus the light from each element into the fibre, effectively combining this technique with the previous method.

The final technique is to use an image slicer to split the image from the telescope (Content, 1997). Figure 2.6 shows an image slicer used in the KMOS instrument. An image slicer is a type of segmented mirror where each linear segment reflects light in a slightly different direction. A second segmented mirror then arranges the images into a pseudoslit where it is then dispersed. As Allington-Smith (2006) demonstrated, this method is intrinsically efficient as complete slices of the field are imaged by the detector. In addition, this method is also particularly applicable for IR studies as the optical system consists mainly of mirrors which are easily cooled to low temperatures. Drawbacks with this technique include that a large and complex optical system is required with a surface roughness (σ) of $\sigma \leq 10\,\mathrm{nm}$ in the IR.

Allington-Smith (2006) performed a detailed theoretical comparison between these three techniques and concluded that, using an image slicer to split up the telescope image is the most efficient, by a considerable margin. In addition, fibres and lenslet arrays give similar performances, although lenslet arrays are easier to construct. Image slicer instruments are the most complicated to construct as a result of their complex optical systems, however, these instruments are also the most applicable for IR studies.

2.4 The K-band Multi Object Spectrograph

KMOS is a second generation instrument on the Very Large Telescope (VLT), Chile, which completed its design review in 2008 and completed commissioning in April 2013. As its name suggests, KMOS is a multi-object spectrograph operating at near-IR wavelengths (providing coverage from 0.8–2.5 μm), which hosts 24

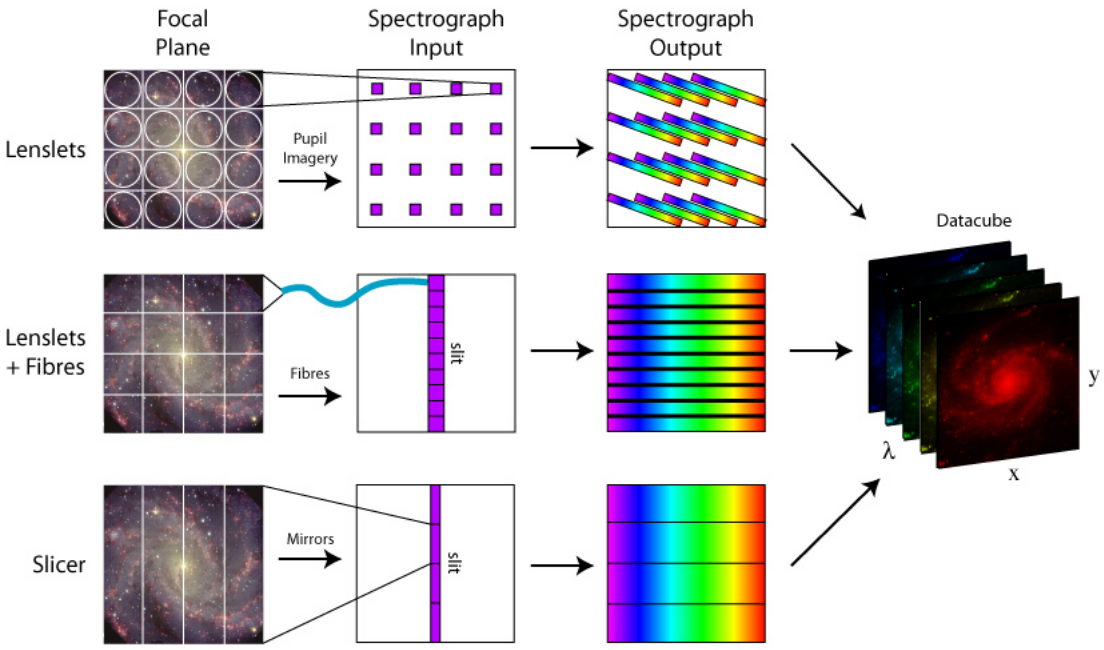

Figure 2.5 *Three diagrams demonstrating the techniques of integral field spectroscopy. The top row shows how an array of lenslets can be used to focus the light for the spectrograph. The right-hand panel of this row demonstrates that this leads to inefficient packing of the spectra on the detector. The middle row shows how a combination of fibres and lenslets can be used to reconstruct a slit and make more efficient use of the detector. The bottom panel shows that an image slicer efficiently splits up the field-of-view and reconstructs the slit using mirrors. Each technique results in a three-dimensional data cube consisting of x, y and λ information for each pixel on the detector. Credit: M. Westmoquette, adapted from Allington-Smith (2006).*

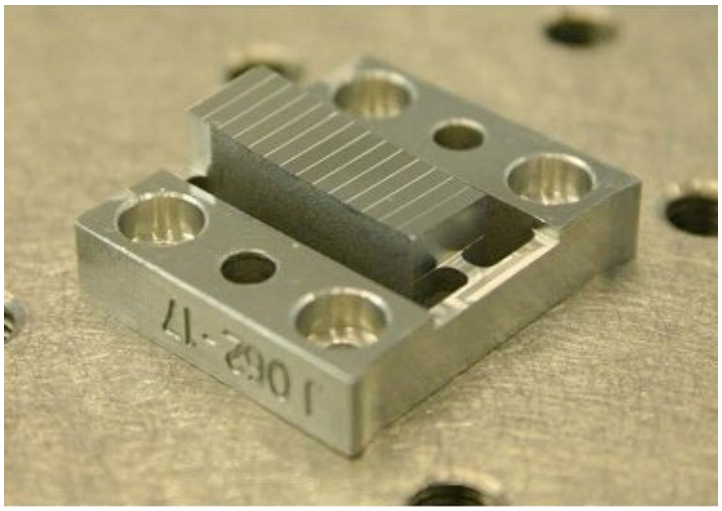

Figure 2.6 *An image slicer from one of the arms used in the KMOS instrument. An image slicer is a type of segmented mirror that slices the image into different segments (14 in this case), where each segment focuses the light in a slightly different direction. KMOS has 24 image slicers. Note: Image retrieved from the European Southern Observatory website: https://www.eso.org/sci/facilities/develop/instruments/kmos.html.*

configurable IFUs. Therefore, KMOS can be described as a multi-object integral field spectrograph.

KMOS was designed specifically to provide spatially-resolved spectroscopy, while allowing multiple spectroscopic observations at near-IR wavelengths and was constructed by a consortium of UK and German institutes in collaboration with the European Southern Observatory (ESO). The final design of KMOS boasts 24 configurable arms, each hosting an IFU with a $2\farcs8 \times 2\farcs8$ FoV that can be placed at user-specified positions within a $7\farcm2$ FoV. These IFUs anamorphically magnify their individual sub-field onto one of the 24 advanced image slicers that partition each sub-field into 14 slices each with 14 spatial pixels. Therefore one KMOS IFU obtains 14×14 contiguous spectra in a single exposure.

The optical design of KMOS includes a three-fold symmetry about the Nasmyth optical-axis. Figure 2.7 illustrates the KMOS light path for one of the three segments. Each segment is designed to receive the light from 8/24 IFUs that is then passed to a cryogenic spectrograph containing five diffraction gratings (IZ, YJ, H, K and HK). Therefore, KMOS has three quasi-identical spectrographs which can be independently configured and set up.

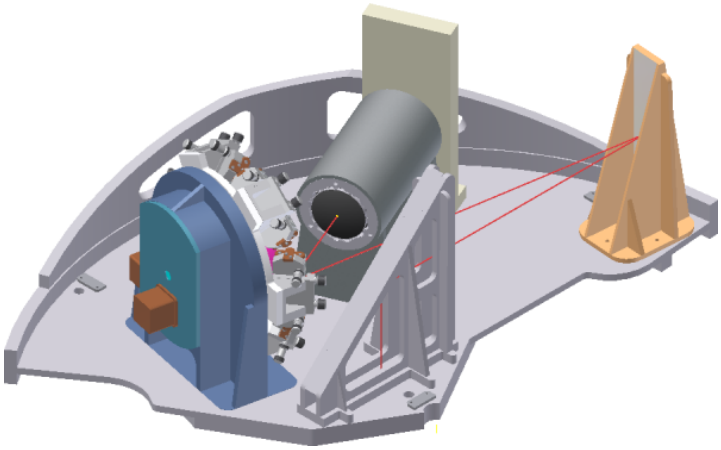

Figure 2.7 *The light path for one of the three KMOS spectrograph demonstrated by the solid red line. The integral field unit entrance slit is located underneath the baseplate. The light path comes from the slit entrance and is redirected by the fold mirror toward the collimator (right, highlighted in yellow), where the light then is directed to the grating (left, housed in the blue filter wheel containing all 5 gratings) which disperses the light in camera barrel which finally focuses the light onto the detector (where the detector mount is in beige).*

KMOS was designed with specific science goals that focused on the case for spatially resolving the structure in galaxies across a large range of redshifts and environments (Sharples et al., 2006) and, as the most-efficient near-IR multi-object spectrograph in the southern hemisphere (and the only one – at the time of writing – on an 8-m class telescope), KMOS has gained significant attention from the scientific community. Following successful commissioning runs KMOS underwent two science verification (SV) runs before being made available to the community for general observing in October 2013 (Sharples, 2015). To date, KMOS has had an impact in the fields of some of its key science drivers (e.g. Harrison et al., 2016; Magdis et al., 2016), as well as some intriguing results in other areas (e.g. Feldmeier-Krause et al., 2015; Parviainen et al., 2015).

In addition, KMOS has been exploited as a multi-object spectrograph to study the metallicities of star-forming galaxies using RSGs as cosmic abundance probes (Gazak et al., 2015; Lardo et al., 2015; Patrick et al., 2015). This thesis makes extensive use of KMOS and would not be possible without this state-of-the-art instrument.

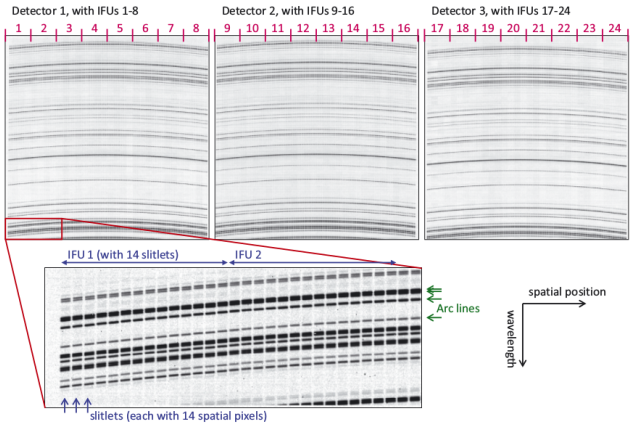

Figure 2.8 *An example of a KMOS raw data product, illustrating how the data is arranged on each detector, taken from Davies, R. I. et al. (2013). Each KMOS raw data product contains information from three detectors. Each detector records light from eight IFUs, each of which contains 14 slitlets. Each slitlet contains 14 spatial pixels and therefore for each IFU, 196 spectra are produced. On the detector, the spectra from each of the slitlets is separated by 3 pixels. The 14 spectra from one slitlet have a width of one pixel and are aligned side-by-side on the detector. The spectra are dispersed roughly in alignment with the y-axis on the detector and the x-axis roughly corresponds to the spatial axis.*

2.5 Production of Three-dimensional Data Cubes

The nature of IFS is to obtain spatial and spectral information for each pixel on a detector. The final data product is, therefore, a three dimensional data cube, which consists of two spatial and one spectral dimensions. The aim of the data reduction and calibration process is to create a regularly-sampled data cube from several raw detector images.

As mentioned, KMOS is arranged into three identical segments. Each segment contains eight IFUs, which are arranged to project data onto a single detector. Each IFU contains an advanced image slicer, which slices the field into 14 slices (see Figure 2.6), each of which contains 14 spatial pixels. Therefore, each IFU produces 196 individual spectra and a single detector contains over 1500 spectra. A visualisation of a KMOS raw data product is illustrated in Figure 2.8 and highlights that each IFU contains 14 spectra each of width 14 pixels on the detector. This figure demonstrates how the dispersed spectra are arranged on the detector.

KMOS is designed so that, on the detector, the x- and y-axes roughly correspond

to the spatial and spectral axes respectively. However, on the detector there is no concept of spatial and spectral axes, only information that can be calibrated and reconstructed into regularly sampled cubes containing spatial and spectral information.

2.5.1 Calibration

To calibrate KMOS data each value recorded by the detector must be assigned spatial and spectral information. To do this one can use the projection of the light onto the detector, and the reliability of this projection, as a detailed diagnostic. Slitlets are projected on the detector to $\pm 1\,\mu$m (roughly $1/18^{\text{th}}$ of a pixel; Davies, R. I. et al., 2013) and the mean slit-width across the detector is 13.6 ± 0.1 pixels, where the error quoted here is the standard deviation of the mean from all slitlets. This pattern is so stable that subtle imprints of the opto-mechanical design of the instrument can be seen in the patterns (see Fig. 2 of Davies, R. I. et al., 2013).

The main factor that affects this pattern is the temperature of the spectrograph. As with any IR instrument, the detector must be cryogenically cooled to minimise the effects of photons from the thermal background promoting electrons into the conduction band of the semi-conducting diode of the detector, which are then confused with signal from the target. For KMOS the detectors are cooled to $\leq$80 K. In addition to the cooling of the detector, the optical bench – which houses the spectrographs – is also cooled to $\leq$140 K. However, the temperature of the optical bench is not controlled and can therefore vary with the ambient temperature of the surroundings by several Kelvin. This variation in temperature has a small, but significant, effect on the positions of the slitlet edges when compared in the calibration- and science-frames (described below). The implications of this potential temperature variation of the optical bench is that during calibration frames, the temperature must be within ± 1 K of the science frames.

To make use of the pattern of the slitlets on the detector, to calibrate the raw data, two types of calibration frames are obtained:

i Flat lamp calibrations: use a halogen lamp with a white-light spectral appearance to fully illuminate each slitlet. These frames are used to calibrate the spatial positions of each detector pixel.

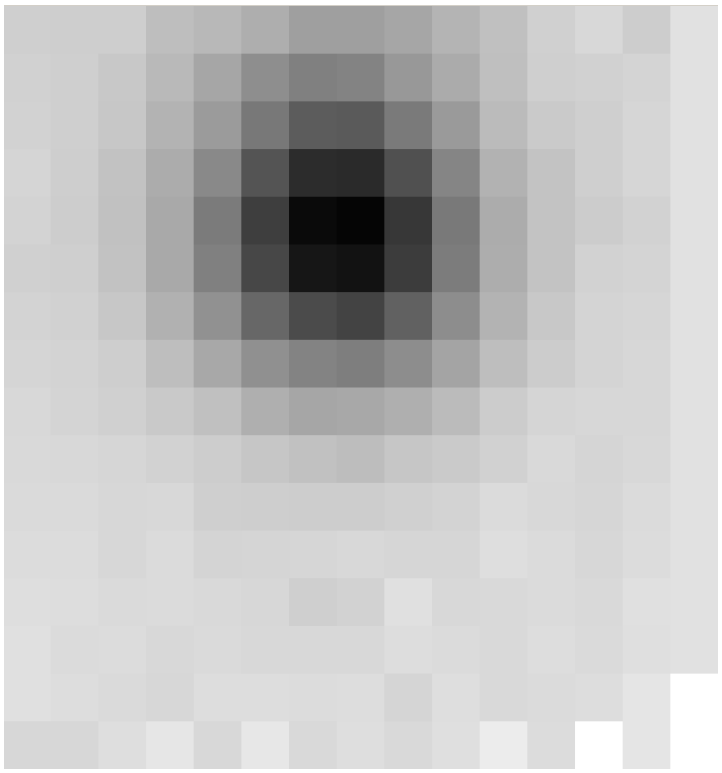

Figure 2.9 *An image of reconstructed KMOS integral field unit, demonstrating that each of the 14 slices of the field contains 14 pixels. This image is at a wavelength of 1.100 μm. A spectrum is produced for each pixel and the current image is a snapshot at one particular spectral pixel.*

ii Arc lamp calibrations: use halogen lamps to create a spectrum containing many diagnostic spectral features, which are used to calibrate the wavelength of each detector pixel.

These calibration frames are then compared with the science frames to construct a three dimensional data cube for each IFU. An example of a reconstructed IFU is given in Figure 2.9. This figure is a snapshot of the reconstructed IFU at a particular wavelength.

Calibration of the KMOS data can be split into three distinct processes:

i flatfielding,

ii mapping data onto a regularly-sampled cube,

iii correcting for atmospheric emission/absorption and instrument transmission.

All of these processes are required to calibrate spectroscopic data in general, however, mapping the distortions of an instrument and transforming the data into a regularly sampled cube are instrument-dependent, and, because of the complexity involved in arranging eight IFUs onto a detector, are the most important aspects in calibrating KMOS data.

Flatfielding is the process that corrects for the difference in response from detector pixels and is performed in a standard fashion using halogen lamps. Flatfielding is also used to correct for variations in the illumination of the KMOS IFUs. This is done directly using exposures from halogen lamps (lamp flats) and can be improved upon by using twilight sky to illuminate the detector (sky flats). Using the twilight sky is, in general, preferred as the light path is identical to that of the science exposures. However, observing in twilight conditions is extremely time dependent and in practice is difficult to undertake for an instrument as complex as KMOS.

To create a three dimensional data cube from KMOS raw data, a look-up table is created containing information relating each detector value with spatial and spectral locations. This look-up table is implemented by creating three calibration files containing x, y and λ information for each pixel. These calibration frames are created by making use of the repeatability of the pattern of the slitlets on the detector. By fully illuminating the slitlets using the lamp-flat exposures the edge positions can be mapped from the calibration frames onto the science frames. This provides the two spatial coordinates for each detector value.

To calibrate the wavelength of the each detector pixel one must illuminate the detector with a spectrum where the wavelength of each spectral feature is precisely known (i.e. arc lamp calibrations). This is achieved with KMOS using a halogen lamp containing Neon and Argon where strong spectral features of known wavelengths cover the full detector range. By identifying a few isolated spectral lines within these exposures, which are then traced across the length of the detector, a polynomial function is used to assign a wavelength solution to the detector.

At this stage, all the information needed to create the three dimensional data cube is available in three calibration frames. This information is now used to transform the detector values onto a regularly sampled three dimensional data cube for each IFU. It is necessary to perform multiple interpolations to the detector values, rather than simply rearranging these values, as – in the frame

of reference of the regularly sampled three dimensional data cube – the detector values are irregularly sampled. This is obvious from Figure 2.8 which illustrates that the spatial and spectral axes are *roughly* aligned with the x and y axes of the detector respectively.

As KMOS is a roughly three tonne instrument, the effects of flexure can be significant and are mainly caused by rotation of the instrument on the Nasmyth platform. To account for this, calibration frames are taken at various rotator angles that are chosen to match the rotator angle of the science observations. Using calibration frames at a more appropriate rotator angle can make a reasonable correction to the most serious sources of flexure.

There are, in principle, many different methods to create the data cube that affect the spectral and spatial resolution of the final data product. The method that typically produces the highest quality data uses two (or three) one dimensional interpolations: the so-called "cubic spline interpolation" routine in the pipeline. This method makes use of two properties of the IFUs:

i each slitlet is a straight line when projected onto the sky,

ii the spacing across each slitlet is fixed and uniform (as a result of the properties of the image slicers).

By exploiting these properties, this method is able to assign each detector pixel an x, y and λ value. This is achieved by rearranging the detector values across each slitlet where no interpolation is necessary, using (ii).[1] Subsequently, a one dimensional cubic spline interpolation is performed along each slitlet, using i. A final one dimensional cubic spline interpolation is performed in the spectral direction. This method produces the best spectral resolution as well as giving highly consistent spatial resolution within each IFU.

The final step in calibrating KMOS data is to take into account the effects of the Earth's atmosphere. Observing from within the Earth's atmosphere affects the quality of the data in two different ways. Intrinsically, when observing an astrophysical source through the Earth's atmosphere, each illuminated detector pixel contains a combination of source- and sky-photons. Molecules and dust within the atmosphere scatter, absorb and emit light from the Earth and Moon,

[1] This is the case when the default sampling is used, when any other sampling is requested this step requires an additional interpolation performed using the cubic spline method.

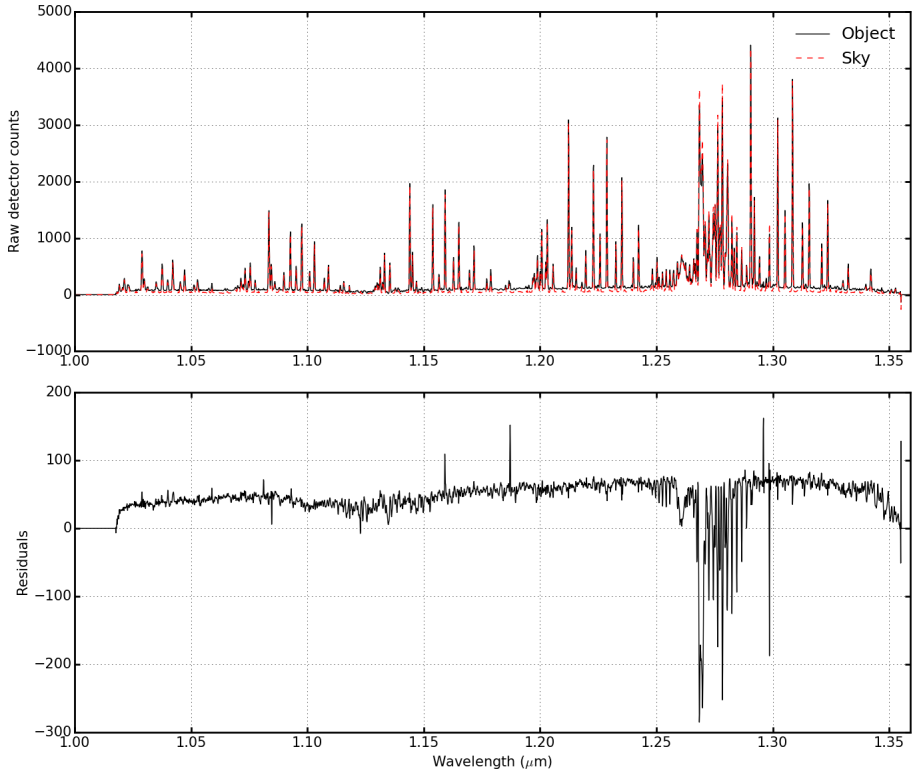

Figure 2.10 *An example of the sky subtraction procedure. The top panel shows an object spectrum, in black, and an associated sky spectrum, in red. The bottom panel shows the sky subtracted spectrum by simply subtracting the two spectra in the top panel. Note the difference in scale between the two panels, illustrating that the signal from the sky is typically significantly larger than that from the object.*

which contaminates spectroscopic and photometric observations. To account for this one typically attempts to observe a sky spectrum without any signal from the astrophysical source. This usually takes the form of observing offset sky positions, where, between each target exposure, sky exposures are observed that are chosen to minimise contamination. This results in an additional set of sky frames that are then used to calibrate the science frames using the same IFU in both science and sky exposures. A simple example of the sky subtraction procedure is illustrated in Figure 2.10. This figure shows that the signal from the sky is significantly larger than the signal from the object. These sky frames are dealt with in the same manner as science frames in terms of calibration. Typically, before the reconstruction of the three-dimensional data cubes however, the sky frame which is nearest in time to the science frame in question is subtracted.

The second correction accounts for the absorption and re-emission of light from the science target by molecules within the Earth's atmosphere. As the

sophistication of this step is highly dependent upon the science case of the observations, for the general user this is implemented in a simplistic manner. Typically, to perform this correction one observes an additional target of known spectral appearance: a telluric standard star. This star is observed in each of the 24 KMOS IFUs in turn (or three IFUs depending upon the quality of the correction required) and the frames are calibrated using the same process as the science observations.

A spectrum is extracted from each IFU that is then divided by a model of the transmission of the atmosphere, the stellar features are then modelled with a simple Lorentzian function and removed. This leaves a continuum spectrum of the star where the main features have been removed. At this point the transmission model is then multiplied back into the spectrum and the shape of the spectrum is corrected with a blackbody spectrum, where the temperature is defined by the spectral type of the observed standard star. Theoretically, these steps create a spectrum that contains only the light from the absorption of the Earth's atmosphere: the telluric spectrum. The final target spectrum from an individual IFU is then divided by the telluric spectrum.

This is a simple overview of how one corrects for the effects of the Earth's atmosphere is KMOS observations. For a more detailed discussion of how this can be improved see Chapter 4 Section 4.3 and Chapter 5 Section 5.3.

2.6 Conclusions

In this chapter, I have detailed the principles of spectroscopy and have outlined some of the key spectroscopic tools used to take astrophysical measurements, focusing on the diffraction grating and its uses in astronomy. I have described IFS in detail and outlined some of the innovations that make this novel method possible. I focused on using an advanced image slicer to perform IFS and outlined why this method is superior to other approaches. This led onto a description of KMOS: the instrument used to obtain the spectroscopic data used in the subsequent chapters of this thesis. In this section I detailed some of the key features that make this instrument unique and highlighted that KMOS has been applied to a range of science cases. Finally, I described the data products from KMOS and detailed the process of calibration of the raw data.

Chapter 3

J-band Spectral Analysis

3.1 Opening Remarks

In this chapter, I describe in detail the process I use to implement an analysis routine to fit synthetic spectra to observed data with the aim of estimating stellar parameters. This analysis builds on existing methods while providing a fresh approach to various aspects of the routine. I have developed this implementation in the public domain and the source code for this project is made publicly available via an online repository.[1]

I begin this chapter by providing an outline to the principles of model stellar atmospheres (Section 3.2), discussing the physics included in these models, as well as some of their strengths and limitations. I then focus the discussion on the grid of synthetic stellar spectra, which forms the base of this analysis routine, in Section 3.3. In Section 3.4, I detail the procedure of matching the continuum level of the observations with that of the models, which leads on to Section 3.5, where the method by which the best-fit parameters are selected is described.

Having described the analysis routine thoroughly, I then test it and compare the results of this method with different implementations in the literature in Section 3.6. Finally, I conclude the chapter in Section 3.7.

[1]Source code available from: https://github.com/lrpatrick/rsg-janal, although the interested reader should be aware that these routines are, at the time of writing, in development mode in the sense that they are highly specialised to one machine and (particularly) one set of model grids.

3.2 Introduction to Stellar Model Atmospheres

A stellar atmosphere is defined as the outer layers within a star that emit radiation. Therefore, by definition, the photons that are observed from a star have originated in the atmosphere. Photons that have originated from deeper layers within the star have been absorbed and re-emitted by particles within the stellar atmosphere. Stellar atmospheres are therefore vitally important in observational studies of stars, even though the fraction of the total mass of the star contained within the atmosphere is tiny ($\sim 10^{-10}$). A nice analogy for visualising this layer and its thickness comes from the preface of Böhm-Vitense (1989), who compared the skin of an apple with a star hypothetically shrunk to the same scale and noted that the skin of an apple is far thicker than the stellar atmosphere.

Even though stellar atmospheres contain a tiny fraction of the total stellar mass, these layers can have an enormous impact on the evolution of a star via stellar winds. For example, in evolved massive stars, winds arising from the atmosphere can strip off the outer layers of the star to leave an exposed hydrogen and helium dominated core or push the star in a different evolutionary direction (see Chapter 1). In addition to having an impact on the evolution of the star, winds also help distribute material throughout their host galaxy and feed subsequent generations of star formation (e.g. Hopkins, Quataert & Murray, 2011, 2012), thereby not only affecting the evolution of the star in which the wind is produced, but also, by acting as part of a larger stellar population, affecting the evolution of their host galaxy.

By modelling stellar atmospheres, one can estimate fundamental stellar parameters through a comparison with observations. The background theory and underlying physical assumptions of these models are the subject of the current section. These are important to detail, as without this background it is impossible to assess the effectiveness of the models and their limitations.

Two of the most fundamental equations that govern the properties of stellar atmospheres are,

$$g = \frac{GM}{R^2}, \tag{3.1}$$

and,

$$T_{\rm eff} = \left(\frac{F}{\sigma_{SB}}\right)^{\frac{1}{4}} = \left(\frac{L}{4\pi\sigma_{SB}R^2}\right)^{\frac{1}{4}}, \tag{3.2}$$

where g is the acceleration due to gravity, M is the total mass of the star of radius R, $T_{\rm eff}$ is the effective temperature of the star, F is the total flux per unit area, L is the total luminosity of the star, σ_{SB} is the Stefan–Boltzmann constant and G is Newton's gravitational constant.

These equations define two fundamental observational properties of model stellar atmospheres. Equation 3.1 is defined by the density stratification of the model and equation 3.2 is defined through the total flux emitted from the model.

In the following sections, I detail the three principal assumptions that are used to create a "classical" one dimensional stellar model atmosphere. These assumptions underpin some of the most widely used model atmospheres.

3.2.1 Hydrostatic Equilibrium

Any model of a star consists of a balance between gravity and pressure in a gaseous material (or plasma considering the typical temperatures and densities within a star). If a model is assumed to be static (i.e. not varying with time) the equation of hydrostatic equilibrium can be derived by considering the balance between forces acting upon a small element of stellar material,

$$\frac{dP(r)}{dr} = -\frac{\rho G M(r)}{r^2}, \tag{3.3}$$

where P is the pressure exerted within radius r, M is the mass within radius r and ρ is the matter density (see Chapter 9 of Böhm-Vitense, 1989, for a simple derivation of this equation). As stated above, the mass contained within the atmosphere of a star is a negligible fraction of the total mass; therefore, $M(r) = M_{tot}$ when considering this equation in the outer layers of the star.

The force exerted by pressure acting on an element of stellar material (dP/dr) can be considered as the sum of the forces acting upon it from gas pressure (P_g),

radiation pressure (P_{rad}) and turbulent pressure (P_{turb}),

$$\frac{dP_{tot}}{dr} = \frac{dP_g}{dr} + \frac{dP_{rad}}{dr} + \frac{dP_{turb}}{dr}. \tag{3.4}$$

Equation 3.4 illustrates that, even though we have assumed the model is static, small scale turbulent motions must still be taken into account to accurately model stellar atmospheres.

3.2.2 Mixing-length Convection

Mixing-length theory describes how convection is treated within a stellar atmosphere. Generally, radiation is the main source of energy transport within stellar atmospheres, as the coefficient of diffusion is far smaller for particles (conduction) than for photons (radiation). Only in degenerate cores does energy transport via conduction become important. Convection also plays an important role in the transport of energy at different evolutionary points in a star.

Convection, in stellar interiors, is a very efficient form of energy transport, where a macroscopic element of higher temperature rises an average distance into a region of lower temperature where it dissipates the excess energy being carried and mixes. However, for convection to be effective, a driving mechanism must be established. The atmosphere is unstable to convection if the Schwarzschild criterion is met,

$$\nabla_{rad} > \nabla_{ad}, \tag{3.5}$$

where $\nabla_{rad} = (d \ln T / d \ln P)_{rad}$ is the radiative temperature gradient and ∇_{ad} is the adiabatic temperature gradient. The driving mechanism for convection is usually a large temperature gradient within a particular layer of the star. This can occur at various stages within the lifetime of a star; for example, most MS stars have a convective core that is a result of the temperature sensitivity of the CNO cycle, which establishes a steep temperature profile.

The theory of convection is very difficult to treat thoroughly. The "simple" theory of mixing-length convection, (Böhm-Vitense, 1958; Henyey, Vardya & Bodenheimer, 1965) is widely used to implement convection within stellar

atmospheres. This theory assumes that the shapes and sizes of the elements that transport energy are fixed and that, on average, an element rises a characteristic length (l_m) before it dissipates energy.

If the Schwarzschild criterion is satisfied, the total flux (F) for a star is given by,

$$F(r) = F_{conv} + F_{rad} = \sigma T_{eff}^4, \tag{3.6}$$

where F_{conv} and F_{rad} are the convective and radiative flux respectively. An expression for the convective flux can be obtained by considering the excess energy dissipated by a rising element moving a distance ($\Delta r = l_m/2$) with an average velocity (v_{conv}). The convective flux can therefore be expressed as,

$$F_{conv} = \rho C_p v_{conv} \Delta T, \tag{3.7}$$

where C_p is the specific heat at constant pressure and ΔT is the temperature difference between the element and its surroundings, which can be expressed in terms of the difference in temperature gradients. Here, the pressure scale height can be introduced using the assumption of hydrostatic equilibrium ($H_p = dr/d\ln P = p/\rho g$) and an expression for the convective velocity can be estimated by assuming that half the work done by buoyancy is converted into kinetic energy,

$$\frac{1}{2}\langle w \rangle \approx \frac{1}{2}\rho v_{conv}^2. \tag{3.8}$$

The parameter $\alpha = l_m/H_p$ is introduced, which typically takes the value $\alpha = 1.5$–2.0. As a side note, in stellar evolutionary models, the value of α used can have a significant effect on the temperature of the models at the end of the RSG phase of evolution.

3.2.3 Local Thermodynamic Equilibrium

The assumption of thermodynamic equilibrium is where the temperature and density of a material can be considered constant (i.e. there are no net flows of energy). This is equivalent to assuming that the emitting source is a perfect black body. Local thermodynamic equilibrium (LTE) is an approximation whereby the

local properties of a material are assumed to be in thermodynamic equilibrium. Stellar atmospheres can be approximated to be in LTE, as their densities are sufficiently high and their density gradients are sufficiently low that their local properties tend towards thermal equilibrium.

The three fundamental equations that can be defined assuming LTE are:

i the Boltzmann equation,

$$\frac{n_i}{N_I} = \frac{g_i}{U_I} e^{-E_i/kT}, \tag{3.9}$$

ii the Saha equation,

$$\frac{N_I}{N_{I+1}} = n_e \frac{U_I}{U_{I+1}} \left(\frac{h^2}{2\pi m_e kT} \right)^{\frac{3}{2}} e^{\chi/kT}, \tag{3.10}$$

iii the Maxwellian distribution of particles,

$$f(v)dv = \left(\frac{m}{2\pi kT} \right)^{\frac{3}{2}} \exp\left(\frac{-mv^2}{2kT} \right) 4\pi v^2 dv, \tag{3.11}$$

where n_i, g_i and E_i are the population, statistical weight and energy of level i respectively; N_I, U_I and χ_I are the total number density, partition function and ionisation potential of ionisation state I (to which i belongs); m is the mass of the particle; v is the velocity of the particle; T is the temperature of the particle; k is the Boltzmann constant; h is the Plank constant; and m_e is the mass of an electron. Equation 3.9 determines the level population of a particular ionisation state for a given atom and in combination with the Saha ionisation equation (equation 3.10), is used to determine the total level population for a given atom.

3.2.4 Analysis of Assumptions and Summary

The assumptions listed above allow one to create a "classical" stellar model atmosphere. These assumptions are known to be simplifications of the true picture within a stellar atmosphere. For example, the assumption of LTE does not hold true in the atmospheres of stars, as they are observed and, by definition, emit radiation. However, using the above assumptions, one can build a consistent model that, in general, agrees reasonably well with observations.

The treatment of convection is an over-simplification where one of the most basic limitation is that the assumed shape and size of the convective elements are constant, whereas numerical simulations and helioseismology show that this is not the case (Kippenhahn, Weigert & Weiss, 2012). Full two- and three-dimensional hydrodynamical simulations are required to assess the assumption of mixing-length convection, which generally show that convective fluxes are smaller than those in more sophisticated prescriptions (Kippenhahn, Weigert & Weiss, 2012). For evolved massive stars in particular, the assumption of mixing length theory may break down where the timescales for convective overturn becomes comparable to the stellar evolution timescale (Weiss et al., 2004)

The assumption of LTE typically holds in dense, deep layers of a star; however, in the atmosphere (where radiation is emitted), this is known to be a poor approximation. This is particularly true in evolved stars where departures from LTE are expected owing to the low densities and surface gravities of their atmospheres.

Full non-LTE stellar model atmospheres are expensive to produce and are only available for particular sets of stellar parameters (e.g. TLUSTY for stars with $T_{\rm eff} > 27\,500$; Lanz & Hubeny, 2003), as of yet, there exists no homogeneous grid of model atmospheres that includes these effects for cool stars. As a first step, one can use a homogeneous set of model grids computed in LTE and select particular elements with which to compute non-LTE deviations in a particular wavelength regime. This is far less expensive than implementing non-LTE in full and produces reliable results over a large range of stellar parameters (e.g Nieva & Przybilla, 2007; Bergemann et al., 2012b; Cunha et al., 2015).

3.3 Quantitative Analysis of near-IR Spectroscopy

To compare stellar model atmospheres with near-IR spectroscopic observations, synthetic spectra are calculated. By calculating synthetic spectra from a grid of model atmospheres with a range of physical parameters, one can then compare the models with observations and determine the model, and hence the stellar parameters, that best reproduces the data. There are four model parameters that are considered to affect the appearance of the spectra: global metallicity ($\log(Z/Z_{\odot}) = [\mathrm{Z}]$), effective temperature ($T_{\rm eff}$), surface gravity ($\log g$) and microturbulence (ξ). Microturbulence is a non-thermal velocity that is

included in quantitative analyses of stellar spectroscopic observations in order to fit the observed line profiles. For MS stars, empirical microturbulence velocities are thought to be connected with convective overshoot motions in stellar atmospheres (Cantiello et al., 2009) and/or the result of high-order non-radial pulsations (e.g. Aerts & Rogers, 2015).

The synthetic spectra used in this analysis cover the J-band, specifically the 1.16–1.22 μm region. The wavelength range is chosen based on the spectral appearance of the region. Typically, in the spectra of cool stars, dense molecular absorption features dominate the spectrum, which require high-resolution spectroscopy to distinguish individual features and estimate stellar parameters (e.g. Cunha et al., 2007; Davies et al., 2009a,b). However, in this small wavelength range, the absorption is dominated by well-separated elemental absorption features from iron, magnesium, silicon and titanium. Therefore, the spectral resolution required to estimate stellar parameters is significantly reduced. This means that this analysis, unlike others at higher resolution, can be performed with a relatively small amount of telescope time using near-IR multi-object spectrographs such as KMOS on the VLT or the multi-object spectrometer for IR exploration (MOSFIRE) on Keck and is therefore feasible for studies of large populations of RSGs in external galaxies.

In addition, given the cool temperature of the outer layers of RSGs, the peak brightness of a typical RSG is at $\sim$1.1 μm. Combining this with the fact that dust attenuation is significantly lower in the near-IR, than in the optical regime, RSGs are ideal candidates to be studied at large distances.

At near-IR wavelengths, the effects of absorption and emission from the Earth's atmosphere are a considerable complication. Although an absorption line may be strong and well separated from other stellar features, it may be contaminated by features arising from the Earth's atmosphere. If a stellar feature is contaminated with strong absorption or emission arising from the Earth's atmosphere (telluric or sky line respectively), the correction required to divide or subtract the non-stellar feature may well leave behind residuals that perturb the line strength and/or shape. For example, in Figure 3.1, there are two strong iron lines around 1.16 μm in the synthetic spectrum (top panel), that are well separated and could be suitable for the estimation of stellar parameters. However, when telluric contamination is taken into account, the size of the telluric absorption around these lines is comparable to the strength of the lines (middle panel). By correcting for the effects of the Earth's atmosphere, a significant uncertainty is introduced in

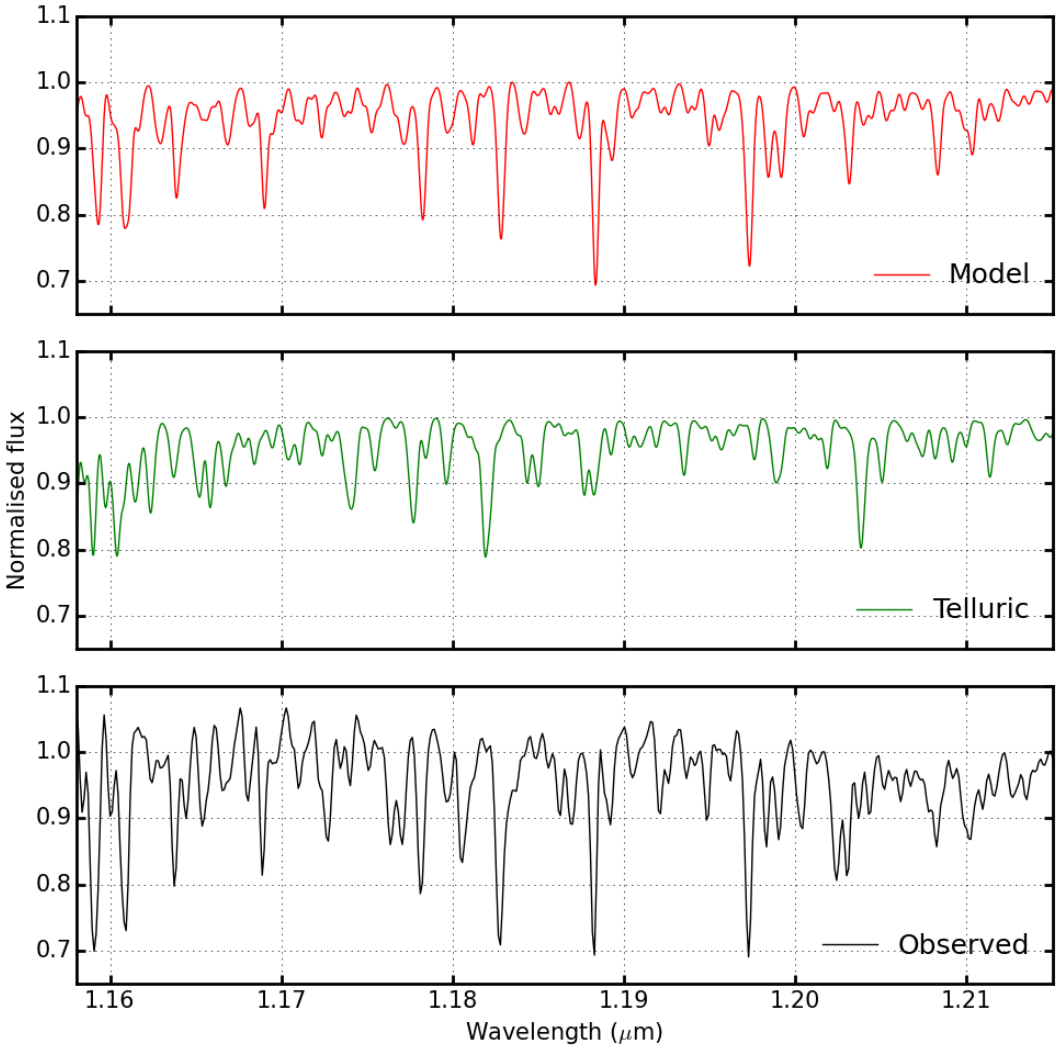

Figure 3.1 *Three panels showing the effect of telluric absorption on spectral lines. The top panel shows a synthetic RSG spectrum within the wavelength range of interest, the middle panel shows a theoretical model spectrum of the Earth's atmosphere and the bottom panel shows an observed KMOS spectrum prior to telluric correction, which, in theory, is a combination of the top two panels and a noise spectrum. To illustrate that the lines used in the analysis must come from regions where there is little telluric contamination, I draw the reader's attention to the two strong iron lines at 1.16 μm. Even though these lines are well separated in the model spectra, telluric contamination renders these lines unsuitable for the estimation of stellar parameters and one can see that the shape and strength of these lines is altered by strong telluric contamination.*

the strength and shape of these lines. Therefore, these lines are unsuitable to be used to measure stellar parameters. Equally, Figure 2.10 demonstrates that sky emission lines can also leave behind significant residuals that can perturb stellar features. The diagnostic features must therefore be chosen carefully not only by examining the model RSG spectra, but also by taking into account potential reduction residuals arising from the Earth's atmosphere. However, if one observes above the Earth's atmosphere, these lines – and many others – could be used to estimate stellar parameters.

The synthetic spectra used in this analysis are calculated from stellar model atmospheres computed from the MARCS model atmospheres project (Gustafsson et al., 1975, 2008). These model atmospheres are "classical" type models computed in one-dimension (i.e. spherically symmetric), where hydrostatic equilibrium, mixing-length theory of convection and LTE are assumed. The MARCS model atmospheres are particularly general and widely applicable to many different types of stars and as such are well used and tested. However, for the atmospheres of RSGs, the assumptions that go into these models (LTE in particular) are known to break down (Freytag, Steffen & Dorch, 2002; Plez, 2010). Therefore, in order to precisely analyse the spectra of RSGs, additional corrections must be applied (Bergemann et al., 2012a).

The MARCS model atmospheres used for this analysis are computed with a mass of $15\,M_{\odot}$. The typical mass range of an RSG is $8 \leq M/M_{\odot} \leq 40$, however, using this mass is applicable, as altering the mass of these models affects only the extension (or geometrical thickness) of the atmosphere, which does not change substantially for red giants or supergiants.

To improve the accuracy of the model atmospheres, non-LTE calculations have been performed for all elements that give rise to the diagnostic features within the wavelength range studied (Bergemann et al., 2012a, 2013, 2015). The line formation calculations of all known transitions of important atoms and molecules are computed in non-LTE using the DETAIL code (Giddings, 1981). DETAIL is a well-tested and widely used code that is used to solve statistical equilibrium equations to obtain non-LTE level populations. Using these level populations, line profiles and synthetic spectra – with non-LTE corrections for the key diagnostic lines – are calculated using an updated version of the SIU code (Reetz, 1999; Bergemann et al., 2012a), which employs the same input physics as DETAIL. By calculating synthetic spectra from a grid of stellar models, one can evaluate the combination of model stellar parameters that best reproduces the observed data.

Table 3.1 *Model grid parameter space*

Parameter	Abbreviation	Range	Increment
Global metallicity	$[Z]$	+1.0 to −1.0	0.1 dex
Effective temperature	$T_{\rm eff}$	3400 to 4400	100 K
Surface gravity	$\log g$	+1.0 to −1.0	0.25 dex
Microturbulence	ξ	1.0 to 5.0	0.2 km s^{-1}

The parameters of the resulting grid of synthetic spectra are detailed in Table 3.1, where the spectral resolving power is $R = 10\,000$, which is significantly higher than the typical resolving power of the observed spectra (i.e. $R \sim 3000$). The sensitivity of each diagnostic line for a given free parameter is illustrated in Figures 3.2 to 3.5 in which one parameter is varied and the remaining are fixed.

From an analysis of Figures 3.2 and 3.3, one can see that the effect of increasing the metallicity of the models is similar to that of decreasing the surface gravity. It is therefore expected that a degeneracy exists between metallicity and surface gravity. This degeneracy is explored further in Section 3.5.

The effect of varying the temperature of the models changes the relative strengths of the lines of different spectral species. For example, see the left panel in Figure 3.4, where the ratio of the iron ($\lambda\,1.188285$) to titanium ($\lambda\,1.189289$) lines is strongly affected by varying the temperature of the models. Also note that each species does not respond linearly to temperature. This can be seen by a comparison between the strength of the iron line ($\lambda\,1.197305$) in the right-hand panel of Figure 3.4 and that of the silicon lines ($\lambda\lambda\,1.198419, 1.199157$) in the same panel. This is clearly distinguishable from the effects of all other parameters.

Increasing the microturbulence has the effect of increasing the equivalent widths of the strongest lines preferentially, as well as affecting the relative strengths of the lines arising from the same spectral species. Therefore, strong features arising from the same element will be most sensitive to this parameter. This is illustrated by a comparison between the two strong iron lines ($\lambda\lambda\,1.188285, 1.197305$) in the left and right panels of Figure 3.5. The iron line in the right panel is strongest at $\xi = 1.0$, whereas at $\xi = 5.0$ the iron line in the left panel is the stronger of the two. In addition, the relative strengths of the two silicon lines ($\lambda\lambda\,1.198419, 1.199157$) in the right-hand panel of Figure 3.5 are not strongly affected, which illustrates that microturbulence preferentially affects the strongest spectral features.

The current model grid is sufficient to explore the parameters for a typical RSG

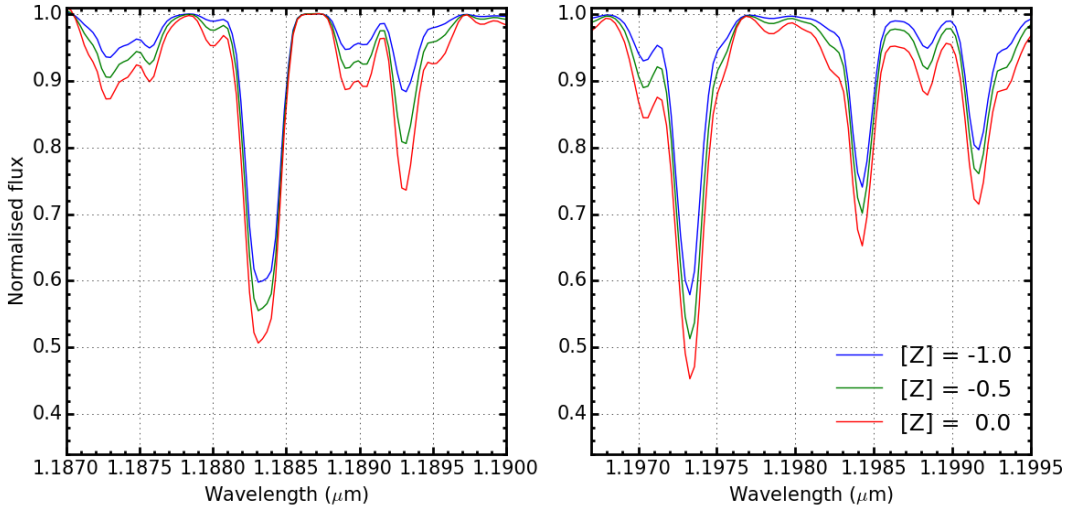

Figure 3.2 *Three example models in which only the metallicity is varied; the remaining stellar parameters are fixed at $T_{\rm eff}$ = 3900 K, $\log g$ = 0.0 and ξ = 3.0 km s^{-1}. Five diagnostic lines are shown in the two panels. Left: Fe I λ1.188285 and Ti I λ 1.189289. Right: Fe I λ1.197305 and Si I λλ 1.198419, 1.199157.*

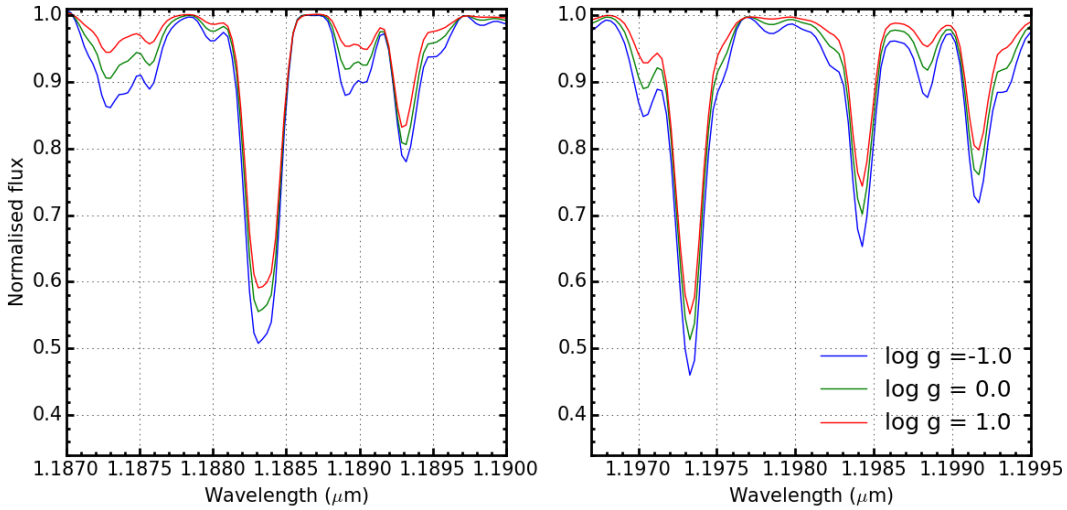

Figure 3.3 *As in Figure 3.2 where surface gravity is varied, and the remaining parameters are fixed at [Z] = −0.5, $T_{\rm eff}$ = 3900 K and ξ = 3.0 km s^{-1}.*

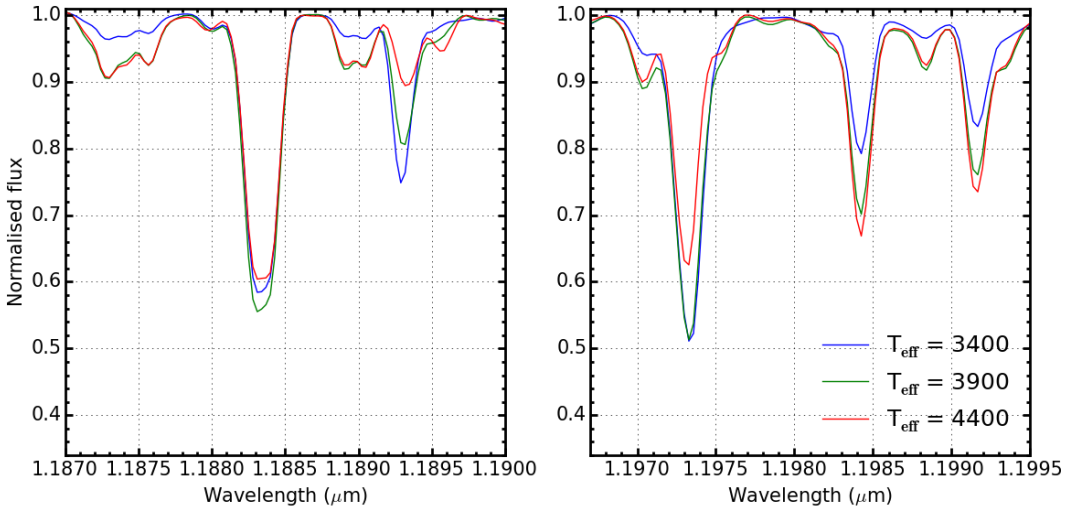

Figure 3.4 *As in Figure 3.2 where effective temperature is varied, and the remaining parameters are fixed at [Z] = −0.5,* $\log g = 0.0$ *and* $\xi = 3.0\,km\ s^{-1}$.

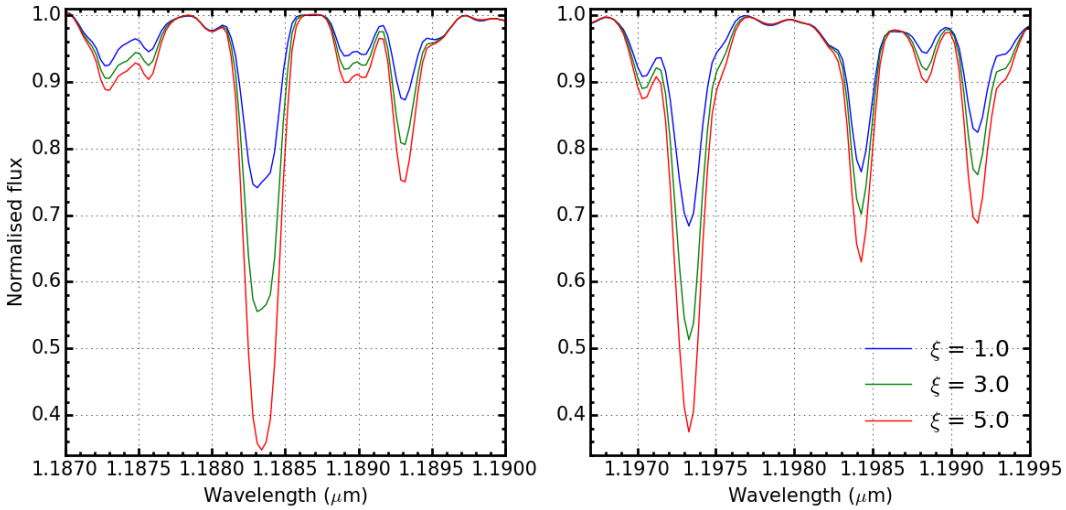

Figure 3.5 *As in Figure 3.2 where microturbulence is varied, and the remaining parameters are fixed at [Z] = −0.5,* $T_{\rm eff} = 3900\,K$ *and* $\log g = 0.0$.

in the Local Universe. However, when using this technique at larger distances, many different metallicity environments are encountered, e.g. the low-metallicity environment of I Zw 18 with $Z = (1/32)Z_{\odot}$ (Vílchez & Iglesias-Páramo, 1998). In order to study these extremely low-metallicity systems, the parameter space would need to be extended.

The α-to-iron ratio of these stars is taken to be that of the solar value (i.e. $[\alpha/\mathrm{Fe}] = 0.0$) and is not yet left as a free parameter in the models. This is one of the main limitations of the models presented and will be an area for improvement in the future (see Chapter 7). Davies et al. (2015) compiled a literature study of abundances in the Magellanic Clouds, which appears to show that there is no evidence for departures from a Solar-like α-to-iron ratio within ± 0.1 dex. In addition, using a slightly different line list to the one used in this study, these authors explored the effect of altering this ratio and found that varying the α-to-iron ratio by ± 0.1 dex results in a corresponding shift in [Z] of ± 0.1 dex, i.e. within the quoted typical uncertainty of [Z]. In the current implementation, this effect is expected to be smaller owing to the enhanced line list used in this study, particularly as the additional diagnostic lines included here (in comparison with Davies et al., 2015) are two lines of magnesium.

3.4 Continuum Fitting

Accurately matching the continuum levels in the observed spectrum provides a base that provides an anchor to the comparison of the diagnostic lines of the models. An incorrectly placed continuum level would bias the analysis and result in the strength of the diagnostic lines being over- or under-estimated, producing inaccurate stellar parameters.

There are many factors that affect the level of the continuum and continuum placement, including the resolution of the observations and the stellar parameters themselves. Therefore, it is vital that, when estimating stellar parameters in crowded spectral regions such as this, the continuum placement is performed consistently and accurately. Intrinsically, when studying RSGs at medium resolution – owing to their cool atmospheres – there are many instances of blended spectral features. At this resolution the density of blended spectral features creates a pseudo-continuum that, in practice, is never at the true continuum level. Figure 3.6 illustrates the varying continuum levels for models where the

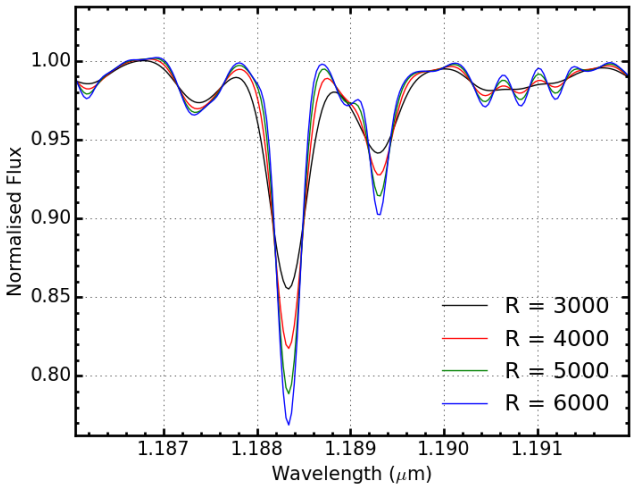

Figure 3.6 *A model spectrum degraded to four different resolution values. This figure demonstrates how the continuum level changes depending upon the resolution of the spectrum. We see at around 1.191 μm at R = 3000 that the continuum level is perturbed by blended lines.*

resolution is varied and Figures 3.2–3.5 demonstrate that varying each of the stellar parameters affects the continuum in a subtly different manner.

Given that it is impossible to know the true continuum level from any given observation, the scaling applied must be consistent between the models and observations. Scaling is required not only to match the levels of the continuum placement, but also to match the line strengths between the models and observations. Providing the treatment of the models and observations is consistent, the fact that the true continuum is never attained is not significant (Gazak et al., 2014b). For the process of continuum matching to work effectively, the observed and model spectra should be at the same resolution, have a consistent wavelength calibration and have identical spectral sampling.

In order to account for differences in the spectral sampling of the observed and model spectra, each model spectrum is resampled onto the wavelength scale of the observations by means of a spline interpolation routine. The model spectrum is then degraded to the resolution of the observations (R) by a convolution with a Gaussian filter, where the width of the Gaussian is defined by the observed resolution ($FWHM = \sqrt{(\lambda/R)^2 - (\lambda/R_{mod})^2}$, where R_{mod} is the spectral resolving power of the model spectrum). The spectral resolving power of the KMOS observations is estimated using the KMOS/esorex pipeline from arc lamp exposures at the appropriate rotator angle for the observations. This is

measured for each spectrograph and is assumed to be constant (to within ± 100) across individual IFUs as well as across the detector.

To ensure the spectra are on the same wavelength scale, the observed spectrum is cross-correlated with the model spectrum; a shift is then applied to the model spectrum in order to minimise the cross-correlation matrix. This procedure is repeated until the shift between the observed and model spectra is less than 0.1 pixel. Over this small wavelength range, one would not expect significant variations in the spectral resolution of the observations to perturb the cross-correlation.

Once the spectra have been correctly matched, they can be compared over the wavelength range 1.16–1.22 μm. To estimate the amount of scaling required, first I define the continuum width (cw) as,

$$cw = \frac{\lambda}{R}, \tag{3.12}$$

where R is the resolution of the spectrum and λ is the wavelength at which the width is taken (in principle, this wavelength varies across the spectrum; however, given our spectral window is sufficiently small, I assume $\lambda = 1.20\,\mu$m). The continuum width is essentially the resolution element of the spectrum at a wavelength of $\lambda = 1.20\,\mu$m.

The model spectrum is divided into wavelength slices, each of width $cw\,\mu$m, and the maximum of each slice is taken. Using this array of maxima, any major feature is systematically removed by rejecting data points more than $3\,\sigma$ from the mean of the distribution. Figure 3.7 illustrates the width of these slices and how this technique removes prominent spectral features. In this figure, blue points represent the boundaries between the slices of width $cw\,\mu$m and the maximum of each slice is shown in red.

The remaining data points (P_{cont}) are used to derive an initial correction function (cf_{init}) by fitting a third-order polynomial to the ratio of the model to observed continuum points (red points in Figure 3.7), defined using the equation,

$$cf_{init} = f\left(\frac{F_{mod}(P_{cont})}{F_{obs}(P_{cont})}\right), \tag{3.13}$$

where F_{mod} and F_{obs} are the flux in the model and observed spectrum respectively.

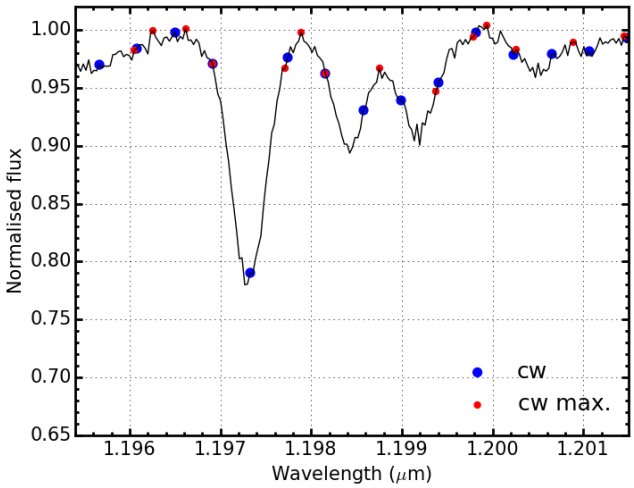

Figure 3.7 *Illustration of the scale of the continuum width (cw) in comparison with typical diagnostic lines. The solid black line shows an example of a model spectrum degraded to $R = 3000$, including a small noise contribution. The blue points show where the continuum width is sliced and the red points show the maximum of each slice. These maxima are then used to define the continuum fitting function.*

The final correction function (cf_{fin}), a refinement of cf_{init}, is defined by removing any remaining outliers more than 3σ from the mean of the initial correction function. This method assumes that, over the small wavelength range considered, cf_{init} does not vary significantly from the mean and, as such, any significant deviation is considered as originating from a spectral feature or noise.

The final correction function, cf_{fin}, is used to define the amount of scaling required for the model. Figure 3.8 demonstrates how the continuum-fitting process works by showing the observed spectrum (in this case is an example model spectrum; black solid line) alongside the unscaled model spectrum in the top panel (red solid line); the continuum points – derived from the model spectrum – are used to define cf_{fin} are shown in the middle panel, and the final correction function and the corrected model spectrum are shown in the bottom panel. In addition, Figure 3.9 shows, on a smaller scale, how the continuum points – and hence the the final correction function – are defined. It can be seen from these two figures that the continuum placement of the example observed spectrum and that of the scaled model spectrum are well matched.

Alternative methods of continuum fitting are discussed in Davies, Kudritzki & Figer (2010) and Evans et al. (2011a). These methods select pseudo-continuum pixels in the models by ranking the model pixels and selecting a percentage of

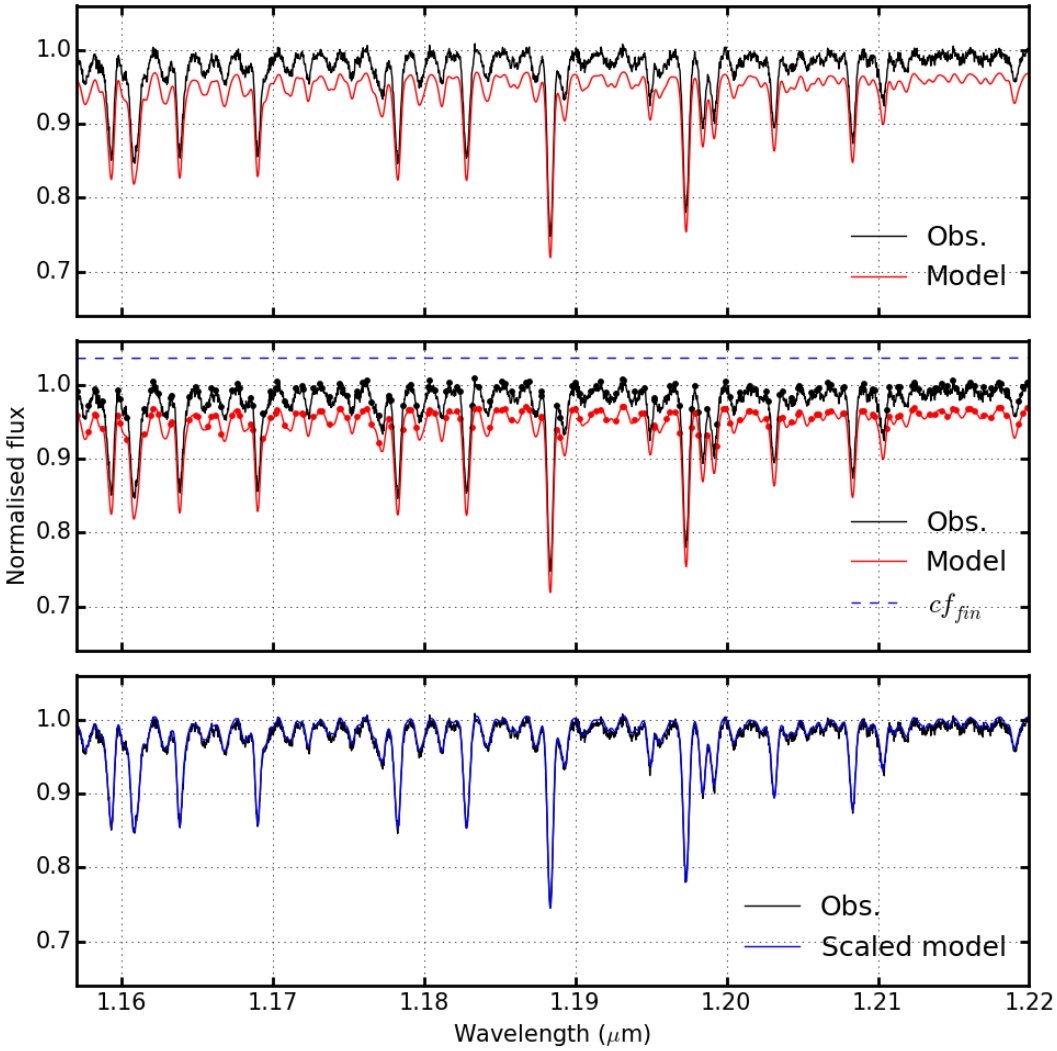

Figure 3.8 *Three panels showing an example of how the continuum-fitting process works using a model spectrum as an example observed spectrum (with a small contribution from noise; black solid line) and the same model spectrum, with a constant offset applied (red solid line). The top panel shows the observed spectrum (black solid line) compared with the unscaled model spectrum (red solid line), the middle panel overlays continuum points in the observed ($F_{obs}(P_{cont})$; black points) and model spectra ($F_{mod}(P_{cont})$; red points) and displays the final continuum function (cf_{fin}; blue dashed line), which is defined from the ratio of these points (equation 3.13). The bottom panel shows the observed spectrum (black solid line) with the corrected model spectrum (blue solid line) compared with the latter having been scaled by the blue dashed line in the middle panel.*

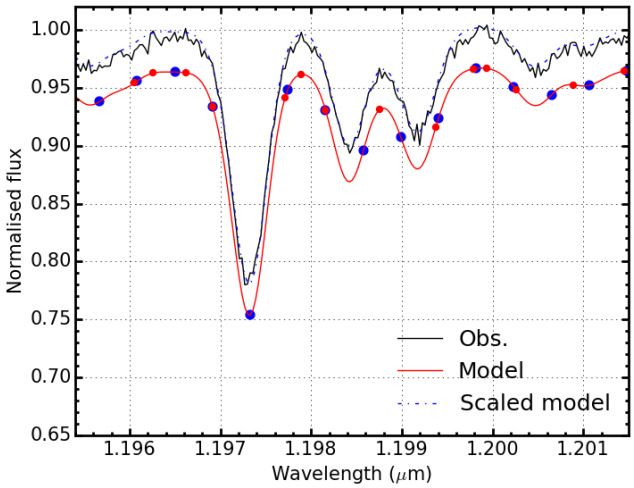

Figure 3.9 *An example of the continuum-fitting procedure using a model spectrum as an example observed spectrum (black solid line) and a separate model spectrum to match the level of the continuum. The red solid line shows the model spectrum before any scaling has taken place. The dot-dashed blue line shows the model spectrum after the continuum-fitting scaling has been applied. The red and blue points indicate the edges of the slices made and maxima of these regions respectively. For these models, the true continuum level is at 1.00.*

the pixels with the largest flux. Providing the pixels from the model are selected in this manner and not those in the observations, this is a reliable method with which to derive the continuum level as demonstrated by Davies et al. (2015).

3.5 Best-fit Parameters

Best-fit parameters are calculated using a maximum likelihood approach, where the χ^2-statistic is computed to compare the model (M) and the observed (O) spectra. The χ^2-statistic is calculated using the equation,

$$\chi^2_\nu = \frac{1}{N_{pix} - \nu} \sum_i \frac{(O_i - M_i)^2}{\sigma^2}, \tag{3.14}$$

where N_{pix} is the number of pixels used, ν is the number of degrees of freedom and σ is determined by the S/N of the spectrum. This statistic is calculated for each of the diagnostic lines, where N_{pix} is the total number of pixels within each line. Table 3.2 details the diagnostic lines used in this analysis. The amount of

Table 3.2 *Diagnostic lines used to estimate stellar parameters ordered by wavelength, by species*

Species	Line centre (μm)
Fe I	1.188285
Fe I	1.197305
Si I	1.198419
Si I	1.199157
Si I	1.203151
Si I	1.210353
Ti I	1.189289
Ti I	1.194954
Mg I	1.182819
Mg I	1.208366

continuum included to compute the χ^2-statistic is important to consider. If this wavelength range is too small, the wings of the lines will be neglected, which would discard vital information used to constrain the model parameters. However, if too much of the pseudo-continuum is included, the parameters could be biased by noise features in the observations or by inaccuracies within the models.

The regions which are used in the calculation of the χ^2-statistic are highlighted in blue in Figure 3.10. From a careful analysis of the individual spectra, the exact regions over which to compute the χ^2-statistic are adjusted slightly depending upon the quality of the reduction and the appearance of reduction residuals near any lines of interest.

As a conservative estimate, for testing purposes, I use 10 regions corresponding to the cores of the individual lines. In practice, however, given that there are several lines that are sufficiently close together, at R $\sim$ 3000 the lines are not clearly separated. In these instances, the most appropriate course of action is often to define a region which encompasses all of the spectral features in question. For example, the Fe Iλ1.188285 and the Ti Iλ1.189289 or the Fe Iλ1.197305 and the Si I$\lambda\lambda$1.198419, 1.199157 lines often are covered by one region to ensure that specific pixels are not counted multiple times.

The best-fit parameters are estimated based on a sampling of the posterior probability density function using EMCEE Foreman-Mackey et al. (2013), an implementation of the affine-invariant ensemble sampler for Markov chain Monte Carlo (MCMC) of Goodman & Weare (2010). The probability function used is,

$$p(D|\{[Z], \log g, T_{\rm eff}, \xi\}) = \exp(-\chi^2_v/2), \tag{3.15}$$

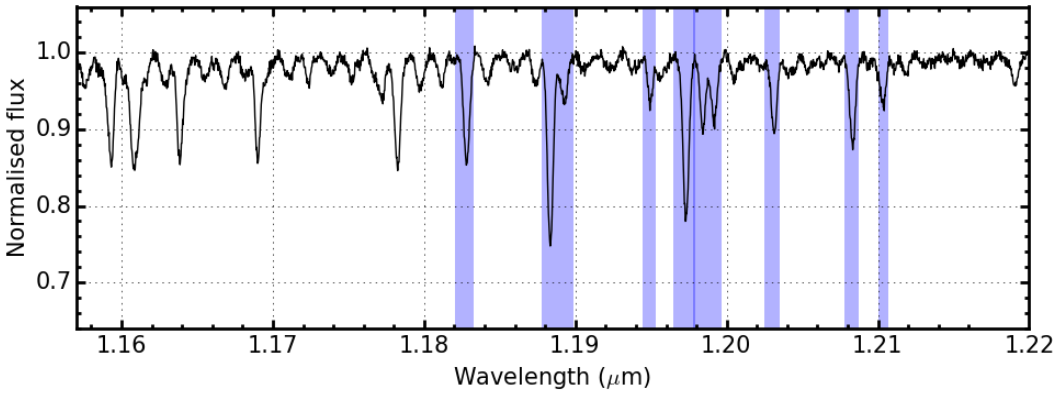

Figure 3.10 *An example of a model spectrum, degraded and resampled to that of a typical observed spectrum, with a small noise contribution added. The blue shaded regions illustrated the wavelength range used to compute the χ^2 calculation.*

where the data (D) consists of the observed spectra and χ^2 is calculated as given by equation 3.14.

The initial guess for each run of the MCMC sampler is calculated by the weighted average of the ten models with the lowest χ^2_v, where the weights for the average are given by $w = \exp(-\chi^2_v/2)$. The guess is varied assuming a Gaussian distribution with a mean value centred on the initial guess and the standard deviation is chosen such that, for each parameter, the guesses sample a small volume of parameter space. The full grid of parameter space is explored from the initial guesses.

To aid the *a priori* assumptions, if broad-band photometry is available for the objects in question (which is nearly always the case given that the most common way to select RSGs is based on the optical or near-IR colours), this information is used to restrict the available range in parameter space. To do this, the luminosity of the star is calculated using the bolometric corrections of Davies, B. et al. (2013), where the photometric band used is preferably the K-band to minimise the effects of interstellar extinction. This is done by combining the two equations that were previously described as two of the fundamental equations for stellar atmospheres (equations 3.1 and 3.2) to arrive at the expression,

$$\frac{g}{T_{\rm eff}^4} \propto \frac{M}{L}. \tag{3.16}$$

By assuming sensible limits on the masses of RSGs, which are thought to be in the range $8 \leq \mathrm{M/M_\odot} \leq 40$, one can restrict the available range of the $\log g$

parameter by calculating upper and lower estimates at every $T_{\rm eff}$ grid space. The models that have $\log g$ values outside of this allowed range are rejected as not physical. This helps to minimise the number of χ^2 calculations performed and also helps to break the $\log g$-[Z] degeneracy within the models. In addition, if mass restrictions can be estimated, the available parameter space can be further restricted.

The best-fit parameters and errors are calculated by drawing at least 200 000 independent samples from the probability density function (rejecting the first half of the results as "burn-in") and computing the $16^{\rm th}$, $50^{\rm th}$ and $84^{\rm th}$ percentiles as defined from these samples. The quoted value for each parameter is then,

$$x^{+\sigma_{high}}_{-\sigma_{low}}, \tag{3.17}$$

where x is the $50^{\rm th}$ percentile, σ_{low} is the $50^{\rm th} - 16^{\rm th}$ percentiles and σ_{high} is the $84^{\rm th} - 50^{\rm th}$ percentiles. In practice, the upper and lower error bounds are sufficiently consistent for the average of the two values to be taken. An exception to this is when a model parameter is on, or near, the edge of the available grid. In this case, the largest of the upper and lower error bounds are quoted as the error. The minimum allowed error on any given parameter is 1/2 of the grid spacing of the parameter in question, the error is set at this limit (i.e. $\xi_{err} = 0.1\,{\rm km\ s^{-1}}$, $[{\rm Z}]_{err} = 0.05\,{\rm dex}$, $\log g_{err} = 0.13$ and $T_{{\rm eff}\,err} = 50\,{\rm K}$). However, as Section 3.6 details, the surface gravity parameter is the most uncertain, therefore, the minimum error on this parameter is set at one grid spacing (i.e. $\log g_{err} = 0.25$).

3.6 Calibration

To test the internal accuracy of this method of parameter estimation, two main tests are devised, which involve simulating observed data with simulated RSG spectra of which the input parameters are known:

i simulated spectra at model resolution and high S/N, and

ii simulated spectra at typical observed resolution and S/N.

Table 3.3 *Fit results to the best-fit parameters for simulated spectra tests*

Parameter	test i		test ii	
	m	b	m	b
ξ	0.02 ± 0.03	-0.01 ± 0.14	-0.04 ± 0.09	-0.16 ± 0.33
[Z]	-0.01 ± 0.04	-0.00 ± 0.01	-0.00 ± 0.10	-0.02 ± 0.04
$\log g$	0.00 ± 0.07	-0.00 ± 0.05	0.16 ± 0.19	-0.01 ± 0.11
$T_{\rm eff}$	-0.05 ± 0.04	196 ± 130	-0.03 ± 0.13	-100 ± 500

In these tests, the resolution of the models is degraded using a Gaussian filter, where the width of this function is determined by the output resolution (as described in Section 3.4). Once the spectra have been degraded (if applicable), random Gaussian noise with μ =0.0 and $\sigma = 1/(\mathrm{S/N})$ is added to each spectral channel. The result of this process is an idealised simulated observed spectrum with known input parameters (idealised, in the sense that this method assumes that no reduction residuals are present). By comparing the parameters used to create the spectra (input) with the results of the analysis routine described above (output), one can assess the effectiveness and limitations of this analysis.

Figure 3.11 shows the results of test i using 18 simulated RSG spectra, which show that in the simplest of tests this method is able to recover input parameters well. A liner fit to the data in each of the panels, where the parameters are estimated using a simple MCMC routine, is also shown with the dashed red lines in Figure 3.11. In all cases, the gradient and the intercept of the fits are consistent with zero. Table 3.3 shows the results of these fits, which confirm – for test i – there appears to be no significant systematic offsets (b) or relationship (m) between the input and output parameters, however the gradient of the fit to the surface gravity could point to a potential systematic uncertainty in the determination of this parameter. For illustration, in this figure, the errors have not been set to the minimum value of 1/2 grid spacing (1 for $\log g$). This allows one to get a sense of how often this occurs for each parameter. For a total of 18×4 parameter estimates, this occurs five times.

The results of test ii are displayed in Figure 3.12, where again a linear fit to each set of results is displayed with a red dashed line. The results of these fits are detailed in Table 3.3. These results show that there are no significant systematic offsets within the analysis routines. As in test i, a potential trend in surface gravity output parameters has been identified. The difference between the input and output surface gravity parameters appears to be most significant at the edges of the model grid. Owing to the low significance of this result, and the fact that

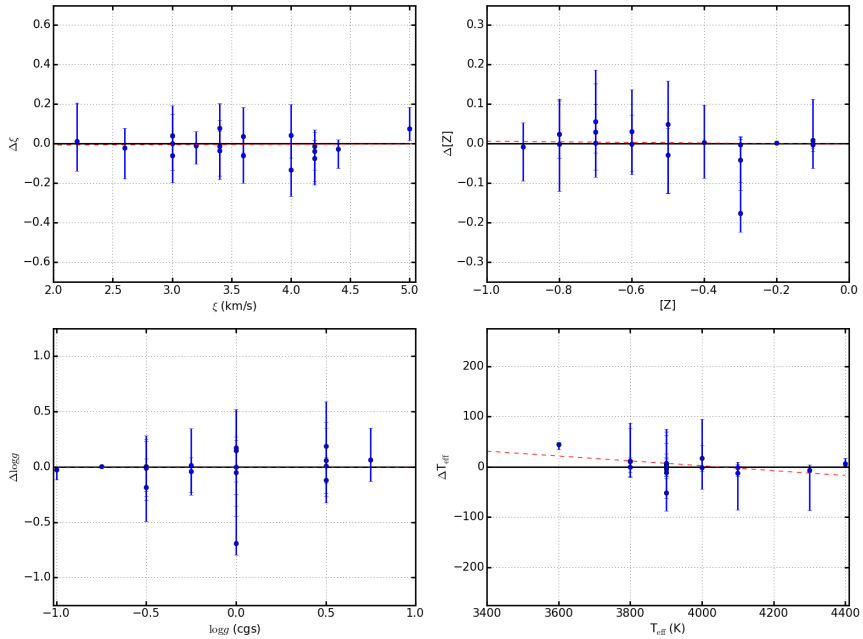

Figure 3.11 *Analysis test i: input and output parameter comparison for simulated spectra. Model parameters used to generate simulated spectra are shown against the difference between the model parameters and the results of the analysis routine (ΔX = input − output). Simulated spectra are generated from models by including random Gaussian noise ($S/N = 150$) and are degraded to $R = 10\,000$. This figure demonstrates the accuracy of the analysis routine presented in an idealised test.*

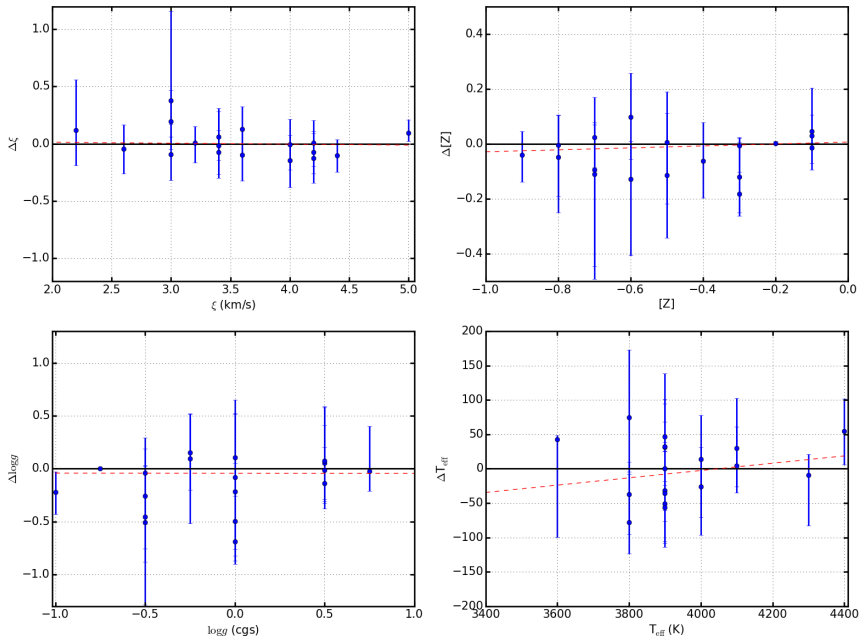

Figure 3.12 *Analysis test ii: input and output parameter comparison for simulated spectra. Model parameters used to generate simulated spectra are shown against the difference between the model parameters and the results of the analysis routine (ΔX = input − output). From top to bottom, left to right: microturblence (ξ, global metallicity ([Z]), surface gravity ($\log g$) and effective temperature ($T_{\rm eff}$). Simulated spectra are generated from models by including random Gaussian noise (S/N = 150) and are degraded to R = 3000. Gaussian noise is added after the spectra have been degraded. This figure shows that the analysis technique presented is (in an ideal case) able to accurately estimate stellar parameters at the typical resolution and S/N of KMOS spectra.*

no one point is more than $1\,\sigma$ discrepant, I have not implemented any correction for this result.

In general, the results of test i and ii demonstrate that there exists no significant systematic uncertainties in the estimation of stellar parameters using the method outlined in this chapter.

In addition, it is useful to characterise how the fit parameters respond to the spectral resolution and S/N of the input spectra to assess the limits of this technique, particularly in the case of low spectral resolution and/or S/N. Figure 3.13 shows input and output parameters for one model spectrum that is degraded to have different resolution values in the range $1000 < R < 10\,000$. The green dashed line in each panel represents the respective input parameters for this model. From this test we can see that the parameters appear stable to

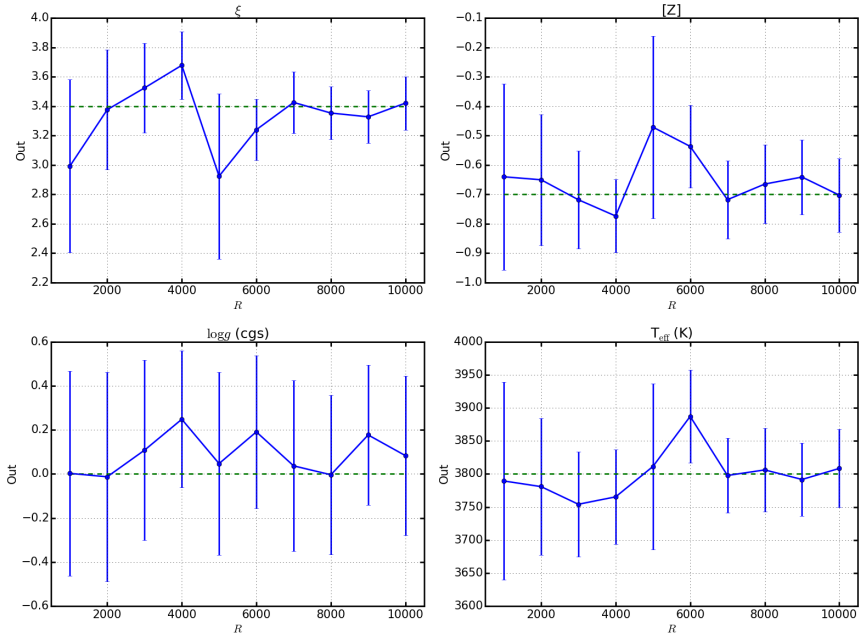

Figure 3.13 *Best-fit parameters using a single simulated RSG spectrum generated from a model spectrum by including random Gaussian noise (S/N = 150) degraded to resolution values in the range 1000 < R < 10 000 (and resampled onto the typical sampling for an KMOS spectrum).*

below $R = 3000$, which is significant, as the resolution of KMOS in the YJ-band is typically $3000 < R < 4000$. In addition, the uncertainties on the surface gravity parameter appear to be insensitive to the input resolution. Note that the uncertainties on the parameters in Figure 3.13 are stable beyond R $\sim$ 5000 owing to the intrinsic uncertainties in the models.

Figure 3.14 shows that best-fit parameters for a single simulated RSG spectrum degraded to a resolution of $R = 3000$ (and resampled onto the typical sampling for an KMOS spectrum) at varying S/N ratios. This figure shows that, at the S/N ratios which are typical of KMOS observations of RSGs, this technique is able to accurately estimate fit parameters. I note, however, that, as the S/N of real spectra decreases, the contribution of residuals from the reduction process becomes increasingly important. Therefore, for real observed data, we expect this analysis routine to break down at below S/N = 100 at $R = 3000$.

As the analysis routine described above has been shown to be internally consistent, the natural next step is to compare the results of this technique with other similar techniques. This helps to increase confidence in the accuracy and reliability in applying spectral fitting in the J-band to RSGs in general, as well

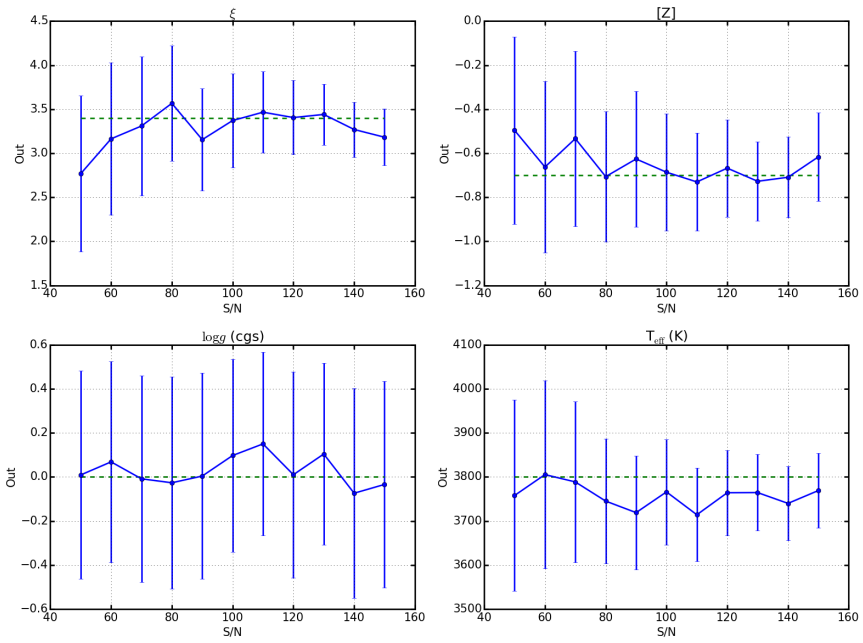

Figure 3.14 *Best-fit parameters using a single simulated spectrum degraded to a resolution of $R = 3000$ (and resampled onto the typical sampling for an KMOS spectrum) at varying S/N ratios in the range $50 < S/N < 150$.*

as to provide a vital test on the effectiveness of the technique described in this thesis.

There are currently two other published analyses using medium resolution J-band spectra of RSGs to estimate stellar parameters, those of Davies, Kudritzki & Figer (2010, DKF10) and Gazak (2014, G14). Both of these approaches use different assumptions to estimate the stellar parameters from a similar model grid.

The main differences between the two methods are that DKF10 uses the strengths of several diagnostic lines to compute the χ^2-statistic, while G14 uses a more extended region within 1.16–1.22 μm, where several key diagnostic lines are present.

In the current analysis, the shape and strength of the diagnostic lines are used to calculate the χ^2-statistic. This is preferred to the two aforementioned techniques for the following reasons:

i The models used are not perfect representations of RSG spectra. The line list which is used to create these spectra is known to be incomplete and the

effect of including these wavelength regions within the χ^2 calculation could be to perturb the fit. G14 is very careful to exclude all known instances of missed lines within the models; however, this cannot be assumed to be a complete consensus of omitted features.

ii By using the full line profile of the diagnostic lines, one can use the shape and strength of the lines to break degeneracies between model parameters.

In addition, an updated line list is used in the current study. This update includes the non-LTE effects on two strong magnesium lines within the region (Bergemann et al., 2015). In Chapter 5, the difference between including and excluding these magnesium lines is explored.

To date there have been several published articles using the DKF10 analysis (Davies, Kudritzki & Figer, 2010; Davies et al., 2015; Patrick et al., 2015). This technique has been updated and tested rigorously on VLT-XSHOOTER spectra of RSGs in the Magellanic Clouds in Davies et al. (2015), and in Patrick et al. (2015, which Chapter 5 is based upon) this was applied to KMOS spectra in NGC 6822.

Here, I compare the DKF10 analysis method with that presented in this thesis. To do this, I compare the output from both routines on three datasets:

i 18 simulated RSG spectra at a S/N and resolution comparable to that of the observations (i.e. test ii),

ii the KMOS observations in NGC 6822, presented in Patrick et al. (2015),

iii and the KMOS observations in NGC 2100, presented in Patrick et al. (2016).

In Patrick et al. (2015), the results are calculated using the DKF10 analysis whereas in Patrick et al. (2016), the routine used is that presented in this chapter.

These tests assess how the two routines compare on simulated data as well as real data. This is important as simulated spectra allow one to compare the accuracy of the routines, when compared to the input parameters. Whereas, comparing the routines using real spectra tests the reliability of the two routines, when compared to each other.

Figures 3.15, 3.16 and 3.17 show how the estimated parameters for the three tests compare. Firstly, from an examination of Figure 3.15, it is evident that

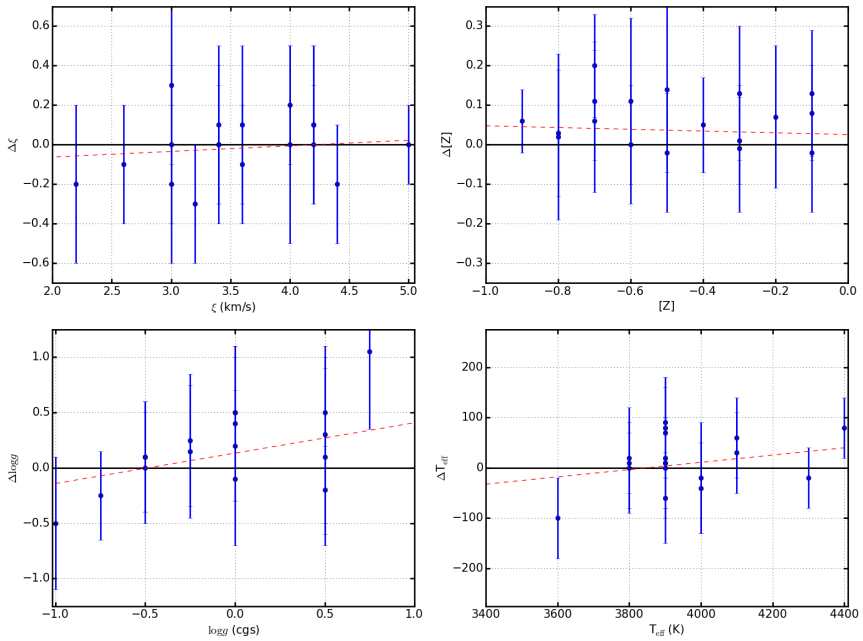

Figure 3.15 *The best-fit parameters for 18 simulated spectra analysed with routines presented in Davies, Kudritzki & Figer. Model parameters used to generate simulated spectra are shown against the difference between the model parameters and the results of the analysis routine ($\Delta X = input - output_{\mathrm{DKF}}$).*

no significant systematics exist in the DKF10 analysis. This is demonstrated by fitting a straight line to each distribution in Figure 3.15. The results of each of these fits for each parameter is listed in Table 3.4.

By examining the results of the straight line fits to each of the output parameters in Table 3.4 and by the appearance of Figures 3.15, 3.16 and 3.17, one can see that there are several interesting features of these output parameters.

The results displayed in Figure 3.15, appear to show a small systematic offset in the DKF10 output metallicity with respect to the input parameters (top right panel in Figure 3.15). The average offset between the input and output parameters is $\Delta \mathrm{Z} = 0.06 \pm 0.06\,\mathrm{dex}$. This offset is barely significant at the 1σ level however, it is an important offset to consider when comparing metallicity measurements taken by the two routines. To fully quantify this offset, more tests on simulated RSG spectra must be undertaken.

In general, the estimation of the surface gravity parameter appears to suffer from being overestimated in the low $\log g$ regime and underestimated in the high $\log g$ regime. Taken individually, Figure 3.15 does not show this convincingly, however,

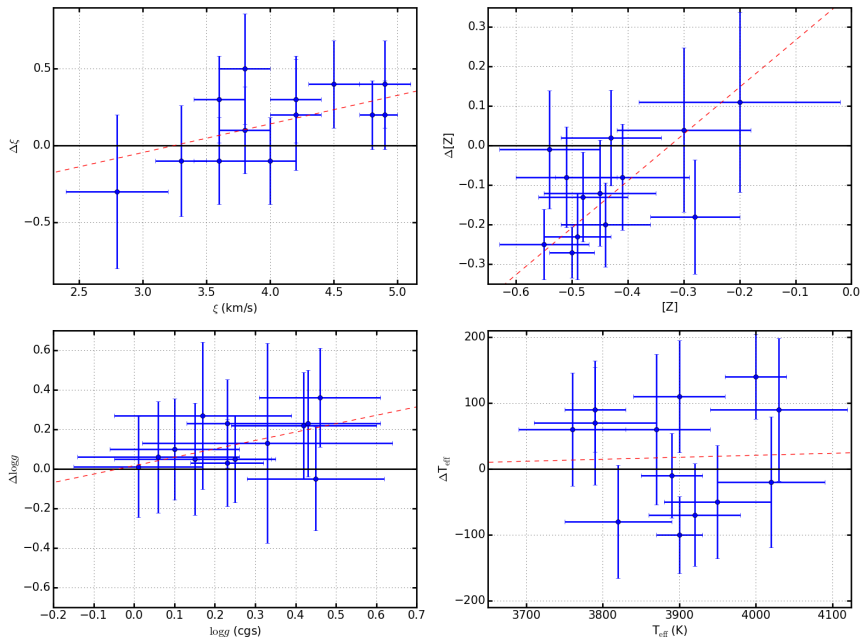

Figure 3.16 *A comparison between the best-fit parameters derived for 14 RSGs in NGC 2100 using two different analysis routines. Results published in Patrick et al. (2016) make use of the technique presented in the current chapter, DKF10 results from Davies, et al. (private communication). In this figure, ΔX is the difference between the output from the current technique and the DKF10 technique (i.e. $\Delta X = output - output_{\mathrm{DKF10}}$).*

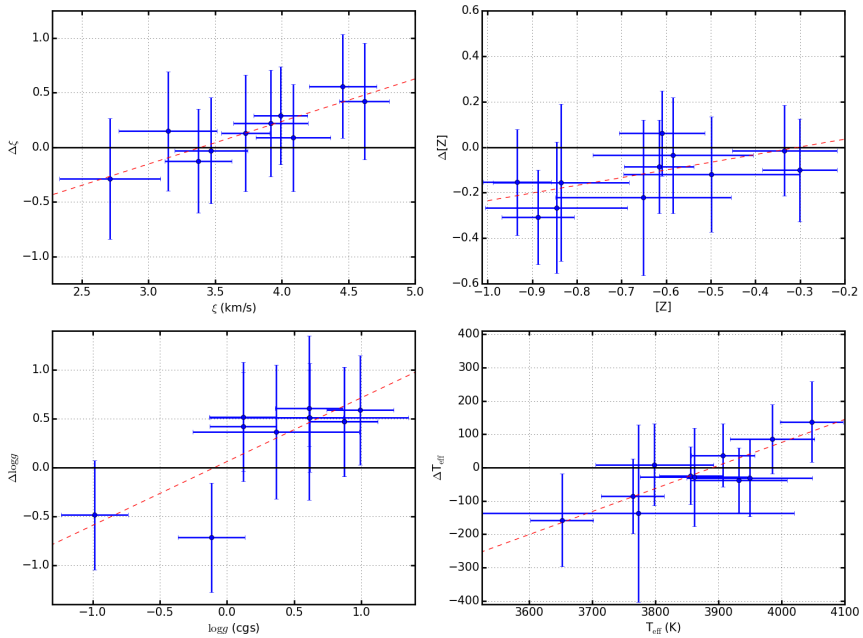

Figure 3.17 *A comparison between the best-fit parameters derived for 11 RSGs in NGC 6822 shown against the difference between the DKF10 results published in Patrick et al. (2015). As in Figure 3.16, in this figure, ΔX is the difference between the output from the current analysis and the DKF10 analysis (i.e. ΔX = output − output$_{\mathrm{DKF10}}$). Note: in this figure, I compare results excluding the Mg I lines to be consistent with those published in Patrick et al. (2015).*

when one considers that Figures 3.11 and 3.12 also show signs of this behaviour, it becomes more clear. The forms of these figures are symptoms of a parameter that prefers the centre of the model grid parameter space (i.e. $\log g = 0.0$). This appears to be present to a greater extent in the DKF10 routines as this behaviour is again viewed in both Figures 3.16 and 3.17.

In Figure 3.16, one can see that there appears to be an offset in the metallicity parameter estimated using the two different methods. In general, the present analysis, estimates lower metallicities by an average of $\sim$0.1 dex. These differences are related to the differences in the surface gravity parameter where almost exclusively, the present analysis estimates higher surface gravity by an average of $\sim$0.1 dex.

The agreement between the stellar parameters of NGC 6822 is more consistent, however, similar relationships are observed in comparisons between the parameters. On average the metallicity measurement measured in the present analysis is $\sim$0.1 dex lower than that of DKF10. In addition, and likely coupled, the surface gravity estimates are again offset by $\sim$0.3 dex. No systematic offset is observed between the effective temperature estimates.

In general, an examination of Figures 3.15, 3.16 and 3.17, demonstrate that on average there is reasonable agreement between the parameters estimated using the different routines, however, an the differences mentioned must be quantified further in future studies.

The choice of using the reduced χ^2 rather than the non-reduced must be justified, given that the number of degrees of freedom used in this statistic can sometimes be not trivial to estimate. In this definition, I have simply defined the degrees of freedom as $N_{pix} - P$, where N_{pix} is the number of pixels per stellar feature and P is the number of fit parameters. This is known to be a simplistic definition, which can lead to potential problems if, for example, the number of degrees of freedom varies across the model grid (Andrae, Schulze-Hartung & Melchior, 2010). This could manifest in accuracies in the fitting procedure towards the edges of the model grid.

Behaviour similar to this is seen to a small extent with the surface gravity fit parameter. However, the same behaviour is observed in the DKF10 analysis, which uses the non-reduced χ^2 statistic (which should not be affected by this problem). Therefore, this is potential not the origin of this uncertainty.

Table 3.4 *Fit results to the best-fit parameters for observed spectra tests. Results for test ii, NGC 2100 and NGC 6822; Figures 3.15, 3.16 and 3.17, respectively.*

Parameter	test ii		NGC 2100		NGC 6822	
	m	b	m	b	m	b
ξ	0.03 ± 0.10	-0.12 ± 0.36	0.19 ± 0.09	-0.60 ± 0.37	0.39 ± 0.04	-1.32 ± 1.63
[Z]	-0.02 ± 0.11	0.02 ± 0.06	1.19 ± 0.44	0.39 ± 0.21	0.33 ± 0.14	0.10 ± 0.09
$\log g$	0.27 ± 0.26	0.14 ± 0.12	0.43 ± 0.22	0.02 ± 0.07	0.65 ± 0.17	0.06 ± 0.11
$T_{\rm eff}$	0.07 ± 0.10	-280 ± 390	0.00 ± 0.03	-100 ± 120	0.70 ± 0.14	-270 ± 52

In tests with the χ^2_ν and χ^2, the reduced χ^2 yields more stable and realistic errors, when compared with the true input parameters. In previous versions of this analysis routine, the degrees of freedom had been optimistically estimated as N_{pix}, this yielded slightly smaller errors, however, the agreement between the best-fit parameters are, generally, good.

Therefore, I conclude that the presented analysis routine is able to accurately measure stellar parameters of RSGs given a set of synthetic spectra extracted from model atmospheres. Compared with DKF10 results from the NGC 2100 and NGC 6822 datasets, the stellar parameters generally agree well; however, there appears to be a significant difference in the measured metallicities by $\sim$0.1 dex, which must be expanded upon in future studies.

3.7 Conclusions

In this chapter, I presented an analysis routine that uses a grid of spectra extracted from stellar model atmospheres to estimate stellar parameters using medium resolution J-band spectroscopy of RSGs.

Initially, I gave a description of stellar atmospheres focusing on their key assumptions and limitations. Having described the background, I then detailed the model stellar atmospheres used in the present study and described the corrections made to include the non-LTE effects of the strongest diagnostic lines. I then described the steps taken to estimate best-fit stellar parameters, where the χ^2-statistic was used to generate the posterior probability density function, which was then sampled using an affine-invariant ensemble sampler.

The analysis was then tested using various simulated spectra generated from the model grid (at different resolution and S/N ratios) and I demonstrated that

this routine was internally consistent. Finally, this technique was thoroughly compared with that of DKF10 on all of the datasets used within this thesis and was shown to compare well on average, with a small potential systematic of $\sim$0.1 dex in the metallicity measurements between the two analyses. This must be quantified further in future studies.

Chapter 4

Chemistry and Kinematics of NGC 2100

4.1 Opening Remarks

This chapter is based on the study which is accepted for publication in Patrick et al. (2016) and represents the first application of the analysis technique presented in Chapter 3. Although this study was conducted after that of Chapter 5, Chapters 4, 5 and 6 are ordered by their distance from the Milky Way, rather than when they were undertaken.

4.2 Introduction

Young massive clusters (YMCs[1]) are important probes of the early evolution of star clusters and have increasingly been used as tracers of star formation in galaxies (e.g. Whitmore & Schweizer, 1995; Miller et al., 1997; Zepf et al., 1999). Known to contain large populations of massive stars, YMCs are also important tracers of massive star formation, which is heavily clustered (Lada & Lada, 2003; de Wit et al., 2005; Parker & Goodwin, 2007). In addition to being the birthplace of most of the massive stars in the Local Universe ($> 200\,M_{\odot}$ stars in R136; Crowther et al., 2010), owing to the density of stars, YMCs are thought to be the

[1] A YMC is defined as having an age of < 100 Myr and a stellar mass of $> 10^4\,M_{\odot}$ (Portegies Zwart, McMillan & Gieles, 2010).

birthplace of some of the rich stellar exotica (e.g. blue stragglers, X-ray binaries and radio pulsars) found in the old population of globular clusters (GCs; Portegies Zwart, McMillan & Gieles, 2010).

Recently, the idea that GCs are simple stellar populations has been called into question based on chemical anomalies of light elements (C, N, O, Na and Al; e.g. Gratton, Carretta & Bragaglia, 2012). These anomalies are considered by most authors to be the signature of multiple stellar populations within GCs. Studying YMCs could therefore potentially help to constrain some of the proposed models for creating multiple stellar populations within GCs (e.g. Cabrera-Ziri et al., 2014).

Investigating the link between YMCs and older clusters is an important, uncertain, factor in the evolution of young clusters. As most stellar systems are thought to dissolve shortly after formation (Lada & Lada, 2003), determining how long bound systems can remain so is an important question to answer. Studying the dynamical properties of YMCs is, therefore, an important tool to evaluate the likelihood that young clusters will survive. In addition, the study of YMCs in different environments can help bridge the gap between the understanding of star formation in the Solar neighbourhood and that in the high-redshift Universe.

Gazak et al. (2013) demonstrated that, after the appearance of the first RSGs within a YMC, the overall near-IR flux from the cluster is dominated by the RSGs ($F_{J,RSG}/F_J > 0.90$). Using this result, these authors showed that the spectrum from an unresolved star cluster can be used to estimate the average properties of the RSG population of the cluster using exactly the same analysis method as for single stars. Lardo et al. (2015) demonstrated this with KMOS spectroscopy of three unresolved YMCs in NGC 4038 in the Antennae ($d = 20$ Mpc), at Solar-like metallicity, finding good agreement with previous studies based on H II region measurements. With a multi-object spectrograph operating on the European Extremely Large Telescope, this technique could be used to measure metallicities of individual RSGs at distances of > 10 Mpc and from YMCs out to potentially > 100 Mpc (Evans et al., 2011a).

NGC 2100 is a YMC in the Large Magellanic Cloud (LMC), located near the large star-forming 30 Doradus region. With an age of ~ 20 Myr (Elson, 1991; Niederhofer et al., 2015), and a photometric mass of $4.6 \times 10^4 M_\odot$ (McLaughlin & van der Marel, 2005, assuming King (1966) profiles), NGC 2100 falls within the mass and age range where the near-IR cluster light is dominated by RSGs (Gazak

et al., 2013). This is supported by the large number of RSGs identified within this cluster (see Figure 4.1).

NGC 2100 is not a cluster in isolation. It is located in one of the most actively star-forming regions within the Local Group of galaxies. At $\sim$20 Myr old, the most massive members of this star cluster will have already exploded as supernovae. This should have had a profound effect on the surrounding gas and dust, and has potentially shaped the surrounding LMC 2 supershell (see Points et al., 1999).

In this chapter I estimate stellar parameters from KMOS spectroscopy for 14 RSGs which appear to be associated with NGC 2100. Section 4.3 describes the observations and data reduction, and I detail the results in Section 4.4, focusing on radial velocities of the target stars where I derive the line-of-sight velocity dispersion, the dynamical mass of NGC 2100 and stellar parameters. The results are discussed in Section 4.5 and conclusions are presented in Section 4.6.

4.3 Observations and Data Reduction

These observations were obtained as part of the KMOS Guaranteed Time Observations (PI: Evans 095.B-0022) in March 2015. The observations consisted of 8×10 s exposures (seeing conditions $\sim$1.″0) taken with the YJ grating with sky offset exposures (S) interleaved between the object exposures (O) in an O, S, O observing pattern. In addition, a standard set of KMOS calibration frames were obtained as well as observations of HD 51506 (B5) as the telluric standard star. Figure 4.1 shows the observed RSGs overlaid on a J-band VISTA image of the surrounding region (Cioni et al., 2011).

The standard KMOS/esorex routines (SPARK; Davies, R. I. et al., 2013) were used to calibrate and reconstruct the data cubes. Telluric correction was performed using the 24-arm telluric-correction routine using the methodology described in detail by Patrick et al. (2015). Briefly, corrections are made to the standard telluric recipe to account for slight differences in wavelength calibration between the telluric and science spectra. This is implemented using an iterative cross-correlation approach. Additionally, differences in the strength of the telluric features are corrected by applying a simple scaling using the equation:

$$T_2 = (T_1 + c)/(1 + c) \tag{4.1}$$

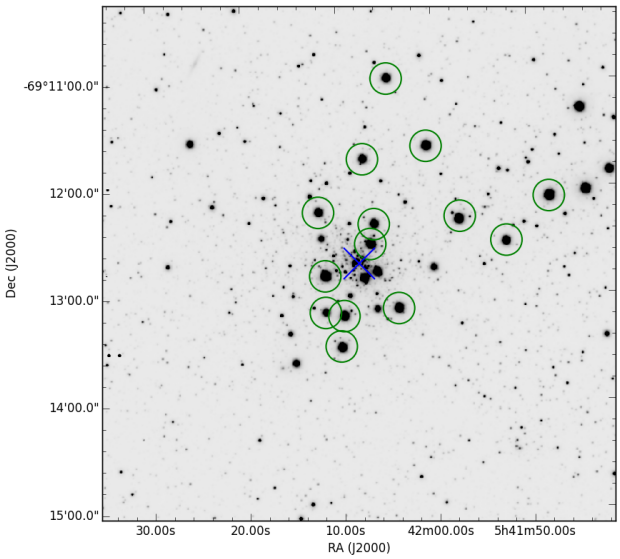

Figure 4.1 *Positions of the KMOS targets in NGC 2100 overlaid on a VISTA J-band image (Cioni et al., 2011). Green circles indicate KMOS targets. The adopted cluster centre has been marked by a blue cross.*

where T_2 is the scaled telluric-standard spectrum, T_1 is the uncorrected telluric-standard spectrum and c is the scaling parameter which is varied from $c = -0.5$ to $c = 0.5$ in increments of 0.02. The best value of c is chosen based on the overall standard deviation of the spectrum, i.e. the c value producing the smallest σ is selected. Once these corrections are accounted for, the science spectra are divided by the appropriate telluric spectrum for that particular KMOS integral field unit (IFU).

4.4 Results

4.4.1 Radial Velocities and Velocity Dispersion

Radial velocities are estimated using an iterative cross-correlation method. To ensure systematic shifts are removed, the observed spectra are first cross-correlated against a spectrum of the Earth's atmosphere, taken from the European Southern Observatory web pages[2], at a much higher spectral resolution than that of KMOS. This spectrum is then degraded to the resolution of the

[2]Retrieved from http://www.eso.org/sci/facilities/paranal/decommissioned/isaac/tools/spectroscopic_standards.html.

Table 4.1 *Observed properties of KMOS targets in NGC 2100*

ID	S/N	J^{a}	H^{a}	$K_{s}{}^{a}$	RV (km s^{-1})	Probabilities[b]		Notes[c]
						P1	P2	
J054147.86−691205.9	320	9.525	8.603	8.200	250.3 ± 4.7	92	8	D15
J054152.51−691230.8	200	10.413	9.526	9.155	249.3 ± 2.6	93	7	D16
J054157.44−691218.1	200	9.811	9.036	8.738	245.6 ± 3.5	90	10	C2
J054200.74−691137.0	260	9.900	9.017	8.683	248.8 ± 2.7	93	7	C8
J054203.90−691307.4	250	9.839	8.996	8.740	251.1 ± 2.8	92	8	B4
J054204.78−691058.8	210	10.319	9.427	9.159	256.1 ± 4.0	74	26	...
J054206.36−691220.2	200	10.371	9.480	9.159	255.7 ± 4.9	77	23	B17
J054206.77−691231.1	250	9.977	9.150	8.807	250.6 ± 3.4	92	8	A127
J054207.45−691143.8	200	10.482	9.610	9.351	252.5 ± 3.0	90	10	C12
J054209.66−691311.2	240	9.976	9.136	8.841	254.3 ± 4.1	84	16	B47
J054209.98−691328.8	250	10.021	9.150	8.823	250.2 ± 3.0	93	7	C32
J054211.56−691248.7	300	9.557	8.617	8.264	255.5 ± 4.3	78	22	B40
J054211.61−691309.2	150	10.943	10.090	9.788	256.6 ± 6.1	72	28	B46
J054212.20−691213.3	200	10.440	9.622	9.335	260.0 ± 4.8	34	66	B22

[a] Photometric data from 2MASS, with typical errors on J, H, and K_{s} of 0.024, 0.026 and 0.022 mag respectively.
[b] Probabilities $P1 = P(x|\{\mu,\sigma\}_{NGC\,2100}, \{\mu,\sigma\}_{LMC-field})$,
$P2 = P(x|\{\mu,\sigma\}_{LMC-field}, \{\mu,\sigma\}_{NGC\,2100})$
[c] Cross-identifications in final column from Robertson (1974).

observations using a simple Gaussian filter. The cross-correlation is performed within the 1.140–1.155 μm region, as a strong set of reliable telluric features dominates this region, with minimal contamination from stellar features. The shift arising from this comparison is typically 0–10 km s^{-1} and is then applied to the science spectra so that they are on a consistent wavelength solution.

Stellar radial velocities are estimated following a similar approach to the methods used by Lapenna et al. (2015) and Patrick et al. (2015). An initial radial-velocity estimate is found for each star from cross-correlation of the KMOS spectra with an appropriate model spectrum in the 1.16–1.22 μm region (selected owing to the dominance of atomic features in RSG spectra at these wavelengths). The initial estimate is improved upon via an independent cross-correlation of the observed and model spectra for seven strong absorption lines in this region.

The quoted radial velocity for each star is the mean of these estimates, where the quoted uncertainty is the standard error of the mean (i.e. $\sigma/\sqrt{n_{\rm lines}}$). Obvious outliers (with δRVs of tens of km s^{-1}) were excluded in calculating the mean estimates; such outliers arise occasionally from spurious peaks in the cross-correlation functions from noise/systematics in the spectra.

In order to sample from the posterior probability distribution for the intrinsic velocity dispersion and mean cluster velocity (given the observed radial velocity estimates and their uncertainties), EMCEE (Foreman-Mackey et al., 2013), an

implementation of the affine-invariant ensemble sampler for Markov chain Monte Carlo (MCMC) of Goodman & Weare (2010), is used. The likelihood function is given by

$$p(D|\{\sigma_{1D}, v_0\}) = \prod_i \frac{1}{\sqrt{2\pi(\sigma_{1D}^2 + \sigma_{v,i}^2)}} \exp\left(\frac{-(v_i - v_0)^2}{2(\sigma_{1D}^2 + \sigma_{v,i}^2)}\right), \tag{4.2}$$

where σ_{1D} is the intrinsic velocity dispersion of the cluster, v_0 is the mean cluster velocity, and the data consists of the set of radial velocity measurements v_i and their uncertainties $\sigma_{v,i}$. The intrinsic cluster dispersion is assumed to be Gaussian with no variations in the dispersion across the sample. The systemic radial velocity (v_0) of the sample is estimated to be $251.6 \pm 1.1\,\mathrm{km\ s^{-1}}$.

Figure 4.2 shows the stellar radial velocity estimates as a function of distance from the centre of the cluster, compared with the average radial velocity of ∼200 massive stars within the LMC from Evans et al. (2015, green dashed line). To quantify the likelihood that the measured velocities are consistent with the NGC 2100 mean cluster velocity the probability that each measured velocity is drawn from a two-component mixture of Gaussian distributions with $P(x|\{\mu,\sigma\}_{NGC\,2100}) + P(x|\{\mu,\sigma\}_{LMC-field}) = 1$ is calculated, where the *LMC-field* distribution is defined by Evans et al. (2015). This allows calculation of the ratio of the probabilities using the equation,

$$P(x|\{\mu,\sigma\}_X, \{\mu,\sigma\}_Y) = \frac{P(x|\{\mu,\sigma\}_X)}{P(x|\{\mu,\sigma\}_X) + P(x|\{\mu,\sigma\}_Y)}, \tag{4.3}$$

where x is the measured radial velocity with associated uncertainty σ_x, $P(x|\{\mu,\sigma\}_X)$ and $P(x|\{\mu,\sigma\}_Y)$ are the Gaussian distributions centred on the NGC 2100 systemic velocity or the LMC-field population as defined by Evans et al. (2015).

The probabilities $P(x|\{\mu,\sigma\}_{NGC\,2100})$ and $P(x|\{\mu,\sigma\}_{LMC-field})$, for each target are calculated using the equation,

$$P(x|\{\mu,\sigma\}_X) = \frac{1}{2(\sigma_x^2 + \sigma_X^2)} \exp\left(\frac{x - \mu_X}{2(\sigma_x^2 + \sigma_X^2)}\right), \tag{4.4}$$

where μ_X and σ_X define the Gaussian distribution of the model (i.e. NGC 2100 or LMC-field).

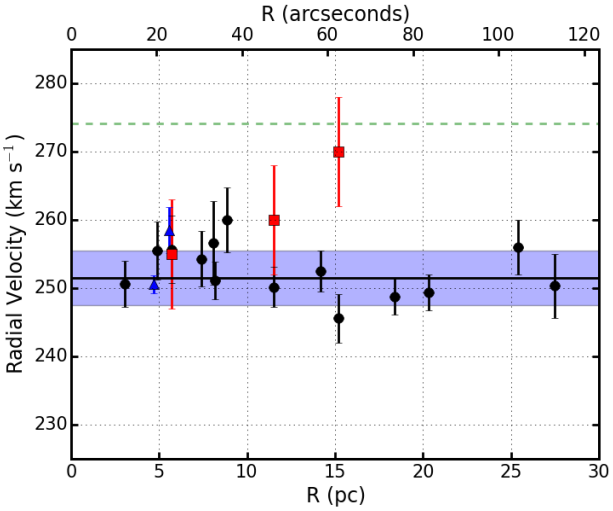

Figure 4.2 *Radial velocities of KMOS targets (black points) shown as a function of distance from the cluster centre. The green dashed line shows the Large Magellanic Cloud systemic velocity of ∼200 massive stars from (274.1 ± 16.4 km s^{-1}; Evans et al., 2015). The solid black line shows the mean cluster velocity (v_0 = 251.6 ± 1.1 km s^{-1}) and the shaded blue region shows $v_0 \pm \sigma_{1D}$. The blue triangles show estimates for two OB-type stars in NGC 2100 (Evans et al., 2015) and the red squares show previous estimates for three targets (Jasniewicz & Thevenin, 1994). The distance modulus used to produce this figure is 18.5 (Pietrzyński et al., 2013; de Grijs, Wicker & Bono, 2014).*

From this analysis one target (J054212.20−691213.3) has a measured velocity with greater probability of being drawn from the underlying distribution of massive stars rather than the distribution centred on the NGC 2100 systemic velocity. Excluding this target from the sample does not alter the estimation of v_0 or σ_{1D} significantly, therefore this target is included for further analysis.

I conclude that all targets have a velocity consistent with membership to the LMC (as opposed to Galactic objects) and that none display compelling evidence for being excluded from membership of NGC 2100.

The estimated v_0 is in reasonable agreement with previous measurements for two OB-type stars in the cluster (Evans et al., 2015) as well as the results from four RSGs in NGC 2100 (Jasniewicz & Thevenin, 1994, henceforth JT94; three of which were observed in the current study). Table 4.2 contains the details of previous radial velocity measurements within NGC 2100. I conclude that there exists no significant difference between the measurements and previous estimates within NGC 2100. This is an additional confirmation that absolute radial velocities can be precisely measured with KMOS spectra.

Table 4.2 *Literature stellar radial-velocity measurements within NGC 2100*

ID		RV (km s^{-1})		Reference	Notes
Lit.	current study	Lit.	current study		
AAΩ 30 Dor 407	—	258.5 ± 3.4	...	Evans et al. (2015)	O9.5 II
AAΩ 30 Dor 408	—	250.6 ± 1.3	...	Evans et al. (2015)	B3 Ia
R74 B17	J054206.36-691220.2	255 ± 8	255.7 ± 4.9	Jasniewicz & Thevenin (1994)	
R74 C2	J054157.44-691218.1	270 ± 8	245.6 ± 3.5	Jasniewicz & Thevenin (1994)	
R74 C32	J054209.98-691328.8	260 ± 8	250.2 ± 3.0	Jasniewicz & Thevenin (1994)	
R74 C34	—	265 ± 8	...	Jasniewicz & Thevenin (1994)	

ID and RV columns: the first value is from the literature and the second is from the current study.

As shown in Figure 4.3, the line-of-sight velocity dispersion (σ_{1D}) of NGC 2100 is unresolved given the current data. Therefore an upper limit on $\sigma_{1D} < 3.9\,\mathrm{km\ s^{-1}}$ at the 95% confidence level is adopted. Figure 4.4 demonstrates that there is no evidence for spatial variations in the measured σ_{1D} and it is noted that in each radial bin (which contain 5, 4 and 5 stars respectively), the measured dispersion is unresolved.

4.4.2 Dynamical Mass

Using σ_{1D} as an upper limit on the velocity distribution, one can calculate an upper limit on dynamical mass of the cluster using the virial equation:

$$M_{dyn} = \frac{\eta \sigma_{1D}^2 r_{\mathrm{eff}}}{G} \tag{4.5}$$

where M_{dyn} is the dynamical mass and $\eta = 6 r_{vir}/r_{\mathrm{eff}} = 9.75$ – providing the density profile of the cluster is sufficiently steep (Portegies Zwart, McMillan & Gieles, 2010) – where $r_{\mathrm{eff}} = 4.41\,\mathrm{pc}$ for NGC 2100 (McLaughlin & van der Marel, 2005). However, NGC 2100 has a relatively shallow density profile ($\gamma = 2.44 \pm 0.14$; Mackey & Gilmore, 2003) which means $\eta < 9.75$. Using $\sigma_{1D} = 3.9\,\mathrm{km\ s^{-1}}$ and equation 4.5, an upper limit on the dynamical mass of NGC 2100 is $M_{dyn} = 15.2 \times 10^4 M_\odot$. Comparing this to the photometric mass $M_{phot} = (2.3 \pm 1.0) \times 10^4 M_\odot$ (McLaughlin & van der Marel, 2005), the upper limit on the dynamical mass is larger.

As discussed by Gieles, Sana & Portegies Zwart (2010), binary motions can increase the measured velocity dispersion profile (e.g. see Hénault-Brunet et al., 2012). However, as Gieles, Sana & Portegies Zwart (2010) note, the mean lifetime for RSGs in binary systems is significantly decreased and, where mass transfer

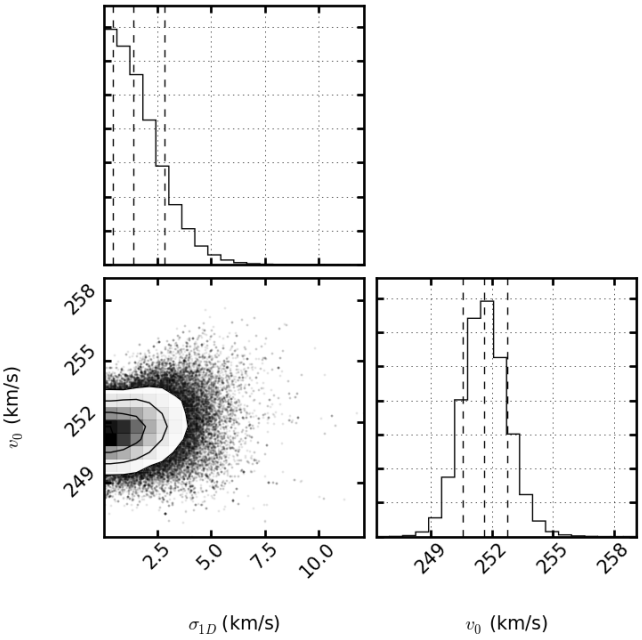

Figure 4.3 *One- and two-dimensional projections of the posterior probability distributions of the line-of-sight velocity dispersion (σ_{1D}) and systemic velocity (v_0) for NGC 2100 assuming the dispersion is Gaussian and constant over the range measured using. Using this method the velocity of NGC 2100 is $251.6 \pm 1.1\,km\ s^{-1}$. This figure also demonstrates that the velocity dispersion for the sample is unresolved and therefore an upper limit is placed on $\sigma_{1D} < 3.9\,km\ s^{-1}$ at the 95% confidence level.*

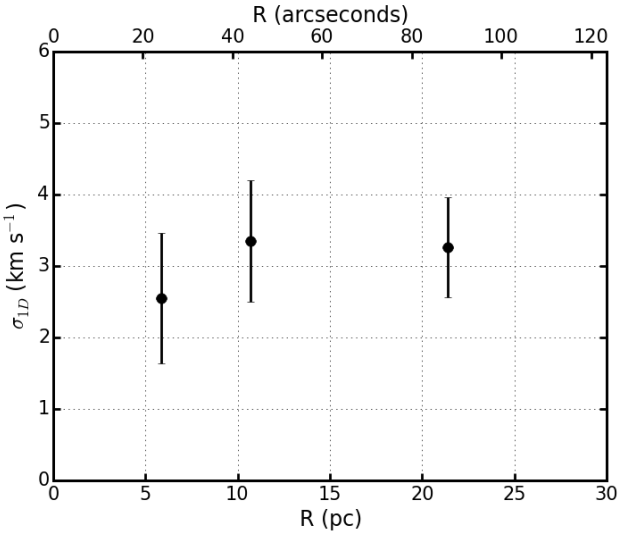

Figure 4.4 *Upper limits to the line-of-sight velocity dispersion for the NGC 2100 RSGs in three radial bins as a function of the distance from the centre of NGC 2100. This figure demonstrates that there is no evidence for spatial variations in the line-of-sight velocity dispersion. However, it is noted that in each radial bin the underlying dispersion is unresolved (see Figure 4.3).*

occurs, their number decrease dramatically (Eldridge, Izzard & Tout, 2008). Therefore it is expected that the number of RSGs in close binaries is small (Feast, 1979; Davies et al., 2009b). The fraction of RSGs in longer-period systems is less certain, but these would contribute less to the line-of-sight velocity distribution.

These arguments suggest that the estimate for the velocity dispersion in NGC 2100 is not significantly increased by binary motions as the target stars are expected to be (predominantly) single objects. As the true dispersion of the cluster appears to be unresolved (Figure 4.3), it is concluded therefore that the upper limit of the dynamical mass is consistent with the published photometric mass.

Evidence in the literature suggests that J054211.61−691309.2 is an eclipsing binary system VV Cep (Feast, 1979). However, the radial velocity of this star (256.6 ± 6.1 km s^{-1}) does not appear to be increased as a result of binary motions, with respect to the sample studied here.

4.4.3 Stellar Parameters

Stellar parameters are estimated for each target using the J-band analysis technique described initially by Davies, Kudritzki & Figer (2010) and tested rigorously by Gazak et al. (2014b) and Davies et al. (2015). These studies show that by using a narrow spectral window within the J-band one can accurately derive overall metallicities ([Z] = $\log(Z/Z_{\odot})$) to better than ± 0.15 dex at the resolution of KMOS observations with S/N $\geq$ 100. Patrick et al. (2015) built on this by demonstrating the feasibility of this technique using KMOS spectra.

The analysis uses synthetic RSG spectra, extracted from MARCS model atmospheres (Gustafsson et al., 2008), computed with corrections for non-local thermodynamic equilibrium for lines from titanium, iron, silicon and magnesium (Bergemann et al., 2012a, 2013, 2015). The parameter ranges for the grid of synthetic RSG spectra are listed in Table 4.3. The synthetic spectra are compared with observations using the χ-squared statistic and the synthetic spectra are degraded to the resolution and sampling of the observations. The diagnostic spectral features used to estimate stellar parameters have equal weighting in the analysis.

Estimated stellar parameters are listed in Table 4.4. Figure 4.5 shows the observed KMOS spectra (black) compared to their best-fitting models (red). The average metallicity for the 14 RSGs is [Z] = -0.38 ± 0.20 dex where the large scatter is a result of the contribution from (J054211.61−691309.2). Excluding this apparent outlier yields an average metallicity of [Z] = -0.43 ± 0.10 dex, which reduces the scatter and does not alter the result significantly. The model fit parameters of J054211.61−691309.2 suggest a considerably ($\times 1.7$) super-solar metallicity. This appears unlikely given its apparent membership of the LMC, and it is notable that the estimates for the surface gravity and microturbulence parameters are also outliers compared to the rest of the sample. In addition, as noted above, this star was flagged as a potential eclipsing binary by (Feast, 1979), therefore this target is excluded from the sample in further analysis.

The average metallicity in NGC 2100 estimated here is in good agreement with estimates of the cluster metallicity using isochrone fitting to the optical colour-magnitude diagram (-0.34 dex; Niederhofer et al., 2015). The only other estimate of stellar metallicity within this cluster is from JT94 who estimated metallicities using optical spectroscopy of four RSGs. These au-

Table 4.3 *Model grid used for the spectroscopic analysis.*

Model parameter	Min.	Max.	Step size
$T_{\rm eff}$ (K)	3400	4400	100
[Z] (dex)	−1.0	1.0	0.1
$\log g$ (c.g.s)	−1.00	1.00	0.25
ξ (km s^{-1})	1.0	5.0	0.2

thors found an average metallicity for NGC 2100 of [Fe/H] = -0.32 ± 0.03 dex, which is in reasonable agreement with the estimate presented here (assuming $12 + \log(\mathrm{O/H})_\odot = 8.69$ (Asplund et al., 2009)). There are three targets in common with the current study: B17, C2 and C32 (using the Robertson, 1974, nomenclature). Given the differences in the analyses (i.e. optical cf. infrared, and the different models used) the estimated parameters are in reasonable agreement for all three stars (aside from the spectroscopic gravities quoted by JT94, but with reasonable agreement with their photometric gravity estimates).

Using the same analysis technique as in this study, Davies et al. (2015) estimate metallicities for nine RSGs within the LMC, finding an average value of [Z] = -0.37 ± 0.14 dex, which agrees well with the estimated presented in this chapter. In Figure 4.6, the effective temperatures and metallicities from NGC 2100 are compared with those estimated for RSGs elsewhere in the LMC. Reasonable agreement is found in the distribution of temperatures from the two studies. A simple two-tailed Kolmogorov–Smirnov (KS) test shows that the null hypothesis of the two samples being drawn from the same distribution cannot be rejected at the 10% level ($D = 0.44$, $p = 0.18$). The range in [Z] from the LMC population is slightly larger than that of the NGC 2100 RSGs, which is expected when comparing a star cluster with an entire galaxy.

4.5 Discussion

4.5.1 Stellar Parameters

Luminosities have been estimated for the target stars from K-band photometry (see Table 4.1) using the bolometric correction from Davies, B. et al. (2013) with a small contribution from interstellar extinction using E(B−V) = 0.17 (Niederhofer et al., 2015) assuming $R_V = 3.5$ (Doran et al., 2013) and $A_K/A_V = 0.112$ (Rieke

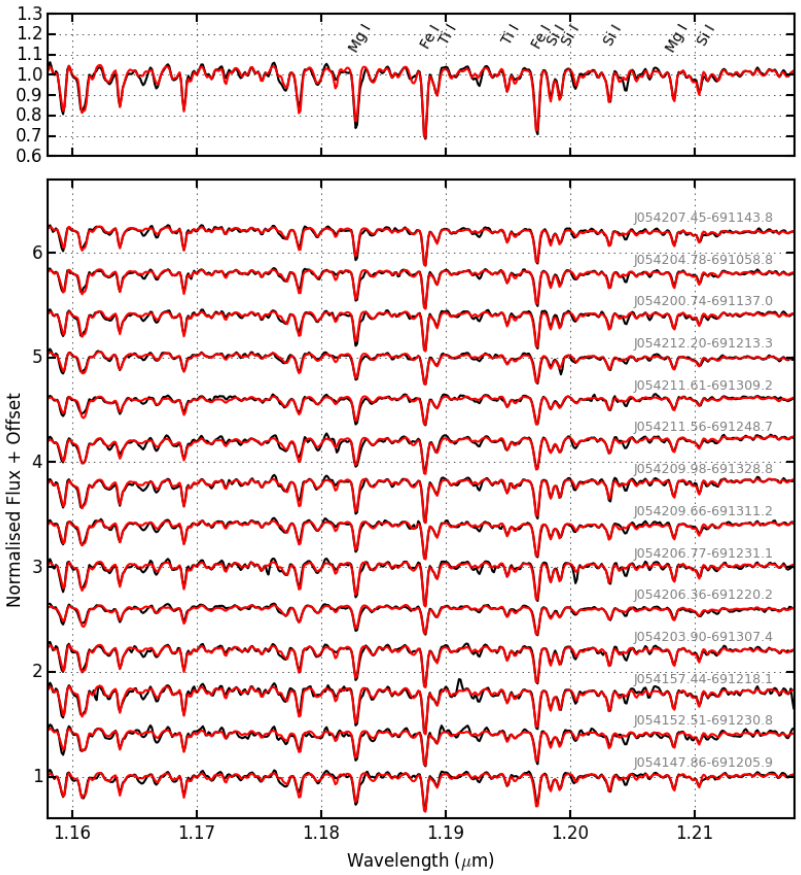

Figure 4.5 *KMOS spectra of RSGs in NGC 2100 and their associated best-fit models (black and red lines, respectively). The upper panel shows the simulated integrated-light cluster spectrum; the lower panel shows spectra for the individual RSGs. The lines used for the analysis, from left-to-right by species, are Fe I λλ1.188285, 1.197305; Mg I λλ1.182819, 1.208335; Si I λλ1.198419, 1.199157, 1.203151, 1.210353; Ti I λλ1.189289, 1.194954.*

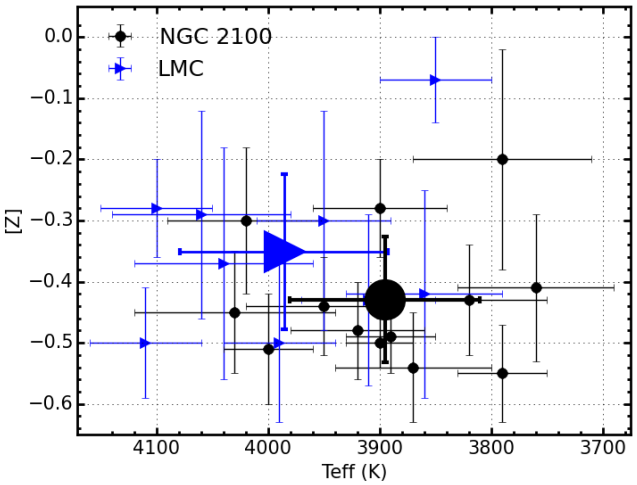

Figure 4.6 *Estimated metallicities for NGC 2100 RSGs in this study shown against effective temperature (black points). For comparison the distribution of Large Magellanic Cloud RSGs from Davies et al. (2015, blue triangles) is shown with good agreement between the means of the two samples.*

Table 4.4 *Physical parameters for the KMOS targets in NGC 2100*

Target	IFU	ξ (km s^{-1})	[Z]	log g	T_{eff} (K)	Notes[a]
J054147.86−691205.9	7	3.6 ± 0.2	-0.45 ± 0.10	0.10 ± 0.16	4030 ± 90	D15
J054152.51−691230.8	9	3.6 ± 0.2	-0.51 ± 0.09	0.43 ± 0.18	4000 ± 40	D16
J054157.44−691218.1	6	4.9 ± 0.1	-0.44 ± 0.08	0.15 ± 0.20	3950 ± 70	C2
J054200.74−691137.0	4	4.2 ± 0.2	-0.55 ± 0.08	0.23 ± 0.10	3790 ± 40	C8
J054203.90−691307.4	12	4.5 ± 0.2	-0.49 ± 0.06	0.23 ± 0.09	3890 ± 40	B4
J054204.78−691058.8	3	4.2 ± 0.2	-0.54 ± 0.09	0.46 ± 0.15	3870 ± 70	...
J054206.36−691220.2	24	2.8 ± 0.4	-0.20 ± 0.18	0.42 ± 0.18	3790 ± 80	B17
J054206.77−691231.1	10	4.9 ± 0.2	-0.50 ± 0.04	0.25 ± 0.09	3900 ± 30	A127
J054207.45−691143.8	2	4.0 ± 0.2	-0.43 ± 0.09	0.45 ± 0.17	3820 ± 70	C12
J054209.66−691311.2	14	3.8 ± 0.2	-0.41 ± 0.12	0.06 ± 0.20	3760 ± 70	B47
J054209.98−691328.8	11	4.8 ± 0.1	-0.48 ± 0.08	0.17 ± 0.22	3920 ± 60	C32
J054211.56−691248.7	20	3.8 ± 0.2	-0.28 ± 0.08	0.01 ± 0.16	3900 ± 60	B40
J054211.61−691309.2	18	2.2 ± 0.4	0.23 ± 0.23	0.65 ± 0.19	3800 ± 100	B46
J054212.20−691213.3	22	3.3 ± 0.2	-0.30 ± 0.12	0.33 ± 0.31	4020 ± 70	B22
NGC 2100 average[b]		4.0 ± 0.6	-0.43 ± 0.10	0.27 ± 0.15	3900 ± 85	
Integrated-light spectrum[c]		4.6 ± 0.3	-0.42 ± 0.14	0.37 ± 0.22	3860 ± 85	

[a] ID in final column from Robertson (1974).
[b] Averages computed excluding J054211.61−691309.2. See text for details.
[c] Simulated integrated light cluster spectrum parameters estimated excluding J054211.61−691309.2.

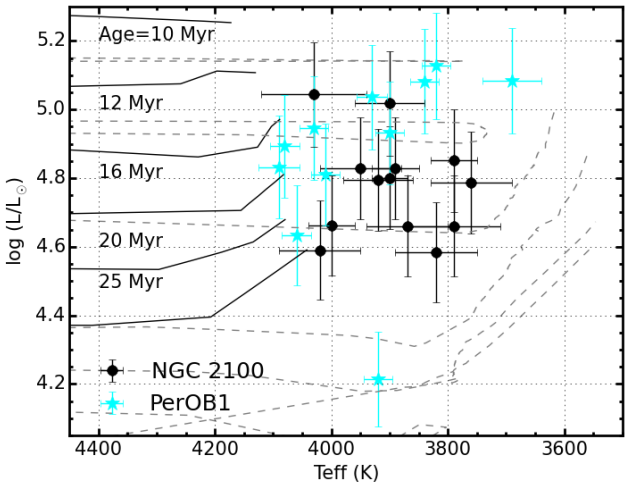

Figure 4.7 *Hertzsprung–Russell diagram for 14 RSGs in NGC 2100 (black points). Isochrones for solar (dashed grey lines; Ekström et al., 2012) and Small Magellanic Cloud (SMC) (solid black lines; Georgy et al., 2013) metal abundances, in which stellar rotation is 40% of the break-up velocity, are shown for ages of 10-32 Myr. For comparison, 11 RSGs from the Galactic young massive cluster Perseus OB-1 are overlaid with cyan stars (Gazak et al., 2014b). The best-fit isochrone to the observed data has an age of 20 ± 5 Myr for both SMC- and solar-like metallicities.*

& Lebofsky, 1985). The H–R diagram for the cluster is presented in Figure 4.7. Overlaid on this H–R diagram are SYCLIST stellar isochrones for SMC-like (solid lines; Georgy et al., 2013) and Solar-like (dashed lines; Ekström et al., 2012) models, where stellar initial rotation is 40% of break-up velocity. The Solar-like models (dashed) demonstrate that, when compared with the SMC-like models, increasing the metallicity of the sample

i decreases the average temperature of the RSGs (something which is not observed by Patrick et al., 2015, see Chapter 5),

ii induces so called 'blue loop' behaviour for the youngest models and

iii decreases the luminosity for the youngest models.

In addition, results for 11 RSGs from the Galactic star cluster Perseus OB-1 (PerOB1; Gazak et al., 2014a) are overlaid in Figure 4.7 (blue stars) for which stellar parameters were estimated using the same analysis technique as in this study. PerOB1 is an association with a similar mass and age ($2 \times 10^4\,M_\odot$ and 14 Myr respectively; Currie et al., 2010) as NGC 2100, and a comparison between

the stellar components of these two clusters using a consistent analysis technique is useful to highlight differences in stellar evolution within clusters at this range of metallicities.

From Figure 4.7, generally, the estimated temperatures are in good agreement between the two clusters. The median luminosity for the PerOB1 targets ($10^{4.93 \pm 0.15}\,L_{\odot}$) is slightly above that of NGC 2100 ($10^{4.77 \pm 0.15}\,L_{\odot}$) which could represent the slight difference in the ages of the two clusters. As PerOB1 is younger, the average mass for a RSG in the cluster will be larger than the average in NGC 2100. Therefore, I would expect to see higher luminosity RSGs in PerOB1. This is in general true and when ranked, the highest three luminosity stars reside in PerOB1. The average effective temperatures for the two data sets (NGC 2100: 3910 ± 15 K, PerOB1: 3940 ± 10 K) are in reasonable agreement, where the spread in temperatures is slightly larger for PerOB1 ($\sigma_{\rm PerOB1} = 120$ K, $\sigma_{\rm NGC\,2100} = 90$), particularly so for the highest luminosity targets within the PerOB1 sample. Again, using a simple two-tailed KS test the null hypothesis that the two samples are drawn from the same distribution cannot be rejected at the 10% level ($D = 0.30$, $p = 0.57$). Overall, by comparing these two star clusters with a similar mass, age and stellar population, I conclude that there exists no significant difference in appearance on the H–R diagram of RSGs within star clusters of different metallicities. However, it is important to note that currently there exists solely two data points with which to make this conclusion, which span a modest range of metallicities. In order to more rigorously examine this relationship, additional YMCs must be studied particularly at low-metallicity.

4.5.2 Simulated Cluster Spectrum Analysis

The individual stars in NGC 2100 can be used to simulate the analysis of a YMC in the more distant Universe, assuming that RSGs dominate the near-IR flux from such a cluster (Gazak et al., 2013). Gazak et al. (2014b) use this assumption to create a simulated integrated-light cluster spectrum for PerOB1 and show that, by analysing the combined spectrum from their 11 RSGs, the resulting parameters are consistent with the average parameters estimated using the individual stars. NGC 2100 has a similar mass and age to PerOB1 and Gazak et al. (2014b) analysed a similar number of RSGs to this study, therefore, a direct comparison between the two clusters is useful to investigate potential metallicity dependencies.

To create a simulated integrated-light cluster spectrum the individual RSG spectra are summed and weighted by their J-band luminosities. The resulting spectrum is then degraded to the lowest resolution spectrum of the sample using a simple Gaussian filter. The top panel of Figure 4.5 shows the resulting integrated-light cluster spectrum. This spectrum is then analysed in the same way described in Section 4.4.3 for a single RSG. The results of this analysis are what one would expect from KMOS observations of more distant YMCs where individual stars cannot be resolved. The estimated parameters for this spectrum are, a metallicity of -0.35 ± 0.07 dex, an effective temperature of 3960 ± 70 K, a surface gravity of 0.64 ± 0.19 dex and a microturbulent velocity of 4.6 ± 0.2 km s^{-1} which agree well with the averages of the individual RSG parameters.

4.5.3 Velocity Dispersion and Dynamical Mass

This study represents the first estimate of an upper limit to the line-of-sight velocity dispersion profile for NGC 2100. Comparing this estimate with that of other YMCs in the Local Universe is useful to ascertain if this cluster shares similar properties with other YMCs. The properties NGC 2100 are well matched by other clusters with similar masses and ages, particularly so with RSGC01, a Galactic YMC (Davies, B. et al., 2007).

Owing to the non-negligible contribution from measurement errors, the σ_{1D} adopted here is an upper limit to the true dispersion within the cluster which is likely to be significantly smaller. Using the data available, $\sigma_{1D} < 3.9$ km s^{-1}to the 95% confidence level, however, the true dispersion of the cluster is unresolved.

By extension, the dynamical mass estimated here is therefore also an upper limit to the true mass of the cluster. There are several factors that could alter the value of the dynamical mass estimate. The likely value of the η parameter is discussed in Section 4.4.2 and any change in this value will act to decrease the estimated dynamical mass.

4.6 Conclusions

Using KMOS spectra of 14 RSGs in NGC 2100 for the first time the dynamical properties of this cluster have been estimated. Radial velocities have been

estimated using KMOS, to a precision of $< 5\,\mathrm{km\ s^{-1}}$, demonstrating that this instrument can be used to study the dynamical properties of star clusters in external galaxies.

An upper limit to the average line-of-sight velocity dispersion of has been estimated to be $\sigma_{1D} = 3.9\,\mathrm{km\ s^{-1}}$, at the 95% confidence level, and no evidence is found for spatial variations. Using the average velocity dispersion within NGC 2100 allows an upper limit on the dynamical mass to be calculated (assuming virial equilibrium) as $M_{dyn} = 15.2 \times 10^4 M_{\odot}$. This measurement is consistent with the literature measurement of the photometric mass (McLaughlin & van der Marel, 2005), as the true dispersion is unresolved.

In addition to estimating the dynamical properties of NGC 2100, stellar parameters have been estimated for 14 RSGs in NGC 2100 using the J-band analysis technique (Davies, Kudritzki & Figer, 2010). The average metallicity for RSGs in NGC 2100 is $[\mathrm{Z}] = -0.43 \pm 0.10\,\mathrm{dex}$, which agrees well with previous studies within this cluster and with studies of the young stellar population of the LMC.

The H–R diagram of NGC 2100 is compared with that of PerOB1: a Galactic YMC with a similar age, mass and stellar population. Using stellar parameters estimated from RSGs using the same analysis technique as in this study, this study demonstrates that there exists no significant difference in the appearance of the H–R diagram of YMCs between these Solar- and LMC-like metallicities.

By combining the individual RSG spectra within NGC 2100, I have simulated an integrated-light cluster spectrum and proceeded to analyse this spectrum using the same techniques for that of the individual RSGs, as RSGs dominate the cluster light in the J-band (Gazak et al., 2013). The results of this technique demonstrate the potential of this analysis for integrated light spectra of more distant YMCs in low-metallicity environments. I find good agreement using the integrated-light cluster spectrum with the average results of the individual RSGs.

Chapter 5

KMOS Observations in NGC 6822

5.1 Introduction

A promising new method to directly probe chemical abundances in external galaxies is with J-band spectroscopy of red supergiant (RSG) stars. With their peak flux at $\sim$1 μm and luminosities in excess of $10^4\,L_\odot$, RSGs are extremely bright in the near-IR, making them potentially useful tracers of the chemical abundances of star-forming galaxies out to large distances. To realise this goal, Davies, Kudritzki & Figer (2010) outlined a technique to derive metallicities of RSGs at moderate spectral resolving power ($R \sim 3000$). This technique has recently been refined using observations of RSGs in the Magellanic Clouds (Davies et al., 2015) and Perseus OB-1 (Gazak et al., 2014b). Using absorption lines in the J-band from iron, silicon and titanium, one can estimate metallicity ($[\mathrm{Z}] = \log \mathrm{Z}/\mathrm{Z}_\odot$) as well as other stellar parameters (effective temperature, surface gravity and microturbulence) by fitting synthetic spectra to the observations. Owing to their intrinsic brightness, RSGs are ideal candidates for studies of extragalactic environments in the near-IR.

To make full use of the potential of RSGs for this science, multi-object spectrographs operating in the near-IR on 8-m class telescopes are essential. These instruments allow us to observe a large sample of RSGs in a given galaxy, at a wavelength where RSGs are brightest. In this context, the K-band Multi-Object Spectrograph (KMOS; Sharples et al., 2013) at the Very Large Telescope (VLT), Chile, is a powerful facility. KMOS will enable determination of stellar

abundances for RSGs out to distances of ∼10 Mpc. Further ahead, a near-IR multi-object spectrograph on a 40-m class telescope, combined with the excellent image quality from adaptive optics, will enable abundance estimates for individual stars in galaxies out to tens of Mpc, a significant volume of the local universe containing entire galaxy clusters (Evans et al., 2011a).

Here I present KMOS observations of RSGs in the dwarf irregular galaxy NGC 6822, at a distance of ∼0.46 Mpc (McConnachie, 2012, and references therein). Chemical abundances have been determined for its old stellar population (e.g. Tolstoy et al., 2001; Kirby et al., 2013), but knowledge of its recent chemical evolution and present-day abundances is somewhat limited. Observations of two A-type supergiants by Venn et al. (2001) provided a first estimate of stellar abundances, finding $\log(\mathrm{Fe/H}) + 12 = 7.01 \pm 0.22$ and $\log(\mathrm{O/H}) + 12 = 8.36 \pm 0.19$, based on line-formation calculations for these elements assuming local thermodynamic equilibrium (LTE). A detailed non-LTE study for one of these objects confirmed the results finding 6.96 ± 0.09 for iron and 8.30 ± 0.02 for oxygen (Przybilla, 2002). Compared to solar values of 7.50 and 8.69, respectively (Asplund et al., 2009), this indicates abundances that are approximately one third solar in NGC 6822. A study of oxygen abundances in H II regions (Lee, Skillman & Venn, 2006) found a value of 8.11 ± 0.1, confirming the low metallicity.

NGC 6822 is a relatively isolated Local Group galaxy, which does not seem to be associated with either M31 or the Milky Way. It appears to have a large extended stellar halo (Letarte et al., 2002; Hwang et al., 2014) as well as an extended HI disk containing tidal arms and a possible HI companion (de Blok & Walter, 2000). The HI disk is orientated perpendicular to the distribution of old halo stars and has an associated population of blue stars (de Blok & Walter, 2003; Komiyama et al., 2003). This led Demers, Battinelli & Kunkel (2006) to label the system as a "polar ring galaxy". A population of remote star clusters aligned with the elongated old stellar halo have been discovered (Hwang et al., 2011; Huxor et al., 2013). In summary, the extended structures of NGC 6822 suggest some form of recent interaction.

In addition, there is evidence for a relatively constant star-formation history within the central 5 kpc (Weisz et al., 2014) with multiple stellar populations (Battinelli, Demers & Kunkel, 2006; Sibbons et al., 2012). This includes evidence for recent star formation in the form of a known population of massive stars, as well as a number of H II regions (Venn et al., 2001; de Blok & Walter, 2006;

Hernández-Martínez et al., 2009; Levesque & Massey, 2012).

In this chapter I present near-IR KMOS spectroscopy of RSGs in NGC 6822 to investigate their chemical abundances. In Section 5.2, the details of the observations are described. Section 5.3 describes the data reduction and Section 5.4 details the derived stellar parameters and investigates the spatial distribution of the estimated metallicities in NGC 6822. A discussion of the key results is presented in Section 5.5, and Section 5.6 concludes the chapter.

5.2 Observations

5.2.1 Target Selection

Targets were selected from optical photometry (Massey et al., 2007), combined with near-IR (JHK_s) photometry (for details see Sibbons et al., 2012) from the wide-field camera (WFCAM) on the United Kingdom IR telescope (UKIRT). The two catalogues were cross-matched and only sources classified as stellar in the photometry for all filters were considered.

Our spectroscopic targets were selected principally based on their optical colours, as defined by Massey (1998) and Levesque & Massey (2012). Figure 5.1 shows cross-matched stars, with the dividing line at $(B-V) = 1.25 \times (V-R) + 0.45$. All stars redder than this line, above a given magnitude threshold and with $V-R > 0.6$, are potential RSGs.

Distinguishing between RSGs and the most luminous stars on the asymptotic giant branch (AGB) is difficult owing to their similar temperatures and overlapping luminosities. Near-IR photometry can help to delineate these populations, with RSGs located in a relatively well-defined region in the near-IR $(J-K)$ CMD, as discussed by Nikolaev & Weinberg (2000). However, there is still overlap between the populations for the faintest RSGs (brightest AGBs). The near-IR CMD from the WFCAM data is shown in Figure 5.2 and was used to further inform our target selection. Employing the updated CMD criteria from Cioni et al. (2014) – modified for the distance and reddening to NGC 6822 – all of our potential targets from the combined optical and near-IR criteria are (notionally) RSGs.

The combined selection methods yielded 58 candidate RSGs, from which 18 stars

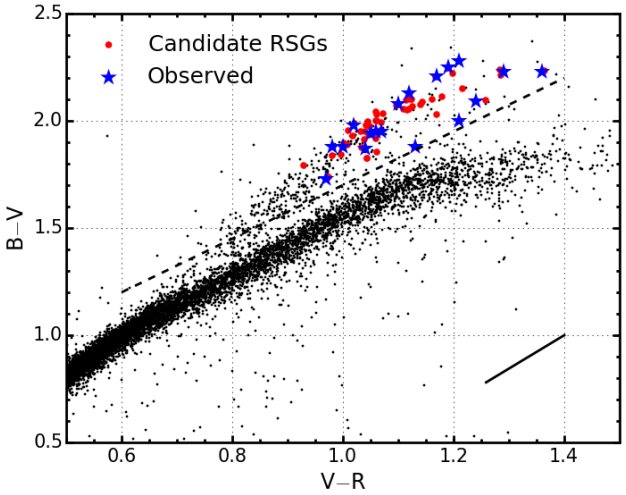

Figure 5.1 *Two-colour diagram for stars with good detections in the optical and near-IR photometry in NGC 6822. The black dashed line marks the selection criteria using optical colours, as defined by Levesque & Massey (2012). Red circles mark all stars which satisfied our selection criteria. Large blue stars denote targets observed with KMOS. The solid black line marks the foreground reddening vector for $E(B-V) = 0.22$ (Schlegel, Finkbeiner & Davis, 1998).*

were observed with KMOS, as shown in Figure 5.3. The selection of the final targets was defined by the KMOS arm allocation software KARMA (Wegner & Muschielok, 2008), where the field centre was selected to maximise the number of allocated arms, with priority given to the brightest targets. Optical spectroscopy of eight of our observed stars, confirming them as RSGs, was presented by Levesque & Massey (2012).

5.2.2 KMOS Observations

The observations were obtained as part of the KMOS Science Verification program on 30 June 2013 (PI: Evans, 60.A-9452(A)), with a total exposure time of 2400 s (comprising 8×300 s detector integrations). KMOS has 24 deployable integral-field units (IFUs) each of which covers an area of $2\farcs8 \times 2\farcs8$ within a $7\farcs2$ field-of-view. The 24 IFUs are split into three groups of eight, with the light from each group relayed to different spectrographs. KMOS is described in more detail in Chapter 2.

Offset sky frames ($0\farcs5$ to the east) were interleaved between the science observations in an object (O), sky (S) sequence of: O, S, O, O. This observing

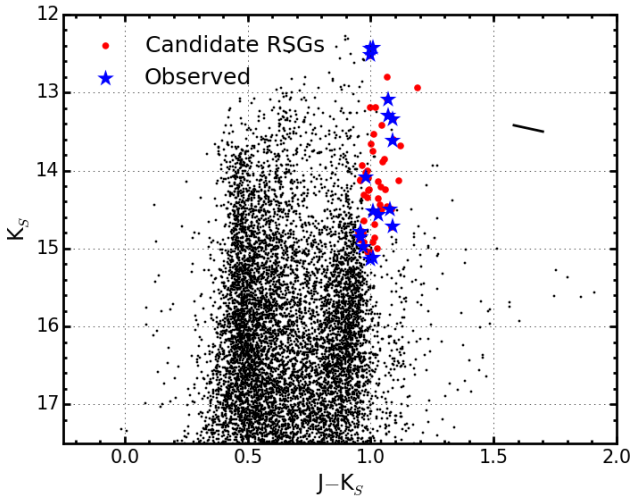

Figure 5.2 *Near-IR colour-magnitude diagram (CMD) for stars classified as stellar sources in the optical and near-IR catalogues, plotted using the same symbols as Figure 5.1. This CMD is used to supplement the optical selection. The solid black line marks the foreground reddening vector for $E(B-V) = 0.22$ (Schlegel, Finkbeiner & Davis, 1998).*

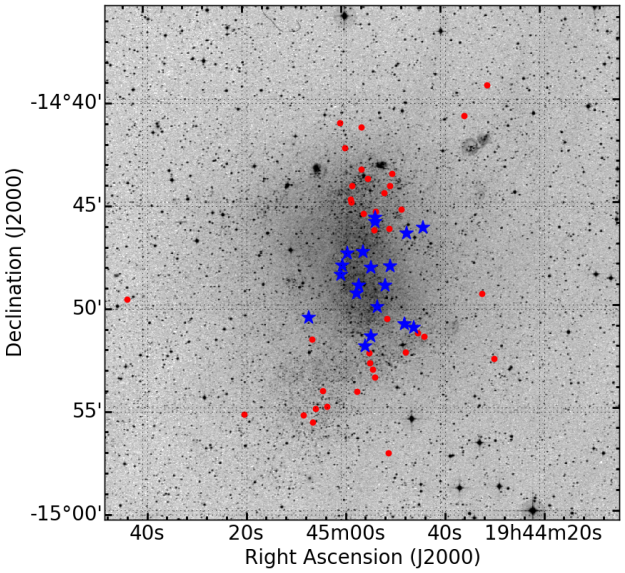

Figure 5.3 *Spatial extent of the KMOS targets over a Digital Sky Survey (DSS) image of NGC 6822. Blue stars indicate the locations of the observed red supergiant stars. Red filled circles indicate the positions of red supergiant candidates selected using out photometric criteria (see Section 5.2.1).*

Table 5.1 *Measured velocity resolution and resolving power across each detector*

Det.	IFUs	Ne λ1.17700 μm		Ar λ1.21430 μm	
		FWHM [km s^{-1}]	R	FWHM [km s^{-1}]	R
1	1-8	88.04 ± 2.67	$3\,408 \pm 103$	85.45 ± 2.67	$3\,511 \pm 110$
2	9-16	82.83 ± 2.48	$3\,622 \pm 108$	80.30 ± 3.05	$3\,736 \pm 142$
3	17-24	103.23 ± 2.73	$2\,906 \pm 77$	101.25 ± 2.99	$2\,963 \pm 87$

sequence was chosen over a more standard O S, O sequence to increase time spent on science objects. The observations were performed with the YJ grating (giving coverage from 1.02 to 1.36 μm); estimates of the mean delivered resolving power for each spectrograph (obtained from the KMOS/esorex pipeline for two arc lines) are listed in Table 5.1.

In addition to the science observations, a standard set of KMOS calibration frames were obtained consisting of dark, flat and arc-lamp calibrations (with flats and arcs taken at six different rotator angles). A telluric standard star was observed with the arms configured in the science positions, i.e. using the *KMOS_spec_cal_stdstarscipatt* template in which the standard star is observed sequentially through all IFUs. The observed standard was HIP97618, with a spectral type of B6 III (Houk & Smith-Moore, 1988).

A summary of the observed targets is given in Table 5.2. A signal-to-noise (S/N) ratio of > 100 per three pixel resolution element is required for satisfactory results from this analysis method (see Gazak et al., 2014b). We estimated the S/N ratio of the spectra by comparing the counts in the brightest spatial pixels (within the 1.15-1.22μm region) of each source with the counts in equivalent spatial pixels in the corresponding sky exposures (between the sky lines). The S/N estimated is knowingly an underestimate of the true S/N achieved.

5.3 Data Reduction

The observations were reduced using the recipes provided by the Software Package for Astronomical Reduction with KMOS (SPARK; Davies, R. I. et al., 2013). The standard KMOS/esorex routines were used to calibrate and reconstruct the science and standard-star data cubes as outlined by Davies, R. I. et al. (2013). Sky subtraction was performed using the standard KMOS recipes and telluric correction was performed using two different strategies. Throughout the following

Table 5.2 *Summary of VLT-KMOS targets in NGC 6822.*

ID	S/N	α (J2000)	δ (J2000)	B	V	R	J	H	K_s	RV (km s^{-1})	Notes
NGC6822-RSG01	223	19:44:43.81	−14:46:10.7	20.83	18.59	17.23	14.16	13.37	13.09	-63.8 ± 3.2	Sample
NGC6822-RSG02	120	19:44:45.98	−14:51:02.4	20.91	18.96	17.89	15.53	14.72	14.52	-60.6 ± 5.5	Sample
NGC6822-RSG03	94	19:44:47.13	−14:46:27.1	21.30	19.41	18.41	16.13	15.35	15.12	-69.8 ± 6.5	
NGC6822-RSG04	211	19:44:47.81	−14:50:52.5	20.74	18.51	17.22	14.37	13.58	13.30	-65.5 ± 4.4	LM12 (M1), Sample
NGC6822-RSG05	104	19:44:50.54	−14:48:01.6	20.83	18.95	17.97	15.75	14.98	14.79	-74.8 ± 5.0	
NGC6822-RSG06	105	19:44:51.64	−14:48:58.0	21.33	19.45	18.32	15.81	14.95	14.72	-65.3 ± 6.0	
NGC6822-RSG07	145	19:44:53.46	−14:45:52.6	20.36	18.43	17.38	15.06	14.30	14.08	-53.8 ± 5.1	LM12 (M4.5), Sample
NGC6822-RSG08	103	19:44:53.46	−14:45:40.1	20.88	19.14	18.17	15.95	15.16	14.98	-51.6 ± 4.1	LM12 (K5), Sample
NGC6822-RSG09	201	19:44:54.46	−14:48:06.2	20.56	18.56	17.35	14.43	13.67	13.34	-47.4 ± 2.1	LM12 (M1), Sample
NGC6822-RSG10	302	19:44:54.54	−14:51:27.1	19.29	17.05	15.86	13.43	12.66	12.42	-75.7 ± 3.5	LM12 (M0), Sample
NGC6822-RSG11	327	19:44:55.70	−14:51:55.4	19.11	16.91	15.74	13.43	12.70	12.43	-59.3 ± 4.0	LM12 (M0), Sample
NGC6822-RSG12	100	19:44:55.93	−14:47:19.6	21.43	19.56	18.52	16.14	15.33	15.14	-39.2 ± 4.6	LM12 (K5)
NGC6822-RSG13	106	19:44:56.86	−14:48:58.5	21.05	19.06	18.04	15.81	15.05	14.85	-55.7 ± 7.4	
NGC6822-RSG14	284	19:44:57.31	−14:49:20.2	19.69	17.41	16.20	13.52	12.76	12.52	-84.2 ± 1.9	LM12 (M1), Sample
NGC6822-RSG15	124	19:44:59.14	−14:47:23.9	21.30	19.17	18.05	15.58	14.74	14.50	-86.9 ± 6.6	
NGC6822-RSG16	107	19:45:00.24	−14:47:58.9	21.27	19.20	18.10	15.60	14.80	14.57	-67.7 ± 3.1	
NGC6822-RSG17	167	19:45:00.53	−14:48:26.5	20.84	18.75	17.51	14.70	13.86	13.61	-64.8 ± 4.2	Sample
NGC6822-RSG18	104	19:45:06.98	−14:50:31.1	21.06	19.12	18.06	15.74	14.94	14.78	-33.8 ± 11.7	Sample

Optical data from Massey et al. (2007), with typical photometric uncertainty 0.016, 0.006, 0.010 in B, V and R bands respectively. Near-IR data from the UKIRT survey (see Sibbons et al., 2012, for details), with typical errors 0.015, 0.010, 0.012, in J, H and K bands respectively. Targets observed by Levesque & Massey (2012) are indicated by 'LM12' in the final column (with their spectral classifications in parentheses). Targets used for abundance analysis are indicated by the comment 'Sample'.

analysis all spectra have been extracted from their respective data cubes using a consistent method (i.e. the optimal extractions within the pipeline).

5.3.1 KMOS/esorex pipeline

The KMOS/esorex pipeline performs the initial calibrations by using a set of dark, flat and arc-lamp calibrations. These calibrations are all performed on raw KMOS images which contain 14×14 spectra from each IFU from the three spectrographs. The flat-field calibrations allow one to trace the spatial coordinates of each spectrum on the raw images. This information is then combined with the wavelength calibration information, obtained from the arc-lamp calibrations, to give a 14×14×2056 3-D spectrum for each IFU across the detector. A snapshot of the 14×14 spatial pixels is shown in Figure 5.4. When reducing multiple exposures of a single object, this cube is then combined to produce the final data cube.

There are many routines with which to extract spectra from this final data cube. The simplest way to do this is to take the single brightest spectral pixel within the cube and extract a spectrum from that. However, higher signal-to-noise can be achieved by extracting the spectrum from a circular pixel mask centred on the brightest pixel, where each pixel is weighted by the integrated flux in that pixel. However, within each IFU, the resolution of the spectrum varies between spatial pixels. Therefore, in order to combine the spectra more precisely, one must first standardise the resolution across the IFU before combining (Gazak et al., 2015).

5.3.2 Sky Subtraction

Sky subtraction is performed within the pipeline before IFU reconstruction where the science frame is matched with its nearest in time sky frame. Initial inspection of the extracted stellar spectra revealed minor residuals from the sky subtraction process. Reducing these cases with the 'sky_tweak' option within the KMOS/esorex reduction pipeline was ineffective to improve the subtraction of these features. Any residual sky features could potentially influence our results by perturbing the continuum placement within the model fits, which is an important aspect of the fitting process (see Gazak et al., 2014b; Davies et al., 2015, for more discussion). Thus, pending a more rigorous treatment of the data (e.g. to take

into account the changing spectral resolution across the array), we exclude objects showing sky residuals from our analysis. Of the 18 observed targets, 11 were used to derive stellar parameters (as indicated in Table 5.2).

In-house Sky Subtraction

An alternative method of sky subtraction would to to subtract the sky from spatial pixels within the object IFU. This is possible as within each IFU the target does not extend over the entire set of spatial pixels as Figure 5.4 demonstrates. Using a collection of these spatial pixels which contain little or no object flux can be a potential method for sky subtraction. Clearly this method has large potential benefits with respect to observing efficiency as less sky exposures would be needed for a given observing run. Theoretically, the sky subtraction from a region which is nearer in space to the object in question is beneficial in two different ways:

i The sky being subtracted more closely represents the sky background which the object is contaminated with. For comparison, during the sky exposures the telescope is offset by $\sim 10\farcm0$, therefore, this sky exposure samples an intrinsically different atmospheric column when compared to the science exposure. Even though the differences in the sky lines on this spatial scale is small, as the signal originating from the sky is roughly an order of magnitude larger than that of our object, a small sky residual could affect the shape and/or strength of a genuine stellar feature.

ii The region of the host galaxy which the target object occupies will often contain contaminating flux. By sampling a region of space closer to the position of the target object, the underlying galaxy flux will be more accurately subtracted.

However, an inherent issue with this method of sky subtraction is that one may well remove some of the object flux in this process. Additionally, (as mentioned in 5.3.1) there is know to exist a slight difference in resolution over the spatial extent of the IFU which could make comparisons between spatial pixels complicated. By standardising the resolution across the IFU one can potentially obtain a more reliable sky subtraction at the expense of the resolution of the spectrum.

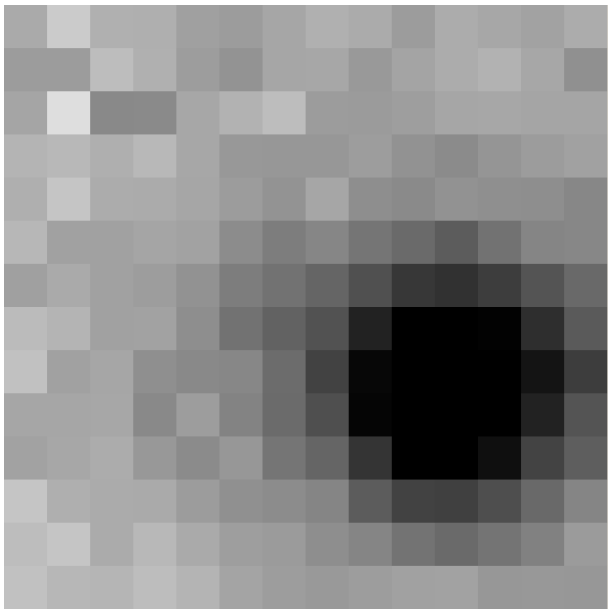

Figure 5.4 *Snapshot of a reconstructed KMOS integral field unit (IFU) (at $\lambda = 1.16\,\mu m$) containing the science target NGC6822-RSG17. Darker shades indicate higher flux. This image serves to demonstrate that the target objects do not entirely fill the KMOS IFU. This therefore, presents the possibility for using several pixels which do not contain flux from the object in the sky subtraction process.*

5.3.3 Telluric Correction

One of the most important stages within the data reduction process for spectroscopic observations from ground-based observatories concerned with measuring absorption, rather than emission, features is the correction for the effects of the Earth's atmosphere. As starlight passes through the atmosphere it is absorbed and re-emitted by various different molecules. These strong molecular features contaminate and blend genuine stellar features. In order to recover the stellar features a spectrum is derived which contains only the atmospheric absorption features. This spectrum is then used to correct the science spectrum.

Typically, one generates a telluric spectrum by observing an additional star of known spectral type. If the stellar features are well characterised for this spectral type, any additional features are assumed to be owing to the Earth's atmosphere. The spectral type is usually chosen to minimize the number of stellar features present in the region of interest. In the J-band an A0V star has few lines of note and is therefore a good choice of telluric standard star in this regime. This method of telluric correction is robust and well tested and is the preferred method for many different studies. However, it does have some fairly fundamental

limitations which include the fact that it is impossible to sample precisely the same atmospheric column in both the science and telluric observations, as well as the additional time it takes to observe a standard star.

Alternative methods to derive a telluric spectrum using atmospheric modelling have, to date, been used reasonably sparsely. However, recently such a tool has been developed and tested on some VLT instruments. The package is briefly explained in section 5.3.6.

5.3.4 Three-arm vs 24 arm Telluric Correction

The default template for telluric observations with KMOS is to observe a standard star in one IFU in each of the three spectrographs. However, there is an alternative template which allows users to observe a standard star in each of the 24 IFUs. This strategy should provide an optimum telluric correction for the KMOS IFUs but reduces observing efficiency.

A comparison between the two methods in the H-band was given by Davies, R. I. et al. (2013), who concluded that using the more efficient three-arm method was suitable for most science purposes. However, an equivalent analysis in the YJ-band was not available. To determine if the more rigorous telluric approach is required for our analysis, we observed a telluric standard star (HIP97618) in each of the 24 IFUs. This gave us the data to investigate both telluric correction methods and to directly compare the results.

We first compared the standard-star spectrum in each IFU with that used by the pipeline routines for the three-arm template in each of the spectrographs. Figure 5.5 shows the differences between the standard-star spectra across the IFUs, where the differences in the YJ-band are comparable to those in the H-band (cf. Fig.7 from Davies, R. I. et al., 2013). The qualitative agreement between the IFUs in our region of interest (1.16–1.22μm) is generally very good.

To quantify the difference the two telluric methods would make to our analysis, we performed the steps described in Section 5.3.5 for both templates. We then used the two sets of reduced science data (reduced with both methods of the telluric correction) to compute stellar parameters for our targets. The results of this comparison are detailed in Section 5.4.1.

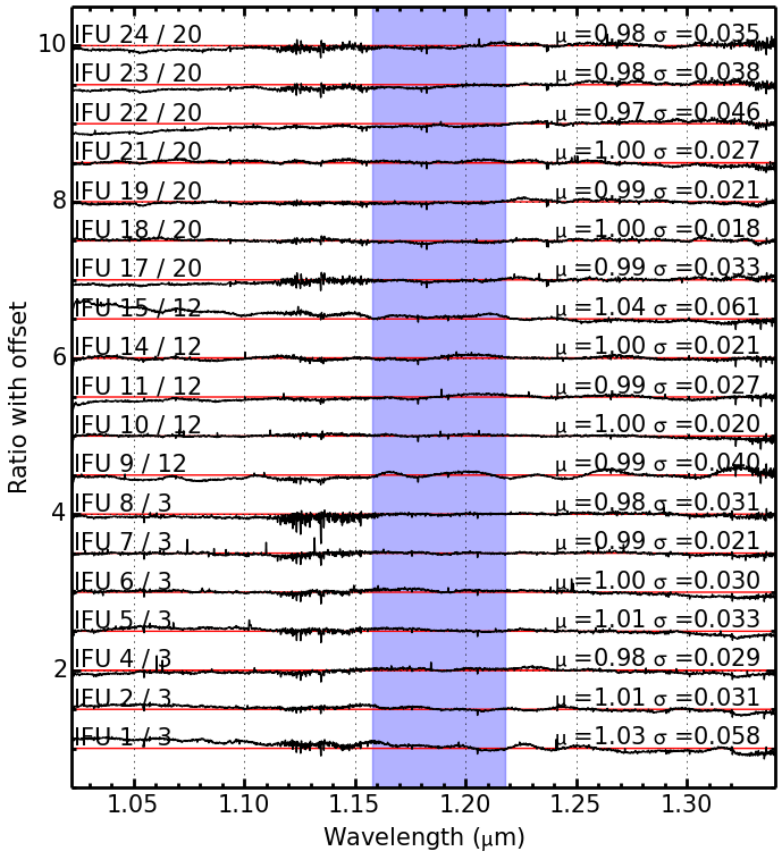

Figure 5.5 *Comparison of J-band spectra of the same standard star in each IFU. The ratio of each spectrum compared to that from the IFU used in the three-arm telluric method is shown, with their respective mean and standard deviation (μ and σ). Red lines indicate $\mu = 1.0$, $\sigma = 0.0$ for each ratio. The blue shaded area signifies the region used in our analysis, within which, the discrepancies between the IFUs are generally small. This is reflected in the standard deviation values when only considering this region. (IFUs 13 and 16 are omitted as no data were taken with these IFUs.)*

5.3.5 Telluric Correction Implementation

To improve the accuracy of the telluric correction, for both methods mentioned above, we implemented additional recipes beyond those of the KMOS/esorex pipeline. These recipes were employed to account for two effects which could potentially degrade the quality of the telluric correction. The first corrects for any potential shift in wavelength between each science spectrum and its associated telluric standard. The most effective way to implement this is to cross-correlate each pair of science and telluric-standard spectra. Any shift between the two is then applied to the telluric standard using a cubic-spline interpolation routine.

The second correction applied is a simple spectral scaling algorithm. This routine corrects for differences in line intensity of the most prominent features common to both the telluric and science spectra. To find the optimal scaling parameter the following formula is used,

$$T_2 = (T_1 + c)/(1 + c), \tag{5.1}$$

where T_2 is the corrected telluric-standard spectrum, T_1 is the initial telluric standard spectrum and c is the scaling parameter.

To determine the required scaling, telluric spectra are computed for $-0.5 < c < 0.5$, in increments of 0.02 (where a perfect value, i.e. no difference in line strength, would be $c = 0$). Each telluric spectrum is used to correct the science data and the standard deviation of the counts across the spectral region is computed for each corrected spectrum. The minimum value of the standard-deviation matrix defines the optimum scaling. For this algorithm, only the region of interest for our analysis is considered (i.e. 1.16–1.22 μm).

The final set of telluric-standard spectra from the KMOS/esorex reductions were modified using these additional routines and were then used to correct the science observations for the effects of the Earth's atmosphere.

5.3.6 MOLECFIT

As an alternative to observing telluric standard stars, a new telluric correction package, MOLECFIT, allows one to calculate a telluric spectrum based on

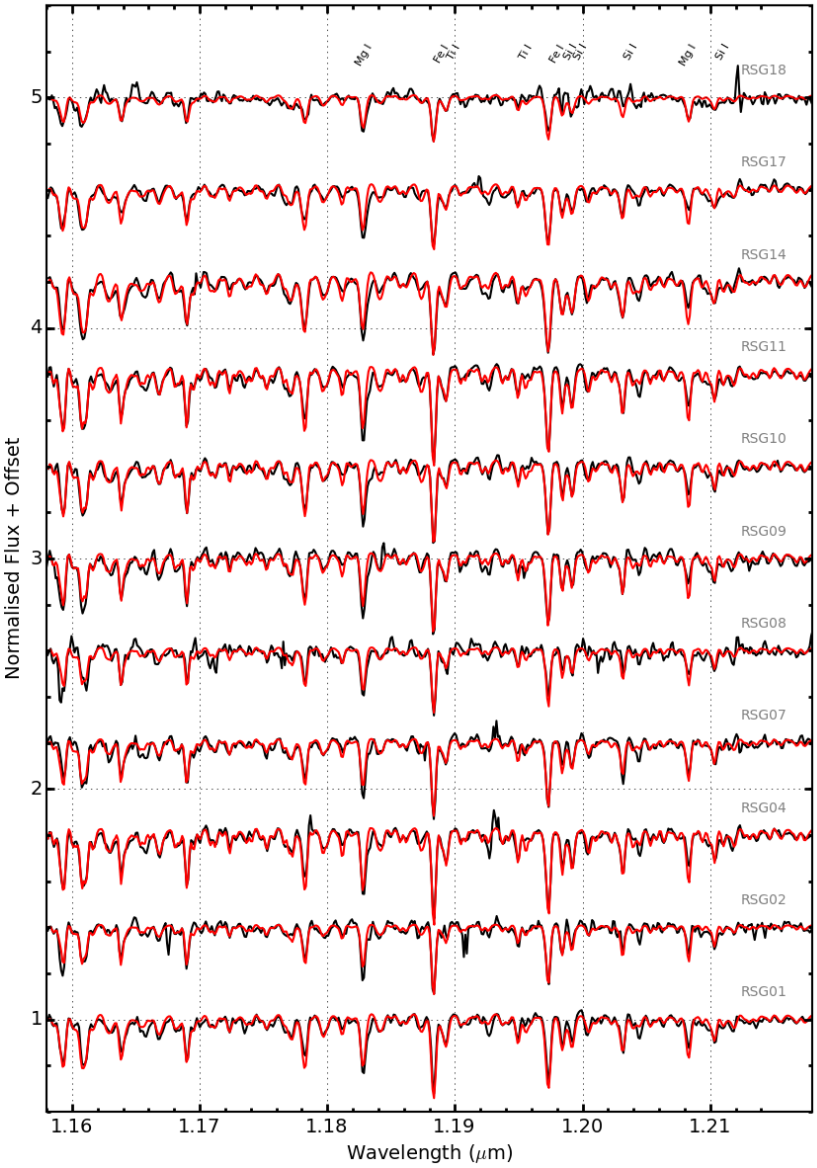

Figure 5.6 *KMOS spectra of the NGC 6822 RSGs and their associated best-fit model spectra (black and red lines, respectively). The lines used for the analysis from left-to-right by species are: Fe I λλ1.188285, 1.197305, Si I λλ1.198419, 1.199157, 1.203151, 1.210353, Ti I λλ1.189289, 1.194954. The two strong Mg I lines are also labelled, but are not used in the fits (see Section 5.4).*

Table 5.3 *Cross-correlation shift values and rescaling (c) values.*

Name	24 AT		3 AT	
	Shift	c	Shift	c
NGC6822-RSG01	0.143	0.112	0.051	0.130
NGC6822-RSG02	0.135	0.140	0.184	0.216
NGC6822-RSG03	0.115	0.104	0.036	0.112
NGC6822-RSG04	0.133	0.122	0.133	0.122
NGC6822-RSG05	0.054	0.198	-0.017	0.206
NGC6822-RSG06	0.127	0.224	0.163	0.226
NGC6822-RSG07	-0.048	0.148	0.052	0.092
NGC6822-RSG08	0.062	0.180	0.062	0.180
NGC6822-RSG09	0.077	0.060	0.012	0.090
NGC6822-RSG10	-0.014	0.102	0.150	0.134
NGC6822-RSG11	0.067	0.134	0.060	0.110
NGC6822-RSG12	0.007	0.228	-0.019	0.182
NGC6822-RSG13	-0.329	0.290	-0.310	0.342
NGC6822-RSG14	-0.464	0.138	-0.021	0.258
NGC6822-RSG15	-0.324	0.206	-0.585	0.250
NGC6822-RSG16	-0.230	0.196	-0.207	0.244
NGC6822-RSG17	-0.192	0.160	-0.192	0.160
NGC6822-RSG18	-0.521	0.366	-0.458	0.364

atmospheric modelling. Briefly, the software uses a reference atmospheric profile to estimate the true profile for the time and location of the science observation. This model is then used to create a telluric spectrum which can be used to correct the observations.

This software has been shown to work well, on a variety of VLT instruments (Smette et al., 2015) and has been rigorously tested using X-shooter spectra (Kausch et al., 2015). However, the package has yet to be tested thoroughly on lower-resolution observations such as those from KMOS. Our first tests appear encouraging, however, pending further characterisation of the KMOS data cubes (e.g., small variations in spectral resolving power leading to sky residuals, see Section 5.3.2), I will investigate the potential of the MOLECFIT package with KMOS in the future.

5.3.7 Stellar Radial Velocities

Radial velocities for each target are listed in Table 5.2. The method used here to measure radial velocity values is consistent with that presented in Chapter 4. Briefly, radial velocities are calculated using an iterative cross-correlation method. Initially, the accuracy of the wavelength solution provided by the data reduction pipeline is checked against a spectrum of the Earth's telluric features. Any offset is accounted for and the science spectrum is now assumed to be at "rest" wavelength.

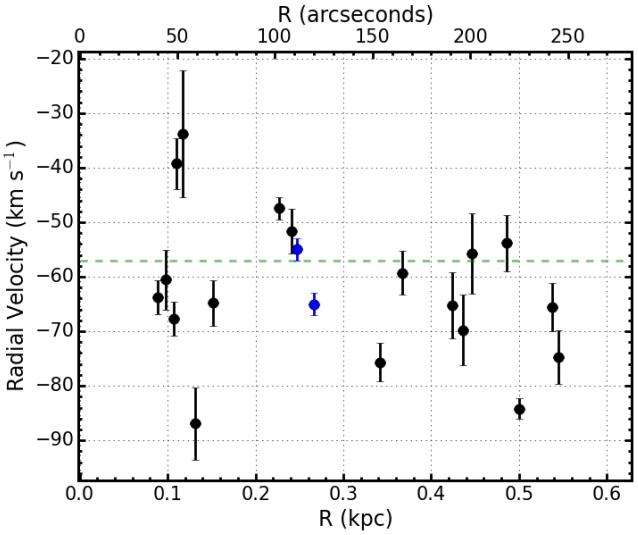

Figure 5.7 *Radial velocities of targets shown against their distance from the galaxy centre. The average radial velocity for the sample is -62 ± 13 km s^{-1}. The green dashed line indicates H I systemic velocity (-57 ± 2 km s^{-1}; Koribalski et al., 2004). The radial velocities of two A-type supergiants from Venn et al. (2001) are shown in blue.*

Once the science spectra are at "rest" wavelength, the spectra are then cross-correlated again an appropriate synthetic RSG model using a large region where stellar features are known to dominate (1.16–1.22 μm). This initial guess is then improved on by selecting seven of the strongest spectral lines in this region and a radial velocity is calculated for each of these lines. The final radial velocity is the mean of these seven strong lines where the error on the measurement is the standard deviation of the measurements normalised by the number of measurements (i.e. $\sigma/\sqrt{n_{\text{lines}}}$). This method is preferred from simply using the large 1.16–1.22 μm region as in individual lines noise features from, for example, inaccurate telluric correction or sky subtraction are more easily identified. In addition, using several cross-correlation regions allows one to analyse the intrinsic dispersion of this technique.

Radial velocities estimates are shown as a function of distance to the centre of NGC 6822 in Figure 5.7. The average radial velocity for our targets is -62 ± 13 km s^{-1}, in good agreement with the systemic radial velocity of the H I disk (-57 ± 2 km s^{-1}; Koribalski et al., 2004). Our radial velocities also agree with estimates for the two A-type supergiants from Venn et al. (2001). This result confirms that our candidates are NGC 6822 members.

Table 5.4 *Model grid used for analysis*

Model Parameter	Min.	Max.	Step size
$T_{\rm eff}$ (K)	3400	4000	100
	4000	4400	200
[Z] (dex)	−1.50	1.00	0.25
$\log g$ (cgs)	−1.0	1.0	0.5
ξ (km s^{-1})	1.0	6.0	1.0

5.4 Results

Stellar parameters (metallicity, effective temperature, surface gravity and microturbulence) have been derived using the *J*-band analysis technique described by Davies, Kudritzki & Figer (2010) and demonstrated by Gazak et al. (2014b) and Davies et al. (2015). To estimate physical parameters this technique uses a grid of synthetic spectra to fit observational data, in which the models are degraded to the resolution of the observed spectra (Table 5.1). Model atmospheres were generated using the MARCS code (Gustafsson et al., 2008) where the range of parameters are defined in Table 5.4. The precision of the models is increased by including departures from LTE in some of the strongest Fe, Ti and Si atomic lines (Bergemann et al., 2012a, 2013). The two strong magnesium lines in our diagnostic spectral region are initially excluded from the analysis as these lines are known to be affected strongly by non-LTE effects (see Figure 5.6, where the two Mg I lines are systematically under- and over-estimated, respectively). This is discussed further in Section 5.4.2.

5.4.1 Telluric Comparison

We used these Science Verification data to determine which of the two telluric standard methods (three-arm or 24-arm) is most appropriate for our analysis. Table 5.5 details the stellar parameters estimated for each target using both telluric methods and these parameters are compared in Figure 5.8. The mean difference in the parameters between the two methods is $<\Delta\xi> = -0.1 \pm 0.1$, Δ[Z] $= 0.04 \pm 0.07$, $<\Delta \log g> = -0.06 \pm 0.12$ and $<\Delta T_{\rm eff}> = -14 \pm 42$. In addition, linear fits to the distributions in Figure 5.8, show that there exists no significant relationship between the difference of the two data sets. Therefore, for our analysis, there appears to be no significant difference between the stellar parameters estimated using the two telluric approaches.

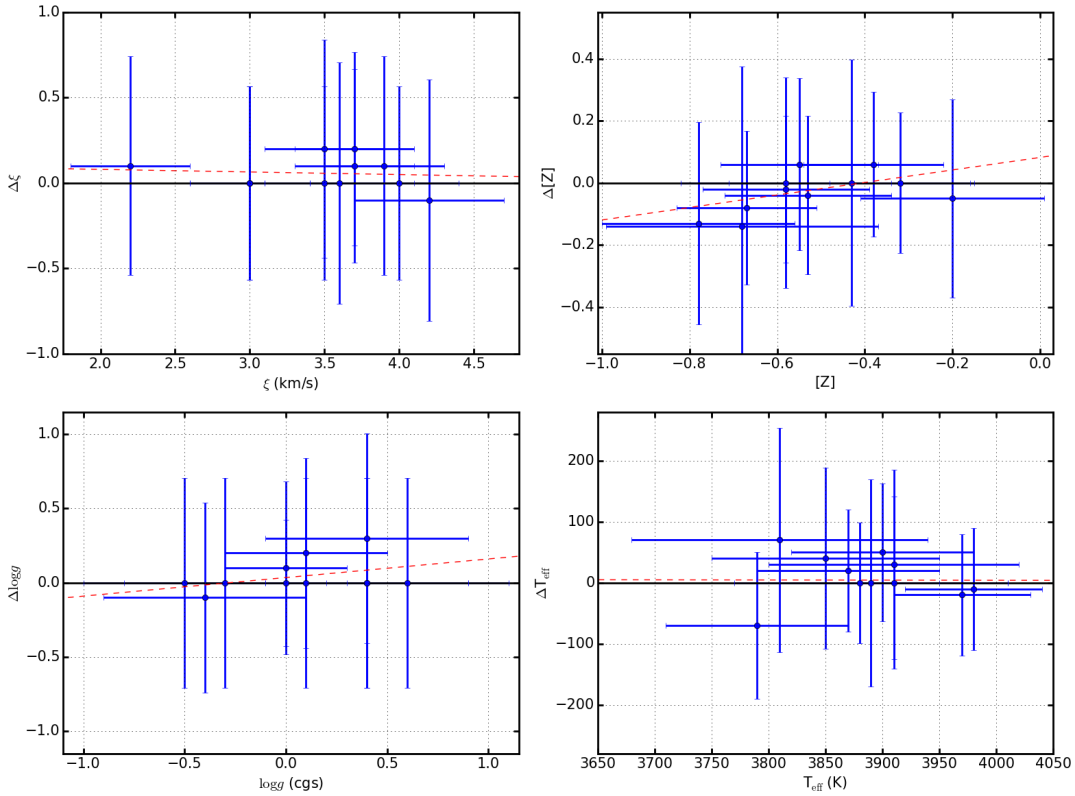

Figure 5.8 *Comparison of the model parameters using the two different telluric methods. In each panel, the x-axis represents stellar parameters estimated using the 24-arm telluric method and the y-axis represents the difference between the 24-arm and three-arm parameters (i.e.* $\Delta X = output_{24-\mathrm{arm}} - output_{3-\mathrm{arm}}$*). Top left: Microturbulence* (ξ)*, mean difference* $< \Delta\xi > = 0.1 \pm 0.1$*. Top right: metallicity* ([Z])*, mean difference* $< \Delta[Z] > = -0.04 \pm 0.07$*. Bottom left: surface gravity* ($\log g$)*, mean difference* $< \Delta \log g > = 0.06 \pm 0.12$*. Bottom right: effective temperature* (T_{eff})*, mean difference* $< \Delta T_{\mathrm{eff}}$¿ $= 14 \pm 42$*. Red dashed lines indicates linear best fits to the data.*

Table 5.5 *Fit parameters for reductions using the two different telluric methods*

Target	IFU	24 Arm Telluric				3 Arm Telluric			
		ξ (km s^{-1})	[Z]	$\log g$	$T_{\rm eff}$(K)	ξ (km s^{-1})	[Z]	$\log g$	$T_{\rm eff}$(K)
NGC6822-RSG01	6	3.5 ± 0.4	-0.55 ± 0.18	-0.0 ± 0.3	3790 ± 80	3.5 ± 0.4	-0.61 ± 0.21	-0.1 ± 0.5	3860 ± 90
NGC6822-RSG02	11	3.5 ± 0.4	-0.78 ± 0.22	0.4 ± 0.5	3850 ± 100	3.3 ± 0.5	-0.65 ± 0.24	0.4 ± 0.5	3810 ± 110
NGC6822-RSG04	12	4.0 ± 0.4	-0.32 ± 0.16	0.0 ± 0.3	3880 ± 70	4.0 ± 0.4	-0.32 ± 0.16	0.0 ± 0.3	3880 ± 70
NGC6822-RSG07	2	3.9 ± 0.4	-0.58 ± 0.19	0.4 ± 0.5	3970 ± 60	3.8 ± 0.5	-0.56 ± 0.14	0.1 ± 0.5	3990 ± 80
NGC6822-RSG08	3	3.0 ± 0.4	-0.58 ± 0.24	0.6 ± 0.5	3910 ± 100	3.0 ± 0.4	-0.58 ± 0.24	0.6 ± 0.5	3910 ± 100
NGC6822-RSG09	4	3.7 ± 0.4	-0.38 ± 0.16	0.1 ± 0.4	3980 ± 60	3.6 ± 0.4	-0.44 ± 0.17	-0.1 ± 0.5	3990 ± 80
NGC6822-RSG10	14	3.7 ± 0.4	-0.67 ± 0.16	-0.3 ± 0.5	3900 ± 80	3.5 ± 0.4	-0.59 ± 0.19	-0.3 ± 0.5	3850 ± 80
NGC6822-RSG11	15	4.2 ± 0.5	-0.53 ± 0.19	-0.4 ± 0.5	3870 ± 80	4.3 ± 0.5	-0.49 ± 0.17	-0.3 ± 0.4	3850 ± 60
NGC6822-RSG14	17	3.6 ± 0.5	-0.20 ± 0.21	-0.5 ± 0.5	3910 ± 110	3.6 ± 0.5	-0.15 ± 0.24	-0.5 ± 0.5	3880 ± 110
NGC6822-RSG17	21	3.0 ± 0.4	-0.43 ± 0.28	0.1 ± 0.5	3890 ± 120	3.0 ± 0.4	-0.43 ± 0.28	0.1 ± 0.5	3890 ± 120
NGC6822-RSG18	18	2.2 ± 0.4	-0.68 ± 0.31	0.4 ± 0.5	3810 ± 130	2.1 ± 0.5	-0.54 ± 0.41	0.4 ± 0.5	3740 ± 130

Table 5.6 *Fit parameters including and excluding Mg I lines*

Target	IFU	24 Arm Telluric without Mg I				24 Arm Telluric with Mg I			
		ξ (km s^{-1})	[Z]	$\log g$	$T_{\rm eff}$(K)	ξ (km s^{-1})	[Z]	$\log g$	$T_{\rm eff}$(K)
NGC6822-RSG01	6	3.5 ± 0.4	-0.55 ± 0.18	-0.0 ± 0.3	3790 ± 80	3.4 ± 0.2	-0.49 ± 0.12	0.4 ± 0.25	3830 ± 65
NGC6822-RSG02	11	3.5 ± 0.4	-0.78 ± 0.22	0.4 ± 0.5	3850 ± 100	3.6 ± 0.6	-0.78 ± 0.33	1.0 ± 0.25	3850 ± 50
NGC6822-RSG04	12	4.0 ± 0.4	-0.32 ± 0.16	0.0 ± 0.3	3880 ± 70	4.2 ± 0.3	-0.34 ± 0.11	0.6 ± 0.25	3855 ± 50
NGC6822-RSG07	2	3.9 ± 0.4	-0.58 ± 0.19	0.4 ± 0.5	3970 ± 60	4.5 ± 0.3	-0.73 ± 0.08	0.9 ± 0.25	4005 ± 59
NGC6822-RSG08	3	3.0 ± 0.4	-0.58 ± 0.24	0.6 ± 0.5	3910 ± 100	2.1 ± 0.4	-0.18 ± 0.09	0.9 ± 0.25	3850 ± 50
NGC6822-RSG09	4	3.7 ± 0.4	-0.38 ± 0.16	0.1 ± 0.4	3980 ± 60	4.0 ± 0.2	-0.69 ± 0.08	-0.6 ± 0.25	3925 ± 50
NGC6822-RSG10	14	3.7 ± 0.4	-0.67 ± 0.16	-0.3 ± 0.5	3900 ± 80	4.0 ± 0.2	-0.61 ± 0.07	0.1 ± 0.25	3970 ± 50
NGC6822-RSG11	15	4.2 ± 0.5	-0.53 ± 0.19	-0.4 ± 0.5	3870 ± 80	4.6 ± 0.2	-0.55 ± 0.06	0.1 ± 0.25	3930 ± 50
NGC6822-RSG14	17	3.6 ± 0.5	-0.20 ± 0.21	-0.5 ± 0.5	3910 ± 110	3.9 ± 0.2	-0.42 ± 0.08	1.0 ± 0.25	4050 ± 50
NGC6822-RSG17	21	3.0 ± 0.4	-0.43 ± 0.28	0.1 ± 0.5	3890 ± 120	2.9 ± 0.4	-0.40 ± 0.22	0.6 ± 0.25	3880 ± 130
NGC6822-RSG18	18	2.2 ± 0.4	-0.68 ± 0.31	0.4 ± 0.5	3810 ± 130	1.3 ± 0.3	-0.46 ± 0.23	1.0 ± 0.25	3650 ± 50

5.4.2 The Introduction of Magnesium

Since the publication of Patrick et al. (2015, where the results from this chapter are published), non-LTE corrections have been calculated by Bergemann et al. (2015). Using these results, the model grids have now been updated to include the corrections for non-LTE for the Mg I lines. As an additional calibration to these corrections (to the extensive testing in Bergemann et al., 2015) I have used the updated model grids to re-analyse the NGC 6822 KMOS spectra. This allows a direct comparison between results including and excluding the Mg I lines.

Figure 5.9 displays a comparison between stellar parameters estimated including and excluding the two Mg I lines using a set of simulated spectra. This test demonstrates that the agreement between stellar parameters including these additional features is very good. In general, the errors on each parameter are systematically slightly reduced by including these lines. One target with a very small estimated uncertainty for the surface gravity parameter (again shown in Figure 5.9 for illustration, rather than boosted to the minimum value of ± 0.25), when the Mg I lines are included, has an offset of ~ 0.75 with respect to the input parameter. Whereas when Mg I lines are included, this parameter is recovered very precisely. This adds strength to a minimum uncertainty for the surface gravity parameter of ± 0.25.

Figure 5.10 displays the stellar parameters estimated including and excluding the two Mg I lines. This figure also shows that there is reasonable agreement between the parameters, however, there is a significant offset in the estimated effective temperatures (61 ± 39 K). This offset is a result of the different techniques used to estimate the parameters, rather than an effect of including the Mg I lines. Table 5.6 details the parameters.

For the remainder of this chapter I adopt the updated stellar parameters including the non-LTE effects of magnesium, unless explicitly stated.

5.4.3 Stellar Parameters and Metallicity

Table 5.6 summarises the estimated stellar parameters. For the remainder of this chapter, when discussing stellar parameters, we adopt those estimated using the 24 arm telluric method including the Mg I lines. (i.e. the results in the left-hand part of Table 5.6.) The average metallicity for our sample of 11 RSGs

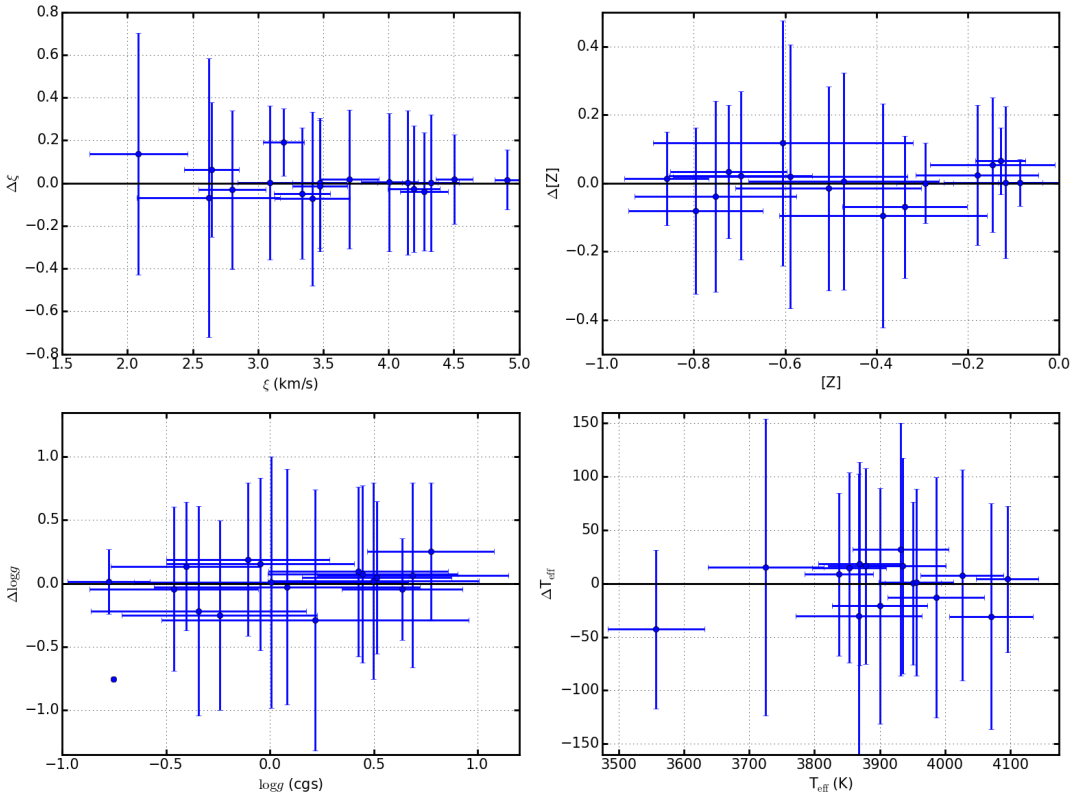

Figure 5.9 *Comparison of the model parameters including and excluding Mg I lines for a set of simulated spectra. As in Figure 5.10, in each panel, the x-axis represents stellar parameters estimated including the Mg I lines and the y-axis represents the difference between the parameters estimated including and excluding the Mg I lines (i.e.* $\Delta X = output_{\rm mg} - output_{\rm no-mg}$*). This figure shows that there is generally good agreement between parameters when including additional stellar lines.*

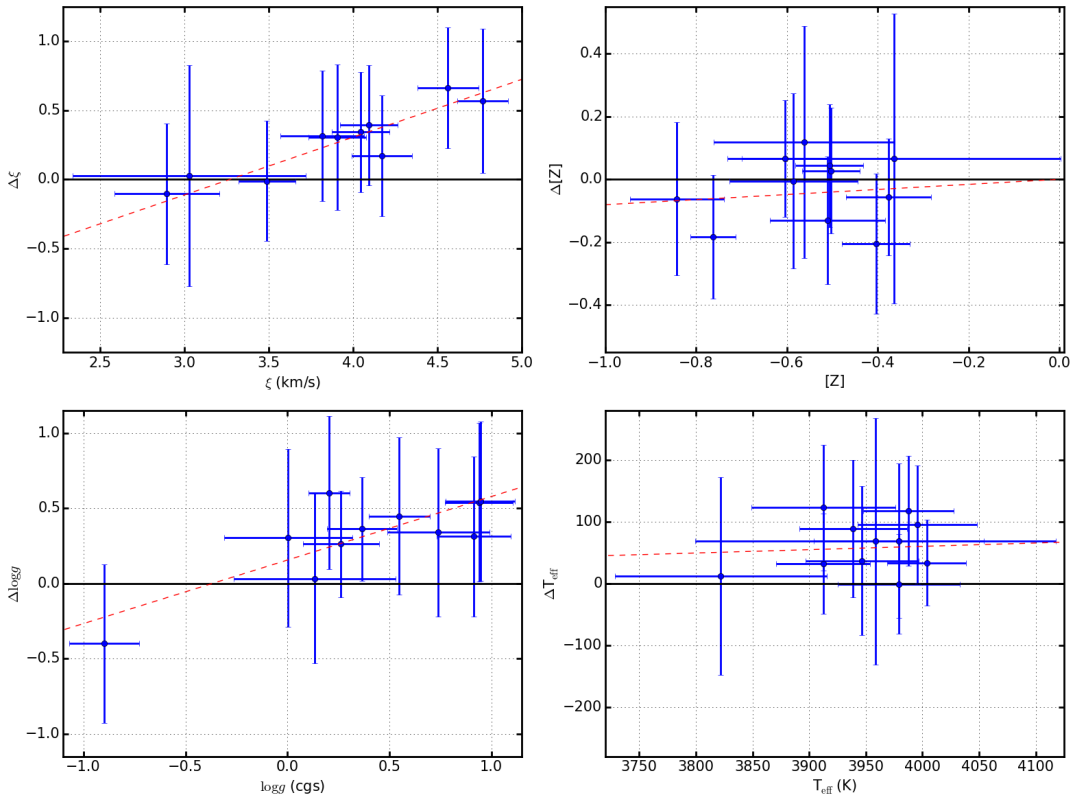

Figure 5.10 *Comparison of the model parameters including and excluding Mg I lines. In each panel, the x-axis represents stellar parameters estimated including the Mg I lines and the y-axis represents the difference between the parameters estimated including and excluding the Mg I lines (i.e.* $\Delta X = output_{\rm mg} - output_{\rm no-mg}$*). Top left: Microturbulence (*ξ*), mean difference* $< \Delta\xi > = 0.17 \pm 0.38\,km\ s^{-1}$*. Top right: metallicity ([Z]), mean difference* $< \Delta[Z] > = -0.03 \pm 0.10$ *dex. Bottom left: surface gravity (*$\log g$*), mean difference* $< \Delta log\, g > = 0.11 \pm 0.37$*. Bottom right: effective temperature (*$T_{\rm eff}$*), mean difference* $< \Delta T_{\rm eff} > = 61 \pm 39\,K$*. Red dashed lines indicates linear fits to the data.*

in NGC 6822 is [Z] = -0.52 ± 0.13. This result is in good agreement with the average metallicity estimated in Patrick et al. (2015, see also Figure 5.11). In addition the results presented here are also in good agreement with results using BSGs (BSGs; Muschielok et al., 1999; Venn et al., 2001).

A direct comparison with metallicities from BSGs is legitimate as the method used in the present analysis yield a global metallicity ([Z]) which closely resembles the Fe/H ratio estimated in Venn et al. (2001). While our [Z] measurements are also affected by Si and Ti, we assume [Z] = [Fe/H] for the purposes of our discussion. Likewise, I can compare oxygen abundances (relative to solar) obtained from H II regions as a proxy for [Z] by introducing the solar oxygen abundance $12 + \log(\mathrm{O/H})_\odot = 8.69$ (Asplund et al., 2009) through the relation $[\mathrm{Z}] = 12 + \log(\mathrm{O/H})$ - 8.69. This implicitly assumes that the α/Fe ratio remains Solar in different environments.

As outlined in Chapter 1 the RSG and BSG stages are different evolutionary phases within the life cycle of a massive star, while H II regions are the birth clouds which give rise to the youngest stellar population. As the lifetimes of RSGs and BSGs are < 50Myr, their metallicity estimates are also expected to be representative of their birth clouds.

To investigate the spatial distribution of chemical abundances in NGC 6822, in Figure 5.11 we show the metallicities of our RSGs as a function of radial distance from the centre of the galaxy, as well as the results from Venn et al. (2001) and the indicative estimates from Muschielok et al. (1999).

A linear least-squares fit to the results from Patrick et al. (2015) reveals a low-significance abundance gradient within the central 1 kpc of NGC 6822 of -0.5 ± 0.4 dex/kpc. In addition, the extrapolated central metallicity from the fit (i.e. at R = 0) of [Z] = -0.30 ± 0.15 dex remains consistent with the average metallicity assuming no gradient. However, using the updated stellar parameters the data appears consistent with no gradient (-0.12 ± 0.19 dex/kpc) even though statistically this is a poorer fit to the data.

Figure 5.12 shows the location of our sample in the H-R diagram. Bolometric corrections were computed using the calibration in Davies, B. et al. (2013). This figure shows that the temperatures estimated using the J-band method are systematically cooler than the end of the evolutionary models (which terminate at the end of the carbon-burning phase for massive stars) for Z = 0.002 from Georgy et al. (2013). This result is discussed in Section 5.5.2.

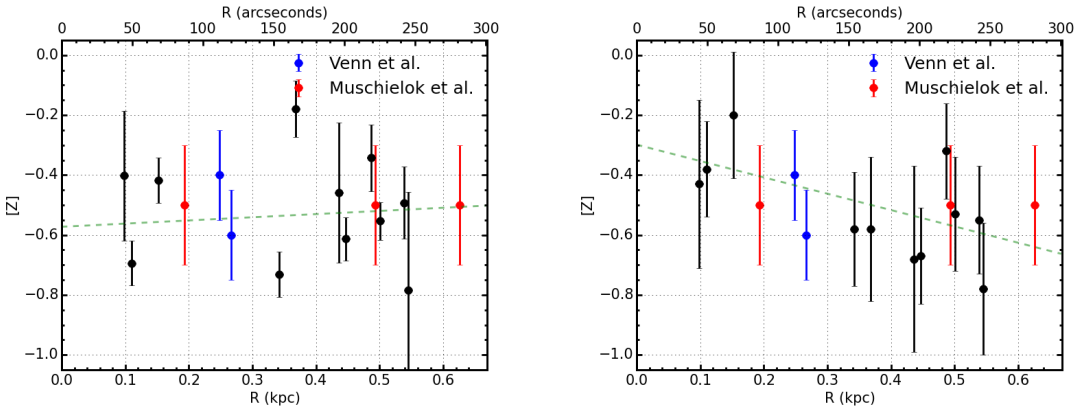

Figure 5.11 *Estimated metallicities for 11 RSGs in NGC 6822 shown against their distance from the galaxy centre. The left panel shows the metallicities estimated including Mg I lines whereas the right hand panel shows metallicities excluding Mg I. Blue and red points show BSG results from Venn et al. (2001) and Muschielok et al. (1999) respectively. The average metallicity is consistent between the two samples and the average including Mg I is adopted at [Z] = −0.52 ± 0.13. A least-squares fit to the results excluding Mg I (right panel) reveals a low-significance abundance gradient (see text for details). For comparison, R_{25} = 460 arcseconds (= 1.03 kpc; McConnachie, 2012).*

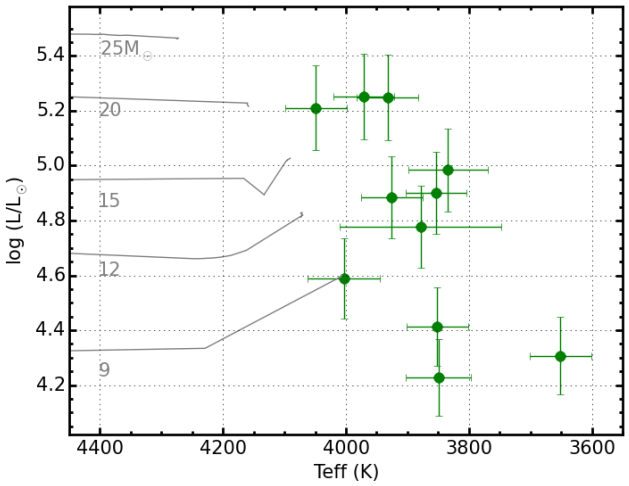

Figure 5.12 *Hertzsprung–Russell diagram for the 11 RSGs in NGC 6822. Evolutionary tracks including rotation (v/v_c = 0.4) for SMC-like metallicity (Z = 0.002) are shown in grey, along with their zero-age mass (Georgy et al., 2013). Bolometric corrections are computed using the calibration in Davies, B. et al. (2013). We note that compared to the evolutionary tracks, the observed temperatures of NGC 6822 RSGs are systematically cooler. This is discussed in Section 5.5.2.*

5.5 Discussion

5.5.1 Metallicity Measurements

The average metallicity for the sample is [Z] = -0.52 ± 0.13, which agrees well with the results estimated from BSGs (Muschielok et al., 1999; Venn et al., 2001; Przybilla, 2002) and H II regions (Lee, Skillman & Venn, 2006). These results are consistent with no metallicity gradient within NGC 6822.

Using the data from Patrick et al. (2015, i.e excluding Mg I) there exists a low-significance metallicity gradient within the central 1 kpc of NGC 6822 (-0.5 ± 0.4 dex/kpc with a $\chi^2_{red} = 1.16$; see Figure 5.11). The gradient estimated is consistent with the trend reported in Venn et al. (2001) from their results for the two BSGs which these authors compared with H II regions (Pagel, Edmunds & Smith, 1980) and two planetary nebulae (Richer & McCall, 1995) at larger galactocentric distances. This result is also consistent with the gradient estimated from a sample of 49 local star-forming galaxies (Ho et al., 2015). Including the results for BSGs from Venn et al. (2001) in the analysis, gives a consistent gradient (-0.48 ± 0.33 dex/kpc) with an improved $\chi^2_{red} = 1.06$. Results from Muschielok et al. (1999) are not included in the fit as these measurements were qualitative estimates of metallicity.

In contrast, Lee, Skillman & Venn (2006) used the oxygen abundances from 19 H II regions and found no clear evidence for a metallicity gradient. Using a subset of the highest quality H II region data available, these authors found a gradient of -0.16 ± 0.05 dex/kpc. Including these results into our analysis degrades the fit and changes the estimated gradient significantly (-0.18 ± 0.05 dex/kpc; $\chi^2_{red} = 1.78$). However, when this data is combined with the RSG data including the Mg I lines, a significant gradient is measured (-0.13 ± 0.04 dex/kpc; $\chi^2_{red} = 2.91$). At this point it is not clear whether the indication of a gradient obtained from the RSGs and BSGs is an artefact of the small sample size, or indicates a difference with respect to the H II region study.

There have been a number of studies of the metallicity of the older stellar population in NGC 6822. From spectroscopy of red giant branch (RGB) stars, Tolstoy et al. (2001) found a mean metallicity of [Fe/H] = -0.9 with a reasonably large spread (see their Figure 19). More recently, Sibbons et al. (2012) derived metallicities using a population of AGB stars within the central 4 kpc

of NGC 6822. They found an average metallicity of [Fe/H] = -1.29 ± 0.07 dex. Likewise, Kirby et al. (2013) used spectra of red giant stars within the central 2 kpc and found an average metallicity of [Fe/H] = -1.05 ± 0.49 dex. We note that none of these studies found any compelling evidence for spatial variations in the stellar metallicities, which is not surprising given that, in disc galaxies, radial migration is thought to smooth out any abundance gradients over time. The stellar populations used for these studies are known to be significantly older than our sample, therefore, owing to the chemical evolution in the time since the birth of the older populations, we expect the measured metallicities to be significantly lower.

The low metallicity of the young stellar population and the interstellar medium (ISM) in NGC 6822 can be understood as a consequence of the fact that it is a relatively gas-rich galaxy with a mass $M_{HI} = 1.45 \times 10^8\,M_\odot$ (Koribalski et al., 2004) and a total stellar mass of ranging from $M_* = 0.83$ - $1.70 \times 10^8\ M_\odot$ (Woo, Courteau & Dekel, 2008; Kirby et al., 2013; Weisz et al., 2014).

The simple closed-box chemical-evolution model relates the metallicity mass fraction $Z(t)$ at any time to the ratio of stellar to gas mass M_*/M_g through

$$Z(t) = \frac{y}{1-R} \ln\left[1 + \frac{M_*(t)}{M_g(t)}\right], \tag{5.2}$$

where y is the fraction of metals per stellar mass produced through stellar nucleosynthesis (the so-called yield) and R is the fraction of stellar mass returned to the ISM through stellar mass-loss.

According to Kudritzki et al. (2015), the ratio $y/(1-R)$ can be empirically determined from the fact that the metallicity of the young stellar population in the solar neighbourhood is solar, with a mass fraction $Z_\odot = 0.014$ (Nieva & Przybilla, 2012). With a stellar-to-gas mass column density of 4.48 in the solar neighbourhood (Wolfire et al., 2003; Bovy & Rix, 2013) one then obtains $y/(1-R) = 0.0082 = 0.59 Z_\odot$ with an uncertainty of 15 percent dominated by the 0.05 dex uncertainty of the metallicity determination of the young population.

Accounting for the presence of helium and metals in the neutral interstellar gas I can turn the observed HI mass in NGC 6822 into a gas mass via $M_g = 1.36\,M_{HI}$ and use the simple closed-box model to predict a metallicity of [Z] = -0.44 - -0.69, in good agreement with our value obtained from RSG spectroscopy.

As discussed above, the older stellar population of AGB stars has a metallicity roughly 0.8 dex lower than the RSGs. In the framework of the simple closed-box model this would correspond to a period in time where the ratio of stellar to gas mass was ∼0.1 (much lower than the present value of 0.42-0.86). The present star-formation rate of NGC 6822 is $\sim 0.02\,M_{\odot}yr^{-1}$ (Gratier et al., 2010; Efremova et al., 2011). At such a high level of star formation it would have taken five Gyr to produce the presently observed stellar mass and to arrive from the average metallicity of the AGB stars to that of the young stellar population (of course, again relying on the simple closed-box model). Evidence suggests that the star-formation rate was substantially lower in the past (Efremova et al., 2011; Weisz et al., 2014), therefore, the build up of the observed stellar mass would have taken correspondingly longer.

Given the irregularities present in the stellar and gaseous morphology of NGC 6822, this galaxy may not be a good example of a closed-box system, however it is remarkable that the closed-box model reproduces the observed metallicity so closely.

5.5.2 Temperatures of RSGs

Effective temperatures have been estimated for 11 RSGs from our observed sample in NGC 6822. To date, this represents the fourth data set used to estimate stellar parameters in this way and the first with KMOS. The previous three data sets which have been analysed are those of 11 RSGs in PerOB1, a Galactic OB association (Gazak et al., 2014b), nine RSGs in the LMC and 10 RSGs in the SMC (both from Davies et al., 2015). These results range from $Z = Z_{\odot}$ in PerOB1 to $Z = 0.3Z_{\odot}$ in the SMC, around 0.5 dex in metallicity.

The effective temperatures estimated in this study are compared with those of the previous results in different environments. Their distribution is shown as a function of metallicity in Figure 5.13. Additionally, Figure 5.14 shows the H-R diagram for the four sets of results. Bolometric corrections to calculate the luminosities for each sample were computed using the calibration in Davies, B. et al. (2013).

From these figures, I see no evidence for significant variations in the average temperatures of RSGs with respect to metallicity. This is in contrast to current evolutionary models which display a change of ∼450 K, for a $M = 15\,M_{\odot}$ model,

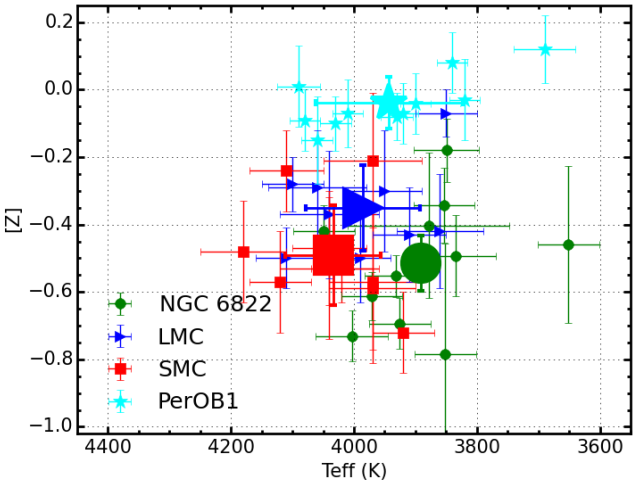

Figure 5.13 *Effective temperatures as a function of metallicity for four different data sets using the J-band analysis technique. There appears to be no significant variation in the temperatures of RSGs over a range of 0.55 dex. These results are compiled from the LMC, SMC (blue and red points respectively; Davies et al., 2015), PerOB1 (a Galactic RSG cluster; cyan; Gazak et al., 2014b) and NGC 6822 (green). Mean values for each data set are shown as enlarged points in the same style and colour. The x-axis is reversed for comparison with Figure 5.14.*

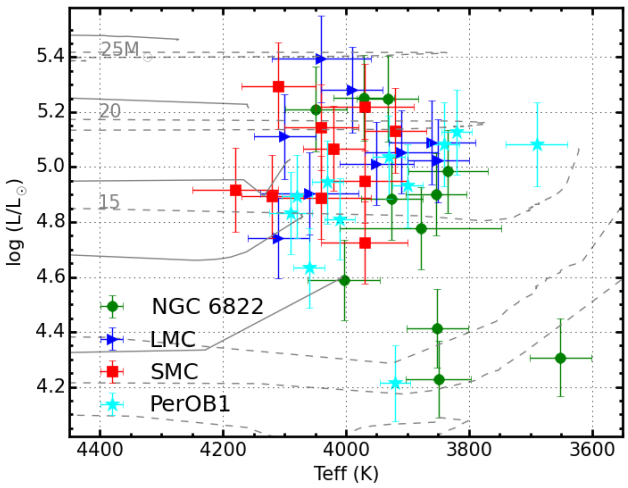

Figure 5.14 *Hertzsprung–Russell diagram for RSGs in PerOB1 (cyan), LMC (blue), SMC (red) and NGC 6822 (green) which have stellar parameters obtained using the J-band method. This figure shows that there appears to be no significant temperature differences between the four samples. Solid grey lines show SMC-like metallicity evolutionary models including rotation (Georgy et al., 2013). Dashed grey lines show solar metallicity evolutionary models including rotation (Ekström et al., 2012).*

over a range of solar to SMC-like metallicities (Ekström et al., 2012; Georgy et al., 2013).

For solar metallicity, observations in PerOB1 are in good agreement with the models (see Figure 9 in Gazak et al., 2014b). However, at SMC-like metallicity, the end-points of the models are systematically warmer than the observations. The temperature of the end-points of the evolutionary models of massive stars could depend on the choice of the convective mixing-length parameter (Schaller et al., 1992). That the models produce a higher temperature than observed could imply that the choice of a solar-like mixing-length parameter does not hold for higher-mass stars at lower metallicity.

Lastly, I note that the average spectral type of RSGs tends towards an earlier spectral type with decreasing metallicity over this range (Humphreys, 1979; Levesque & Massey, 2012). Following the arguments in Humphreys (1979) this is not in contradiction to the above results. Spectral types are measured for RSGs using the optical TiO band-heads at $\sim$0.65 μm, whereas in this study temperatures are estimated using near-IR atomic features (as well as the line-free pseudo-continuum). The strengths of TiO bands are dependent upon metallicity which means that the spectral classification for RSGs at a constant temperature will differ (Davies, B. et al., 2013). Therefore, although historically spectral type has been used as a proxy for temperature, this assumption does not provide an accurate picture for RSGs.

5.5.3 AGB Contamination

As mentioned in Section 5.2.1, massive AGB stars are potential contaminants to our sample. These stars have similar properties to RSGs and can occupy similar mass ranges as lower-mass RSGs (Herwig, 2005), however, their lifetimes are around $\sim$25 Myr (Doherty et al., 2010). Wood, Bessell & Fox (1983) argued for an AGB luminosity limit (owing to the limit on the mass of the degenerate core) of $M_{bol} \sim -7.1$. Using this maximum luminosity, corrected for the distance to NGC 6822, yields $K = 14.0$. Four of our analysed stars have K-band magnitudes fainter than this limit, but excluding the results for these does not significantly alter any of our conclusions (and arguably, they would still be tracing the young stellar population).

5.6 Conclusions

KMOS spectroscopy of RSGs in NGC 6822 is presented. The data were telluric corrected in two different ways and the standard 3 arm telluric method is shown to work as effectively (in most cases) as the more time expensive 24 arm telluric method. Radial velocities of the targets are measured and are shown to be consistent with previous results in NGC 6822, confirming their extragalactic nature.

Stellar parameters are calculated for 11 RSGs using the J-band analysis method outlined in Davies, Kudritzki & Figer (2010). The average metallicity within NGC 6822 is $[\mathrm{Z}] = -0.52 \pm 0.13$ dex, consistent with previous abundance studies of young stars. We find an indication of a metallicity gradient within the central 1 kpc, however with a low significance caused by the small size and limited spatial extent of our RSG sample. To conclusively assess the presence of a metallicity gradient among the young population within NGC 6822 a larger systematic study of RSGs is needed.

The chemical abundances of the young and old stellar populations of NGC 6822 are well explained by a simple closed-box chemical evolution model. However, while an interesting result, I note that the closed-box model is unlikely to be a good assumption for this galaxy given its morphology.

The effective temperatures of RSGs in this study are compared to those of all RSGs analysed using the same method. Using results which span 0.55 dex in metallicity (Solar to SMC) within four galaxies, I find no evidence for a systematic variation in average effective temperature with respect to metallicity. This is in contrast with evolutionary models which, for a similar change in metallicity, produces a shift in the temperature of RSGs of up to 450 K. We argue that an observed shift in average spectral type of RSGs over this metallicity range does not imply a shift in average temperature.

Chapter 6

First steps outside the Local Group of Galaxies: Red Supergiants in NGC 55

6.1 Opening Remarks

To improve the quality of the data reduction I enlisted the help of a fellow student, Owen Turner, who has provided some additional corrections to the standard KMOS/esorex pipeline to correct for the readout bias and to improve the pipeline's bad pixel map. Details of this procedure are given in the text and the reader is referred to Turner et al. (in prep) for a more in depth discussion of the steps taken.

The results in this chapter have been calculated using a previous version of the analysis routine presented in Chapter 3. The effect of this update is small, and the affect on the results in this chapter may be that the uncertainties on the parameters are slightly underestimated.

6.2 Introduction

NGC 55 is a galaxy located outside of the Local Group of Galaxies within the Sculptor Group at a distance of 1.94 ± 0.03 Mpc (Pietrzyński et al., 2006; Gieren

et al., 2008) which, before the emergence of the Araucaria Project (Gieren et al., 2005), had been subject to considerable uncertainty (e.g. Pritchet et al., 1987; van de Steene et al., 2006).

The Sculptor "Group" includes five massive galaxies (NGC 55, NGC 247, NGC 253, NGC 300 and NGC 7793) and numerous (∼20) dwarf galaxies. NGC 253 is a large starburst galaxy and is the brightest and most massive of the group. This is the closest group of galaxies to the Local Group, and offers a fantastic laboratory to test theories of stellar and galactic evolution as, from the ground, one can resolve individual stars within these galaxies.

Association to the Sculptor Group however, is a contentious issue. By revising distances for nine of the Sculptor Group dwarfs Karachentsev et al. (2003) postulated that the Sculptor group was actually filament-like, which intersects the Milky Way group, where NGC 55 and NGC 300 and their surrounding satellite galaxies were potentially not associated with the main group of galaxies in this filament. Regardless of the geometry and association to the Sculptor Group, NGC 55 is the nearest large galaxy to the MW group in the direction of the Sculptor Group.

The morphology of NGC 55 is asymmetric and complicated owing to the high inclination angle (up to 80°; Hummel, Dettmar & Wielebinski, 1986; Westmeier, Koribalski & Braun, 2013). de Vaucouleurs (1961) classified this galaxy as an LMC-like spiral barred galaxy (SB(s)m) where the bar is seen along the line of sight, prompting various claims that this galaxy is an edge-on analogue of the LMC (e.g. Robinson & van Damme, 1964, although not cited heavily – two citations in 50 years – the idea has propagated). Figure 6.1 shows NGC 55 and its complicated morphology where one can see the edge-on disk along the major axis of the galaxy and the brighter central part of the galaxy represents the head of the bar. In addition to NGC 55 being orientated nearly edge on, extending from the disk-bar system there exists many star-formation features, such as giant H II regions as well as supergiant filaments and shells that are thought to allow ionising radiation to be transported to the halo where star-formation is currently occurring (Ferguson, Wyse & Gallagher, 1996).

The morphology of NGC 55, as well as its known population of massive hot stars (Castro et al., 2008, 2012), points to a recent history of intense star formation. This is supported by the infrared morphology of NGC 55 which is dominated by young star-forming features (with a star-formation rate of

Figure 6.1 *Image of NGC 55 where the edge-on disk of the galaxy makes up the major axis and the bright central region represents the head of the bar containing intense star-forming regions. Image from the Wide Field Imager on the 2.2-metre MPG/ESO telescope at ESO La Silla Observatory. Credit: ESO, press release.*

$0.22\,M_{\odot}yr^{-1}$; Engelbracht et al., 2004) as well as indications from near-IR imaging (Davidge, 2005).

The metal content of NGC 55 is expected to be LMC-like, which is supported by Castro et al. (2012) who measured metallicities of 12 blue supergiants using optical spectroscopy and found a mean metallicity $[Z] = -0.40 \pm 0.13$ dex. In addition, Webster & Smith (1983) measure abundances of seven H II regions across the disk of NGC 55 using the strong-line method (as well as four measurements of the auroral "direct" line method) and found a similar LMC-like metallicity.

Even though the hot massive star population of NGC 55 has been explored, there are currently no confirmed RSGs in NGC 55, although Davidge (2005) note that the near-IR CMDs of fields within the disk of NGC 55 reveal signatures of RSGs. This study represents the first quantitative study of RSGs in NGC 55 and, by measuring metallicities of this population, will provide a crucial test of the metallicity gradient within this galaxy.

In this chapter, I describe the observations and data reduction procedure in Section 6.3 and highlight the target selection method and its uncertainties. I then present the main results of the chapter in Section 6.5 where I first measure

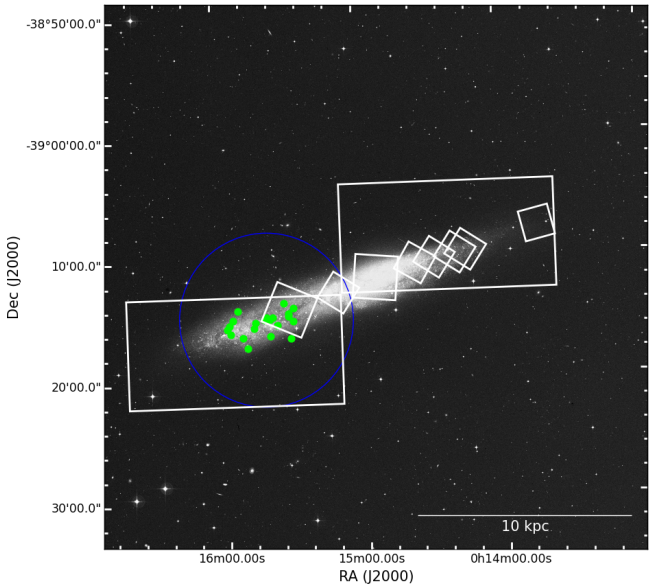

Figure 6.2 *Digital sky survey image of NGC 55 with KMOS targets overlaid in green and photometric footprints from the Araucaria Project (Gieren et al., 2005) in white rectangles and the ANGST project (Dalcanton et al., 2009) in the smaller white squares.*

radial velocities for each epoch of the RGSs, confirming their membership of NGC 55, and then go on to measure stellar parameters for each target using the J-band analysis technique described in detail in Chapter 3. The main conclusions are presented in Section 6.6.

6.3 Observations

6.3.1 Target Selection

Targets were selected based on their optical photometry from the the Araucaria Project (Gieren et al., 2005) where the footprints for this project are highlighted with large white rectangles in Figure 6.2. The optical CMD which is used to select targets is displayed in the left hand panel of Figure 6.3, where the RSG candidates are within the black box and the observed targets are highlighted in red. This method of target selection is preferred as a result of the limited extent of near-IR photometry in this area.

Candidate RSGs, illustrated by the black box in the left hand panel of Figure 6.3, are defined as $17 < I < 19$ and $1.2 < V - I < 3.5$. The magnitude limit here is

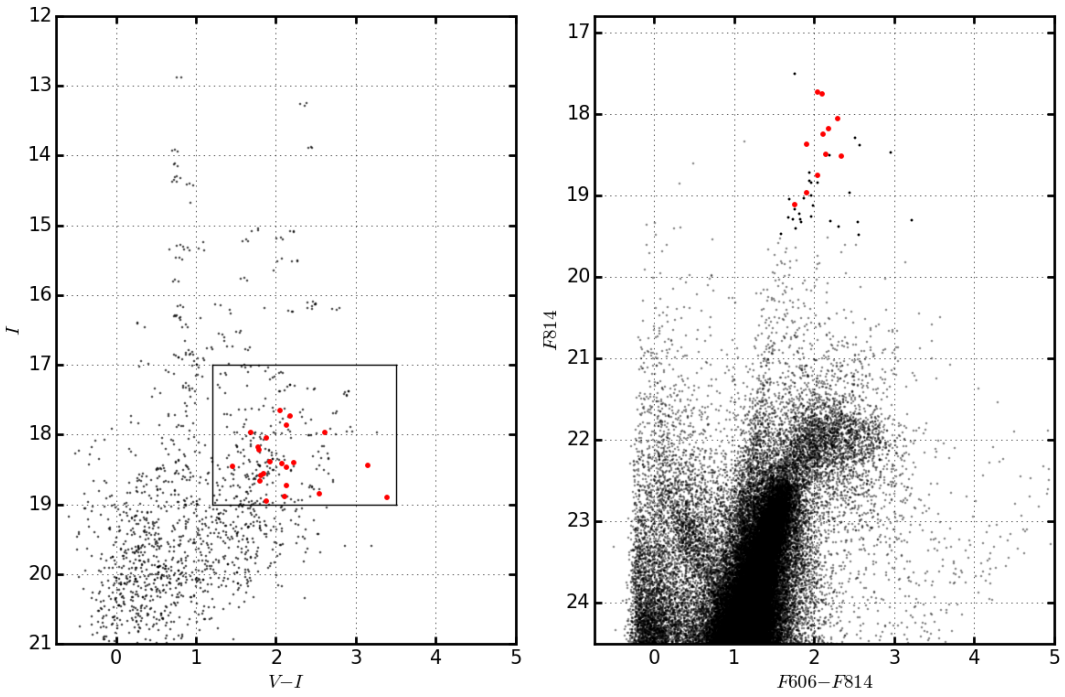

Figure 6.3 *NGC 55 ground- and space-based colour–magnitude diagrams. Left hand panel shows $V - I$, I data from the ground-based Araucaria Project Gieren et al. (2005) over the entire field-of-view (Fov) of the KMOS observations. The black box defines candidate RSGs that are defined as $17 < I < 19$ and $1.2 < V - I < 3.5$. Right hand panel shows data from the ACS Nearby Galaxy Survey Treasury project (ANGST; Dalcanton et al., 2009), where photometry from this project covers only a portion of the KMOS FoV (see Figure 6.2).*

a result of the expected magnitudes of RSGs in NGC 55 (e.g. Gazak et al., 2015, who identified RSGs in NGC 300) and the $V - I$ colour limit is chosen to avoid potential Galactic contamination at $V - I \sim 0.95$. All stars that meet this criteria are defined as candidate RSGs and the final target selection was performed by analysing the spatial location of the candidates and selecting those which traced the disk population of NGC 55 (see Figure 6.2).

In addition to the ground-based photometry available, the ACS Nearby Galaxy Survey Treasury project (ANGST; Dalcanton et al., 2009) has publicly available photometry for several fields within the disk of NGC 55 that are displayed as small white squares in Figure 6.2. A F814W, F606W−F814W CMD is shown in the right hand panel of Figure 6.3 for the ANGST field that contains 11 of our KMOS targets, where observed KMOS targets are highlighted in red. Given the smaller spatial coverage of the HST Advanced Camera for Surveys (ACS) field, the expected number of Galactic contaminants is correspondingly smaller. To add to this, as a result of their cool temperatures and extreme luminosities, RSGs should exist in a "plume" at the tip of a structure of cool stars in the F606W−F814W, F814W CMD (assuming no contamination). This compares well to the location (in colour–magnitude parameter space) of confirmed RSGs in NGC 300 (Gazak et al., 2015). Therefore, all candidates with HST photometry are classified as priority one targets.

Table 6.1 shows ground- and space-based optical photometry of the KMOS targets along with their radial velocities that confirm many of these targets as NGC 55 RSGs (see Section 6.5.1).

6.4 Observations and Data Reduction

These observations are part of the the KMOS guaranteed time observations (GTO; ESO ID: 092.B-0088(A)) that was proposed to investigate the spatial distribution of metallicities NGC 55 and NGC 300, both at d = 1.9 Mpc. This included three pointings in NGC 55 containing ∼60 RSG candidates. However, during the observations in October 2013, as a result of poor conditions, only half the requested time on one field in NGC 55 was observed. In order to supplement this partially completed field, the proposal was re-submitted as a back-up OB for subsequent GTO.

Table 6.1 *Summary of VLT-KMOS targets in NGC 55*

ID	α (J2000)	δ (J2000)	V[a]	I[a]	F606W[b]	F814W[b]		rv (km s^{-1})			$\langle rv \rangle$ (km s^{-1})	Notes
								14-09-2013	16-10-2013	14-09-2014	15-09-2014	
NGC55-RSG19	00:15:29.190	−39:14:08.20	19.914	17.731	19.85	17.76	205 ± 4	178 ± 7	222 ± 10	191 ± 7	199 ± 14	
NGC55-RSG20	00:15:29.520	−39:15:13.00	20.832	18.952	20.86	19.11	194 ± 14	220 ± 5	–	–	217 ± 10	
NGC55-RSG22	00:15:30.520	−39:16:36.70	20.406	18.589	–	–	95 ± 14	-41 ± 26	–	–	–	
NGC55-RSG24	00:15:31.460	−39:14:46.30	20.612	18.475	20.29	18.38	186 ± 6	194 ± 7	146 ± 38	237 ± 16	192 ± 16	
NGC55-RSG25	00:15:31.490	−39:14:32.40	20.316	18.394	20.63	18.49	204 ± 12	217 ± 16	-376 ± 41[c]	151 ± 23	200 ± 26	
NGC55-RSG26	00:15:33.160	−39:13:42.00	20.572	17.964	20.35	18.06	174 ± 9	173 ± 8	–	–	173 ± 1	
NGC55-RSG28	00:15:36.160	−39:15:29.40	21.001	18.892	20.87	18.97	233 ± 17	161 ± 20	–	–	203 ± 41	
NGC55-RSG30	00:15:38.030	−39:14:50.20	20.867	18.730	20.79	18.75	212 ± 10	215 ± 10	-424 ± 21[c]	212 ± 22	213 ± 2	
NGC55-RSG35	00:15:39.260	−39:15:01.70	20.007	17.872	19.78	17.73	202 ± 3	206 ± 4	223 ± 13	200 ± 11	204 ± 5	
NGC55-RSG36	00:15:39.520	−39:16:23.10	19.915	18.462	–	–	-188 ± 31	-284 ± 16	-588 ± 35	346 ± 12	–	
NGC55-RSG39	00:15:40.260	−39:15:01.00	19.654	17.970	20.36	18.19	206 ± 11	192 ± 5	-1 ± 30[c]	126 ± 30	193 ± 14	
NGC55-RSG43	00:15:40.700	−39:14:50.20	19.957	18.183	20.36	18.25	-220 ± 20[c]	196 ± 5	173 ± 17	31 ± 38[c]	194 ± 9	
NGC55-RSG46	00:15:41.640	−39:14:58.80	21.591	18.441	20.85	18.52	228 ± 5	195 ± 6	-128 ± 18[c]	210 ± 8	214 ± 18	
NGC55-RSG57	00:15:45.590	−39:15:16.40	20.010	18.220	–	–	217 ± 10	197 ± 6	207 ± 13	177 ± 6	193 ± 16	
NGC55-RSG58	00:15:46.270	−39:15:43.20	20.619	18.400	–	–	236 ± 8	216 ± 3	214 ± 21	210 ± 13	218 ± 8	
NGC55-RSG60	00:15:49.180	−39:17:19.80	21.393	18.847	–	–	-73 ± 39	26 ± 26	-533 ± 39	94 ± 37	–	
NGC55-RSG65	00:15:51.250	−39:16:26.40	19.706	17.653	–	–	224 ± 5	215 ± 4	217 ± 6	215 ± 6	218 ± 4	
NGC55-RSG67	00:15:53.110	−39:14:13.60	19.925	18.047	–	–	25 ± 24[c]	6 ± 31[c]	37 ± 14[c]	175 ± 18	175 ± 18	
NGC55-RSG69	00:15:55.280	−39:15:00.10	20.470	18.666	–	–	231 ± 5	195 ± 9	130 ± 14[c]	220 ± 23	222 ± 18	
NGC55-RSG70	00:15:56.310	−39:16:08.60	22.300	18.907	–	–	155 ± 12	187 ± 9	202 ± 20	205 ± 24	180 ± 20	
NGC55-RSG71	00:15:56.900	−39:15:27.50	20.401	18.559	–	–	197 ± 11	214 ± 11	320 ± 16[c]	-476 ± 42[c]	206 ± 12	
NGC55-RSG73	00:15:57.710	−39:15:41.50	20.489	18.411	–	–	161 ± 7	178 ± 6	136 ± 35	176 ± 19	171 ± 11	

[a] Ground-based data from the Araucaria Project Pietrzyński et al. (2006), with typical photometric uncertainty 0.075 and 0.016 mag in V and I bands respectively.
[b] HST ANGST photometry from Dalcanton et al. (2009), with typical errors 0.12, 0.13 in F606W and F814W bands respectively.
[c] Value excluded from average for target.

Table 6.2 *NGC 55 observing log*

Date	Seeing Conditions (*arcsec*)	Airmass	Number of Exposures	Notes
14-10-2013	0.″8–1.″2	1.0–1.8	6 × 600s	Observed by author
16-10-2013	0.″8–1.″2	1.0–1.3	14 × 600s	Observed by author
14-09-2014	0.″4–2.″2	1.0–1.9	24 × 600s	Back-up observations
15-09-2014	1.″1–1.″6	1.1–1.5	12 × 600s	Back-up observations

As back-up observations, this field was observed on two nights in August 2014. Therefore, this field was observed on four different nights: 14-10-2013, 16-10-2013, 14-09-2014 and 15-10-2014 as detailed by Table 6.2. The observations on each night consisted of science exposures (O) with sky offset exposures (S) interleaved in an O, S, O observing pattern, where each exposure is 600 s.

In addition, on each night a standard set of KMOS calibration files was obtained as well as standard star observations on each night. In October 2013, HIP 3820 (B8 V; Houk, 1978) was observed using the 24-arm telluric template (KMOS_spec_acq_stdstarscipatt). However, on 14-10-2013, this OB was interrupted and several of the IFUs (particularly on detector two) were not observed with the 24-arm recipe: this OB was not repeated.

In August 2014 the 3-arm telluric template (KMOS_spec_cal_stdstar) was observed as opposed to the full 24-arm template. However, on both of these nights both HIP 3820 and HIP 18926 (B3 V; Houk & Smith-Moore, 1988) were observed as a standard star.

The quality of the observations taken on each night varies significantly. The first set of observations (14-09-2013) were taken in excellent conditions where the seeing conditions were stable with good transparency. As one would expect with back-up observations the conditions were not so idyllic. On both nights where this field was observed as a back-up target, the conditions were varying significantly throughout the night with patchy, sometimes significant, cloud coverage.

These differences in the quality of the data and in the actual execution of the observations must all be taken into account when the data is reduced. In addition to differences in the observations arising from the conditions, there are also differences as a result of the time between the observations. Table 6.3 shows the mean measured resolution and resolving power, at the appropriate rotator angles, for each night where the NGC 55 data were taken. This table shows that the resolution can vary significant between each night, particularly on detector

Table 6.3 *Measured velocity resolution and resolving power across each detector.*

Date	Det.	IFUs	Ne λ1.17700 μm		Ar λ1.21430 μm	
			FWHM (km s^{-1})	R	FWHM (km s^{-1})	R
14-10-2013	1	1-8	95.48 ± 2.42	3140 ± 80	90.71 ± 2.09	3305 ± 76
	2	9-16	88.67 ± 1.67	3381 ± 64	86.35 ± 1.84	3472 ± 74
	3	17-24	82.89 ± 1.81	3617 ± 79	80.56 ± 2.11	3721 ± 97
16-10-2013	1	1-8	95.48 ± 2.46	3140 ± 81	90.78 ± 2.12	3302 ± 77
	2	9-16	88.91 ± 1.66	3371 ± 63	86.30 ± 1.85	3473 ± 74
	3	17-24	82.96 ± 2.14	3612 ± 76	80.77 ± 2.14	3712 ± 98
14-09-2015	1	1-8	84.18 ± 1.93	3561 ± 82	81.76 ± 2.15	3667 ± 96
	2	9-16	87.00 ± 1.69	3446 ± 67	84.67 ± 1.93	3541 ± 81
	3	17-24	97.14 ± 1.88	3086 ± 60	94.85 ± 2.01	3161 ± 67
15-09-2014	1	1-8	82.55 ± 1.96	3632 ± 86	80.41 ± 2.30	3728 ± 106
	2	9-16	88.08 ± 1.78	3404 ± 69	86.03 ± 1.96	3485 ± 80
	3	17-24	98.04 ± 1.91	3058 ± 59	96.74 ± 2.05	3099 ± 66

three where the mean resolving power changes by a factor of 1/5. Therefore, this must be taken into consideration when combining exposures on different nights. This is solved by using a simple Gaussian filter (as first described in Chapter 3) to degrade the resolution of the spectra to that of the lowest resolution spectrum within the data set. For example, all spectra for a star in IFU 1 would be degraded to a resolution of 3302 (see Table 6.3) before being combined into a master spectrum for the four nights.

The observations were reduced using the recipes provided by the Software Package for Astronomical Reduction with KMOS (SPARK; Davies, R. I. et al., 2013). The standard KMOS/esorex routines were used to calibrate and reconstruct the science and standard-star data cubes as outlined by Davies, R. I. et al. (2013), including a correction for the readout column bias as well as enhancing the bad pixel mask following Turner et al. (in prep.). Using the reconstructed data cubes the pipeline was used to extract science and sky spectra in a consistent way for all exposures.

Sky subtraction was performed using the ESO SKYCORR package (Noll et al., 2014). SKYCORR is an instrument independent tool that applies a scaling to a sky spectrum, given a pair of observed and sky spectra in order to more accurately match the sky lines in the observed spectrum and hence, provide a more accurate sky subtraction. This works by adapting the reference sky spectrum to correct

for differences as a result of temporal and spatial airglow variability This software is specifically designed for observations at Cerro Paranal and has been shown to be an effective tool for various different science goals (e.g. Noll et al., 2014; Gazak et al., 2015; Fossati et al., 2016; La Barbera et al., 2016).

Telluric correction is performed on each sky subtracted spectrum (before combination) using the method described in full in Chapter 5. Briefly, additional corrections are made to the standard KMOS/esorex method of telluric correction by correcting for potential offsets between the wavelength solutions of the science and telluric spectra using a iterative cross-correlation approach. In addition, a simple scaling is applied to the telluric spectrum in order to more accurately match the telluric absorption in the science spectrum. Once these addition corrections have been implemented, I divide the science spectrum by the telluric using only the 1.16–1.21 μm region.

As mentioned above, during each night of observing at least one telluric standard-star was observed. Where multiple telluric spectra were available for a single science spectrum, all appropriate telluric spectra were used to apply the telluric correction. The spectra resulting from these corrections are then compared visually and the spectrum producing the fewest residuals is selected. There were instances where multiple spectra were of equal quality, in these cases both spectra were used in the combination process.

To combine the fully calibrated and corrected spectra on each night, I first degrade the spectral resolution of all spectra to the lowest resolution of the set as defined by Table 6.3. Once all spectra are at a constant resolution I correct for any differences in the wavelength solution by using an iterative cross-correlation approach, where the spectra are all corrected to the rest frame of a single "reference" spectrum. The choice of the reference spectrum is important as if one selected a poor quality reference spectrum with strong sky- or telluric-correction residuals, this could result in an alignment of the residuals which would amplify these features when finally combined. To avoid this, the highest-quality spectrum for each target is selected as the reference spectrum. In practise, this was typically frame four of the night of 16-09-2013.

This procedure mainly corrects for differences in the wavelength solution from different nights as typically on an individual night, particularly in the case of 14-09-2013 and 16-09-2013, there are not significant differences in the wavelength solution. Once this correction is implemented all spectra are combined using

a simple median combine. This simple method is preferred to something more sophisticated as there were significant sky- and telluric-correction residuals present in many of these spectra which are found to be most effectively extinguished using a median combination.

6.5 Results and Discussion

6.5.1 Radial Velocities

Radial velocities are measured using the method described first in Chapter 4 where radial velocities are measured using several strong spectral features within the 1.16–1.21 μm region. Each of these spectral features is independently used to measure a radial velocity where the value quoted is the average of these measurements and the uncertainties are defined by the standard deviation of the measurements. This method is known to work well on stellar spectra from KMOS (Lapenna et al., 2015; Patrick et al., 2015, 2016).

Velocities are measured by combining frames from each night individually using the standard KMOS/esorex routines, rather than the method described above. Estimated radial velocities from each KMOS pointing are listed in Table 6.1 alongside the average radial velocity for each target, where any significantly discrepant measurement has been excluded as a result of residuals in the spectrum perturbing the fit (marked by note c in Table 6.1). This is a particular problem on the night of 14-09-2014 where 7/20 velocity measurements were excluded. Uncertainties quoted on the average are the standard deviation of the measurements on each night. Three targets (NGC55-RSG22, NGC55-RSG36 and NGC55-RSG60) have been excluded from this average based on their unreliable radial-velocity estimates. Given the significant variability in these measurements on each night, an assessment on membership to NGC 55 is impossible given the current data. Therefore, henceforth, these targets are excluded from the sample.

Comparing the estimated velocities to previous measurements we find good agreement with velocities measured for ∼200 BSGs in NGC 55 in Castro et al. (2008) as well as with measurements of the velocity from the H I gas (Puche, Carignan & Wainscoat, 1991). The estimated radial velocities as a function of galactocentric distance are shown in Figure 6.4, where previous measurements are also shown for comparison. The radius at which the surface brightness first

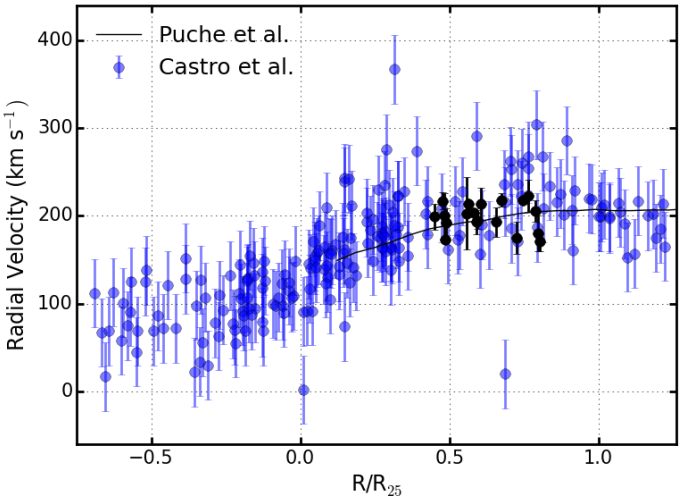

Figure 6.4 *Radial velocities for the KMOS RSGs (black points) shown against projected radius from the centre of NGC 55 as defined by the Two Micron All Sky Survey (2MASS; Skrutskie et al., 2006) scaled by $R_{25} = 16.2 \pm 0.4$ arcmin (de Vaucouleurs et al., 1991). Blue points show data for ∼200 BSGs in NGC 55 from Castro et al. (2008, shown with 50% transparency to highlight densely populated areas) alongside the rotation curve of NGC 55 (black solid line; Puche, Carignan & Wainscoat, 1991).*

reaches 25 mag/arcsec^2 in the B-band (R_{25}; e.g. Schneider, 2015) is shown for scale ($R_{25} = 16.2 \pm 0.4$ arcmin; de Vaucouleurs et al., 1991). We find no evidence for a systematic offset between the measurements of Castro et al. (2008) and those measured in this study. The de-projected radius is calculated by assuming the geometrical model defined by Puche, Carignan & Wainscoat (1991) i.e. with an inclination angle $i = 78\,^{\circ}$and a position angle $\phi = 109\,^{\circ}$.

As the observed data is taken over four different epochs, the variability of each source can be assessed. To assess variability, the variability criteria of Hénault-Brunet et al. (2012) is employed, i.e.

$$\left| \frac{RV_i - \mu}{\sigma_i} \right| > 4.0, \tag{6.1}$$

where RV_i is the radial velocity with an associated uncertainty σ_i measured on an individual night i and μ is the average radial velocity for the target. Using this criteria on all targets finds that none show compelling evidence for variability. This adds strength to the suggestion that observed RSGs are intrinsically single objects as a result of the length of time spent as an RSG in a binary is significantly

decreased (see discussion in Chapter 4).

6.5.2 Stellar Parameters

Stellar parameters are estimated for each target using the J-band analysis technique detailed in Chapter 3. This analyis is used to measure stellar parameters, including overall metallicity – to a precision of ± 0.15 dex at the resolution of KMOS observations with S/N $\geq$ 100. The parameter ranges are given shown in Chapter 3, Table 4.3.

The analysis uses synthetic RSG spectra, extracted from MARCS model atmospheres (Gustafsson et al., 2008), computed with corrections for non-local thermodynamic equilibrium for lines from titanium, iron, silicon and magnesium (Bergemann et al., 2012a, 2013, 2015). The synthetic spectra are compared with observations using the χ-squared statistic and the synthetic spectra are degraded to the resolution and sampling of the observations.

Estimated stellar parameters are listed in Table 6.4 and the best-fit model spectra are shown with the final reduced science spectra in Figure 6.5. Assuming no spatial variations in metallicity the average metallicity of of the sample is -0.36 ± 0.25 dex. This average value compares well to the average metallicity measured using 12 BSGs in NGC 55 from (Castro et al., 2012, -0.4 ± 0.13). These authors find no evidence for spatial variations in metallicity in NGC 55.

Kudritzki et al. (2016) measure metallicities for $\sim$60 BSGs in NGC 55 covering a larger spatial extent. Combining all of the available data sets for BSGs and RSGs yields a metallicity gradient of -0.16 ± 0.05 dex/kpc: the first detected in this galaxy. In order to independently calibrate this gradient with only RSGs would require a larger sample covering the full spatial profile of NGC 55.

Figure 6.6 displays the estimated metallicities shown as a function of the deprojected radial distance from the centre of the galaxy as defined by the Two Micron All Sky Survey (2MASS; Skrutskie et al., 2006). As in Figure 6.4, the deprojected radius is calculated by assuming a geometrical model with an inclination angle $i = 78\,^{\circ}$and a position angle $\phi = 109\,^{\circ}$ (Puche, Carignan & Wainscoat, 1991).

Luminosities have been calculated for the targets using the bolometric corrections of Davies, B. et al. (2013) with the F814W HST bandpass where available, otherwise the ground-based I-band filter has been used. Figure 6.7 shows a H-R

Table 6.4 *Physical parameters determined for the KMOS targets in NGC 55*

Target	IFU	ξ (km s^{-1})	[Z]	log g	$T_{\rm eff}$ (K)	Notes
NGC55-RSG24	10	4.2 ± 0.6	-0.43 ± 0.24	-0.37 ± 0.75	4180 ± 330	
NGC55-RSG25	8	3.2 ± 0.9	-0.53 ± 0.33	0.12 ± 0.36	3460 ± 250	
NGC55-RSG26	4	3.2 ± 0.7	-0.64 ± 0.34	0.12 ± 0.25	3560 ± 280	
NGC55-RSG35	12	4.0 ± 0.6	-0.35 ± 0.26	-0.13 ± 0.24	3750 ± 120	
NGC55-RSG39	14	3.3 ± 0.7	-0.28 ± 0.28	-0.13 ± 0.25	3700 ± 100	
NGC55-RSG43	24	3.7 ± 0.8	-0.27 ± 0.26	0.12 ± 0.98	3960 ± 250	
NGC55-RSG57	1	4.0 ± 0.7	-0.39 ± 0.28	0.10 ± 0.24	3550 ± 270	
NGC55-RSG58	15	3.5 ± 0.7	-0.38 ± 0.27	0.12 ± 0.96	3750 ± 140	
NGC55-RSG65	17	4.2 ± 0.5	-0.25 ± 0.19	0.11 ± 0.97	3750 ± 180	
NGC55-RSG73	19	3.2 ± 0.5	-0.26 ± 0.15	-0.86 ± 0.50	3830 ± 300	

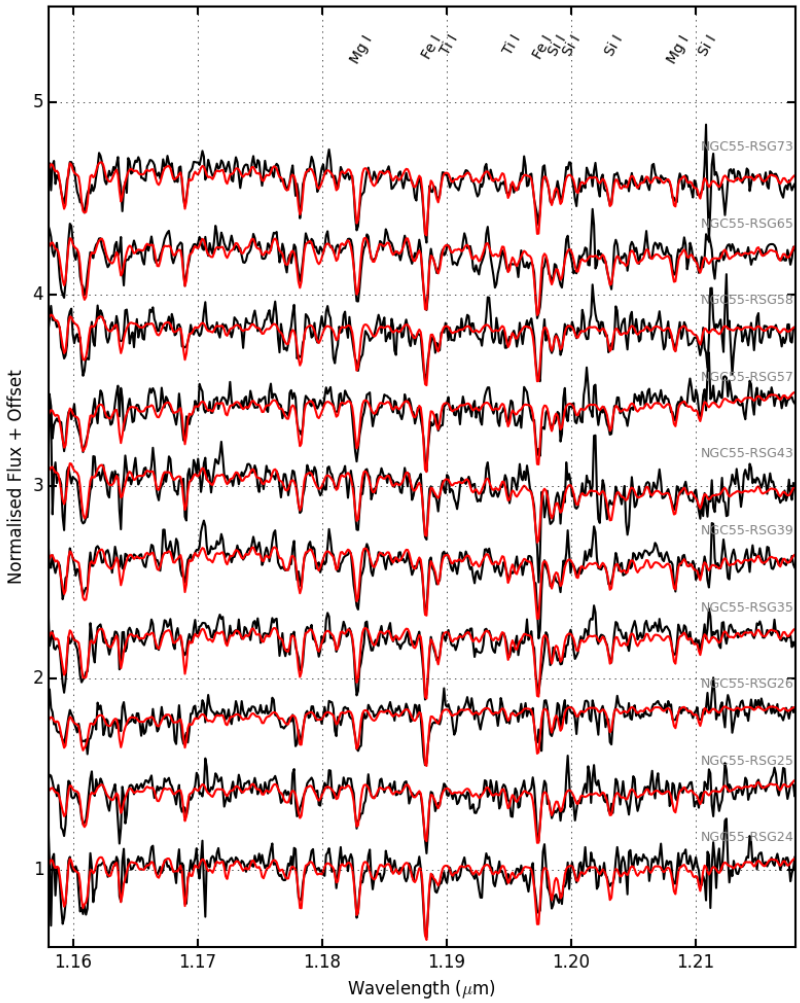

Figure 6.5 *Observed and best-fit model spectra of RSGs in NGC 55 (black and red lines, respectively). The lines used for the analysis, from left-to-right by species, are Fe I $\lambda\lambda$1.188285, 1.197305; Mg I $\lambda\lambda$1.182819, 1.208335; Si I $\lambda\lambda$1.198419, 1.199157, 1.203151, 1.210353; Ti I $\lambda\lambda$1.189289, 1.194954.*

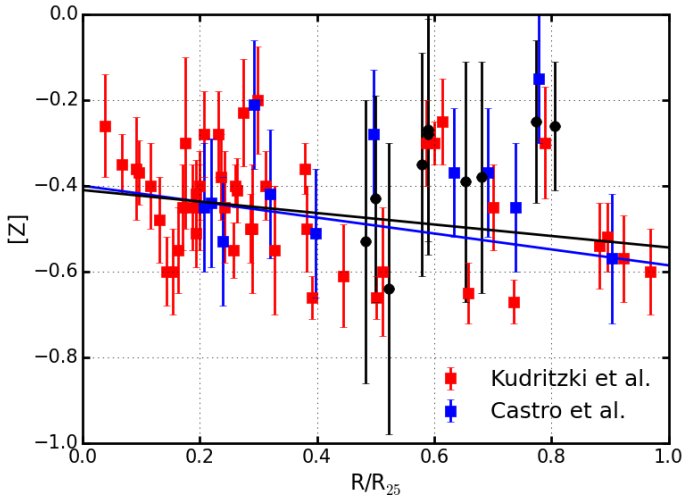

Figure 6.6 *Metallicities for KMOS RSGs (black points) shown against de-projected radius from the centre of NGC 55 as defined by the Two Micron All Sky Survey (Skrutskie et al., 2006) scaled by $R_{25} = 16.18$ arcmin (Karachentsev et al., 2004). The average metallicity of the KMOS RSGs is -0.36 ± 0.25 dex. Results for blue supergiant stars (BSGs) from Kudritzki et al. (2016) and Castro et al. (2012) are shown with red and blue squares respectively. Using a least squares fit to all of these measurements yields a metallicity gradient of -0.16 ± 0.05 dex/kpc (black line). The blue line shows a least squares fit to just the BSG data.*

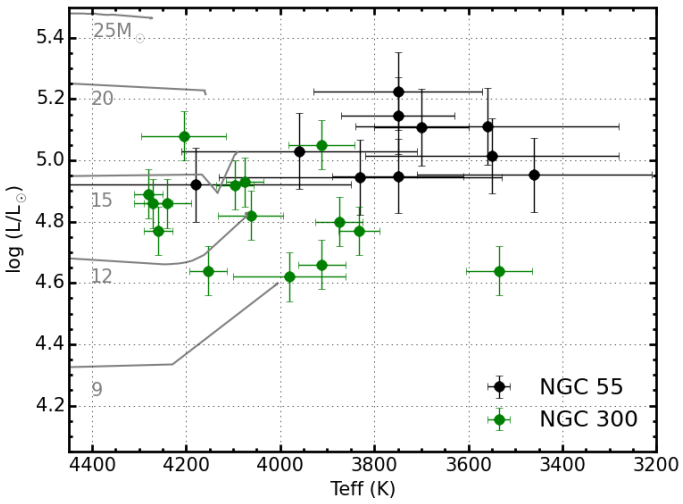

Figure 6.7 *Hertzsprung–Russell diagram for NGC 55. Solid grey lines show SMC-like metallicity evolutionary models including rotation (Georgy et al., 2013). Results from Gazak et al. (2015) in NGC 300 are shown in green for comparison.*

diagram for these targets using the temperatures estimated in Section 6.5 along with SMC-like evolutionary tracks (Georgy et al., 2013). Results for 15 RSGs in NGC 300 (a fellow Sculptor galaxy also at ∼1.9 Mpc) are shown in green on this figure for comparison (Gazak et al., 2015). This appears to show a difference in the temperatures of the RSGs in the sample.

6.6 Conclusions

I have presented multi-epoch near-IR spectroscopic observations of 22 RSGs in the Sculptor Group galaxy NGC 55. Radial velocities are presented and are shown to agree well with previous measurements in this galaxy, where all targets with reliable radial velocity measurements are consistent with membership to NGC 55: confirming their nature as supergiants. Variability is assessed for each target and I find no evidence for variability. A lack of variability is what one would expect from a sample consisting of single stars.

Stellar parameters are estimated for 10 of the highest S/N targets in the sample using the J-band analysis method described in Chapter 3. The average metallicity of the sample is -0.36 ± 0.25, in good agreement with previous results. No evidence is found for spatial variations in metallicity given the present sample, however, we note that this is expected as a result of the combination of the

spatial coverage of the sample and the uncertainties in the metallicity parameter. Luminosities are calculated and are compared with RSGs in NGC 300 (a fellow Sculptor galaxy at ∼1.9 Mpc) where there appears to be slight differences in the average effective temperatures of the two samples.

Chapter 7

Conclusions

7.1 Summary

In this thesis, I have used near-infrared (near-IR) spectroscopic observations to measure the chemical abundance of red supergiant (RSG) stars in different environments within the Local Universe. I have detailed the background theory surrounding the evolution of massive stars and described their pivotal role in shaping the Universe. To make the best use of the extremely luminous nature of RSGs, I have described and detailed the K-band multi-object spectroscopy (KMOS): the only near-IR multi-object spectrograph in the southern hemisphere.

I have developed and tested a grid-based analysis technique, which is used to estimate stellar parameters of RSGs using medium-resolution J-band spectroscopy. I estimate parameters by sampling the posterior probability density function using a maximum-likelihood approach and show that, this technique is not only internally consistent, but is also in good agreement with literature measurements.

In Chapter 4, I measure the chemistry and kinematics of a young massive cluster (YMC) in the Large Magellanic Cloud (LMC): NGC 2100. KMOS spectra of 14 RSGs in NGC 2100 are used, for the first time, to estimate the dynamical properties of this star cluster. This study demonstrates that KMOS can be used to measure velocities of stars in external galaxies to a precision of $<5\,\mathrm{km\ s^{-1}}$, and I place an upper limit on the line-of-sight velocity dispersion (σ_{1D}) of NGC 2100 at $\sigma_{1D} = 3.9\,\mathrm{km\ s^{-1}}$, at the 95% confidence level, where no evidence is found for spatial variations in σ_{1D}. Using this upper limit, the dynamical mass of NGC 2100

has been calculated (assuming virial equilibrium) as $M_{dyn} < 15.2 \times 10^4 M_{\odot}$, consistent with the literature value of the photometric mass for NGC 2100.

The chemistry of NGC 2100 has been estimated using the analysis technique developed in this thesis, where the average present-day metallicity of NGC 2100 is $[Z] = -0.43 \pm 0.10$ dex, which agrees well with previous studies in this cluster and with studies of the young stellar population of the LMC.

The observational properties of the RSGs in NGC 2100 are compared with a star cluster of similar age and mass at Solar-like metallicity. This comparison allows differences in the observational properties of RSGs at different metallicities to be assessed and I show that there appears to be no significant difference between the RSGs in these Solar-like and LMC-like metallicity clusters.

As the RSGs population dominates the infrared light output of a YMC, of a particular age and mass, I combine the RSG spectra to create a simulated integrated-light cluster spectrum of NGC 2100. Using the same analysis technique as for single stars, I demonstrate that the stellar parameters estimated using integrated-light spectroscopy of YMCs are representative of the average parameters of the RSG population within the cluster.

In Chapter 5, KMOS spectroscopy of 18 RSGs in the dwarf irregular galaxy NGC 6822 is presented. The KMOS data used in this chapter was obtained using KMOS science verification (SV) time, before this instrument was released to the general community. This chapter represents the first KMOS study of RSGs and forms the base of which all other studies in this area are built from. In order to characterise the performance of the data reduction, I have reduced and analysed the data using two different methods of telluric correction: the more expensive 24-arm telluric correction and the more efficient three-arm method. Both methods give consistent results and the 3-arm telluric correction is shown to work as effectively (in most cases). However, we caution, in the low signal-to-noise regime, the 24-arm telluric method will give more reliable results.

Stellar parameters for the RSGs in NGC 6822 are calculated using two different analysis techniques and are shown to be in good agreement. The present day metallicity of NGC 6822, from RSGs, is $[Z] = -0.55 \pm 0.13$ dex, which is consistent with previous measurements of the young stellar population in NGC 6822. The data show evidence for a low-significance abundance gradient within NGC 6822 and if real, this would be the first of its kind in a dwarf irregular galaxy. A larger follow-up study is required in order to fully characterise this gradient.

The chemical abundances of the young and old stellar populations, of NGC 6822, are well explained by a simple closed-box chemical evolution model. However, while an interesting result, we note that the closed-box model is unlikely to be a good assumption for this galaxy given its morphology.

The effective temperatures of RSGs are compared in four galaxies using the same analysis technique. These environments span 0.55 dex in metallicity, and no evidence is found for a significant variation in temperature with respect to metallicity. This is in contrast with evolutionary models that, for a similar change in metallicity, produce a change in the temperature of RSGs of up to 450 K. In addition, in this chapter I argue that the observed shift in the spectral type of RSGs (defined at optical wavelengths), with respect to metallicity, does not imply that the temperatures of RSGs is dependent upon metallicity.

In Chapter 6, multi-epoch KMOS spectroscopy is presented of 22 RSGs in the Sculptor Group galaxy, NGC 55. I have measured radial velocities for each epoch and showed that these measurements agree well with previous measurements. All targets with reliable velocities are shown to be consistent with membership of NGC 55. In addition I have assessed the radial-velocity variability of each target and find no evidence for any variable sources, which is consistent with all targets being single objects.

Stellar parameters are estimated for the highest S/N targets and the average metallicity is found to be -0.36 ± 0.25 dex, in good agreement with previous results for blue supergiant (BSG) stars. No evidence is found for spatial variations in metallicity given the present sample, however, I note that this is expected as a result of the combination of the spatial coverage of the sample and the uncertainties in the metallicity parameter.

7.2 Future Projects

As the topic of this thesis explores many different environments and attempts to relate observations, not only to stellar evolution but also, to galaxy evolution in general, there are many future projects that build on the present study. One of the key aims of this thesis has been to develop the use of RSGs as chemical abundance probes in external environments. Having demonstrated the effectiveness of RSGs as useful tools to measure chemical abundances, in a range

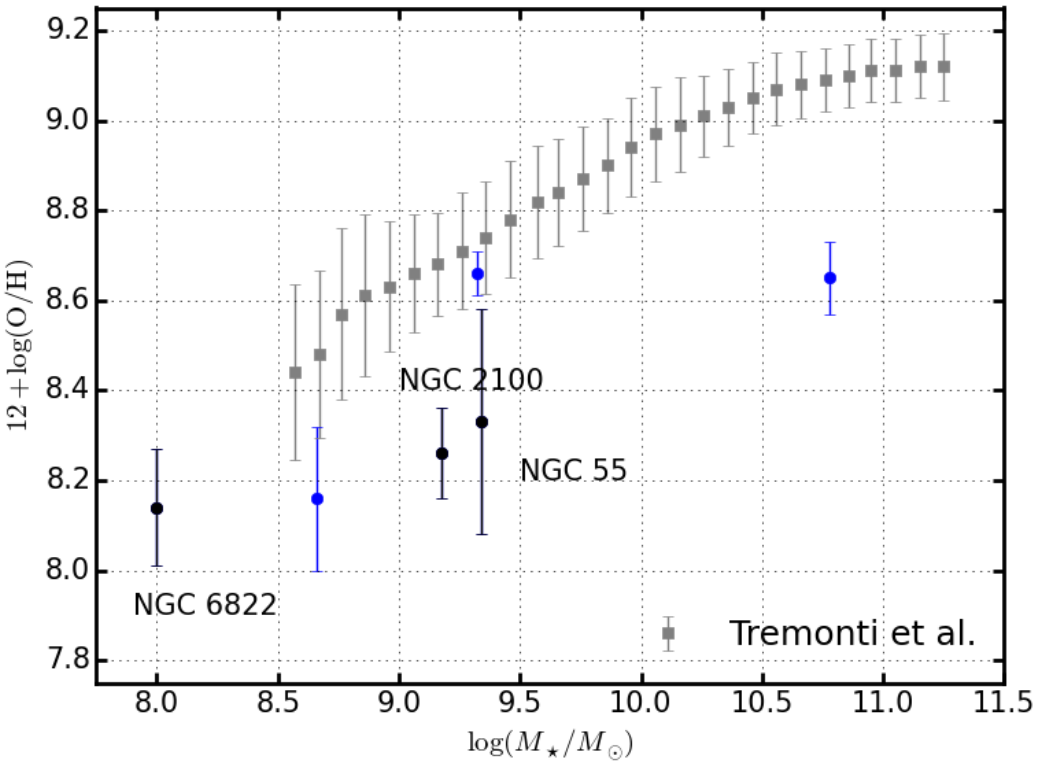

Figure 7.1 *The mass-metallicity relation (MZR) for red supergiant stars (RSGs) in the Local Universe, shown with blue points, where the work included in this thesis is shown with black points. Metallicity measurements are compiled from the Small Magellanic Cloud (Davies et al., 2015), Perseus OB-1 (Gazak et al., 2014b), NGC 300 (Gazak et al., 2015), NGC 2100 (Chapter 4), NGC 6822 (Chapter 5) and NGC 55 (Chapter 6). By introducing the Solar oxygen abundance ratio (12 + log $(O/H)_{\odot}$ = 8.69; Asplund et al., 2009), I compare these results to the local MZR for galaxies at $z \sim 0.1$ (Tremonti et al., 2004). This is the first calibration of the MZR using RSGs. This figure illustrates some of the intriguing differences between the metallicity measurements detailed in this thesis and those of Tremonti et al. (2004), however, to quantitatively assess the calibration of this relationship a larger sample of RSGs in the Local Universe must be obtained.*

of galaxies in low-metallicity environments, I can compile an initial calibration of the mass–metallicity relationship (MZR) using the results presented here.

In Figure 7.1, I present a first-look at the calibration of the MZR in the Local Universe using RSGs as abundances probes in external galaxies. This figure displays results for six galaxies in the Local Universe (blue points) where three of the points have been added by this thesis (black points). In addition, I show the results of Tremonti et al. (2004) who measured the MZR for ∼50 000 SDSS galaxies in the Local Universe ($z \sim 0.1$), and by introducing the Solar oxygen abundance ratio ($12 + \log (O/H)_{\odot} = 8.69$; Asplund et al., 2009), I compare these two results. This figure appears to show an indication of an offset between the metallicity measurements of these two data sets, however, a larger sample of measurements from RSGs is required to quantitatively assess this offset and differences in these relationships. To compare these measurements two critical dependencies must be addressed:

- is the assumption of a constant, solar α/Fe ratio applicable for this set of galaxies?
- does the metallicity measurement depend upon the area of the target galaxy targeted for the measurement?

These are significant issues to take into account, particularly when comparing a large set of galaxies where the metallicity measurement has been estimated using different techniques and instruments. Tremonti et al. (2004) use fibre spectroscopy to estimate abundances, which, depending upon the location of the galaxy in redshift space, covers a significantly different amount of the target galaxy. This must be taken into account to effectively calibration this relationship.

Using RSGs as metallicity indications must take into account the location of the RSGs within the target galaxy and any spatial variations in metallicity. The most obvious drawback of the calibration presented here is the number of target galaxies that RSGs are studied in. To increase this sample size, I am part of a collaboration that aims to measure chemical abundances from RSGs, using techniques developed in this study, with KMOS observations of RSGs in 13 galaxies. This will allow us to provide a full, independent calibration of the MZR using RSGs in the Local Universe. The observational campaign has been partially successful through use of KMOS guaranteed time observations (GTO) and SV

data, however, the core proposal for this project was only partially completed in 2015 as a result of poor weather during observing. I am part of the team that has re-applied for time to observe the final three galaxies in this sample. When complete, this project will allow for the most precise determination of the MZR to date, and will provide a foundation for calibration of future extragalactic abundance work.

In addition to the calibration of the MZR, which was known to be a project which would be greater than the work of one PhD thesis, something that was an unexpected result of this thesis has been the result that there appears to exist no significant variation in the temperature of RSGs with respect to metallicity. In Figure 7.2, I compile all observations of RSGs analysed using the same approach as the one described in this thesis. This figure shows effective temperature as a function of the metallicity, estimated using the J-band analysis technique, for 81 targets in seven different metallicity environments ranging from Solar, in Perseus OB-1, to the low-metallicity environment of NGC 6822, spanning a range of 0.55 dex in metallicity. The mean of the distribution is 3990 K with a standard deviation of 150 K.

From this figure I find no clear evidence for a temperature variation with respect to metallicity. However, to quantify this fully, a larger sample of RSGs must be studied in a range of different metallicity environments and any systematic effects must be correctly taken account of. Large spiral galaxies are star-forming environments that typically contain hundreds of RSGs and large spatial variations in abundances. Therefore, a study of a (near) complete population of RSGs in a nearby grand design spiral galaxy e.g. M 31 or NGC 300, would be a good starting point to quantitatively assess this interesting result.

Selecting a complete sample of RSGs is essential to quantify potential systematic effects that are inherent to this result. This is because RSGs are typically selected using the optical or near-IR CMD where RSGs of significantly different temperatures could be blended with galactic contaminants. This would introduce a significant bias into this result and could contribute to the lack of variation in the effective temperatures of RSGs.

If this result is real, a possible explanation could be that in stellar evolutionary models the temperature of RSGs is affected by the choice of the convective mixing length parameter α_{MLT}, which is usually fixed at the Solar value ($\alpha = 2.0$). A dependence of α on the metallicity of the star could account for the lack of

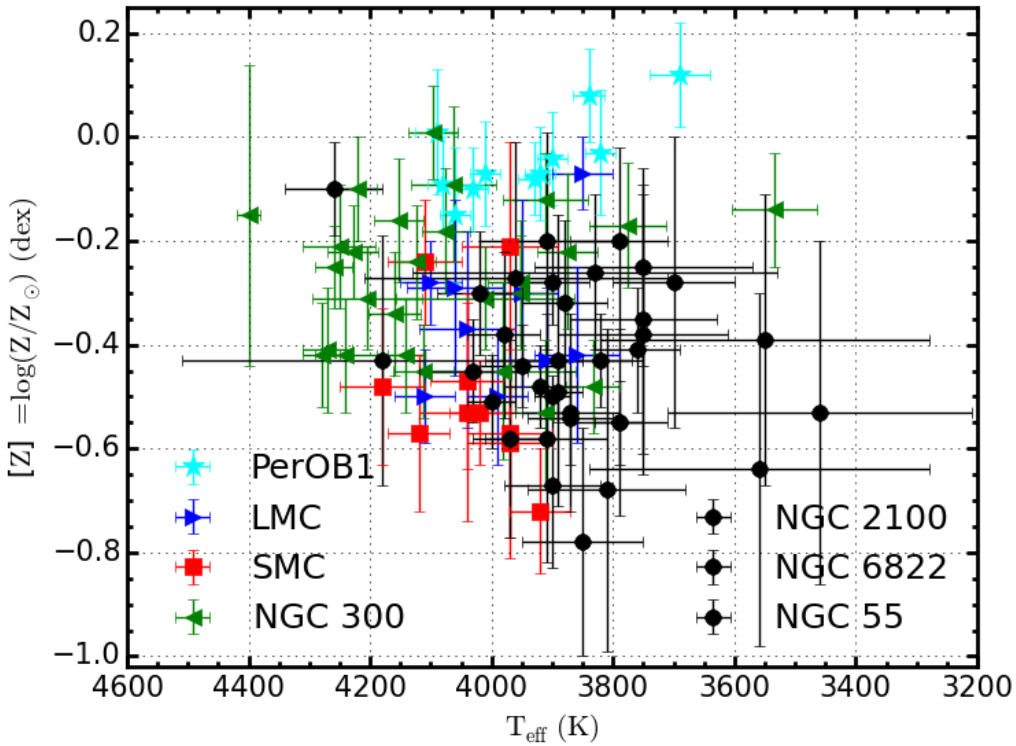

Figure 7.2 *Effective temperatures as a function of metallicity for five different data sets using the J-band analysis technique. There appears to be no significant variation in the temperatures of RSGs over a range of 0.55 dex. These results are compiled from Perseus OB-1 (a Galactic RSG cluster; cyan; Gazak et al., 2014b), the LMC and SMC (blue and red points respectively; Davies et al., 2015), NGC 300 (green points; Gazak et al., 2015), NGC 2100 (Chapter 4), NGC 6822 (Chapter 5) and NGC 55 (Chapter 6). The work included in this thesis is shown with black points.*

observed temperatures of RSGs.

In Chapter 5 I present low-significance evidence for a metallicity gradient within NGC 6822. Previously in the literature there have been claims for a weak radial metallicity gradient however these claims have been hampered by a lack of precision in metallicity and/or small sample size. By targeting all candidate RSGs within NGC 6822 using KMOS GTO in April 2016, I will measure metallicities for ∼60 RSG candidates across the full spatial extent of NGC 6822 (see Chapter 5, Figure 5.3). These follow-up observations will allow me to definitively quantify the spatial distribution of metallicity within NGC 6822. This is an important result to quantify as a radial metallicity gradient would be direct evidence for a disk structure in NGC 6822.

In addition to follow-up spectroscopy in NGC 6822, our collaboration has re-submitted for KMOS spectroscopy of an additional one field in NGC 55 to extend the spatial profile covered in this galaxy. By estimating metallicities for an additional ∼20 targets in the disk of NGC 55 I will be able to more rigorously quantify the abundance gradient in this galaxy with the aim to independently calibrate the metallicity gradient measured from BSGs (Kudritzki et al., 2016). In addition to this, by measuring temperatures of the RSGs more accurately in NGC 55 I will be able to quantify the potential offset in temperatures between this data set and that of NGC 300.

In Chapter 4, I presented the first determination of (an upper limit to) the dynamical mass of NGC 2100 as well the unresolved line-of-sight velocity dispersion for this cluster. By obtaining higher resolution spectroscopy of a large sample of stars within this star cluster one could measure the velocity dispersion profile and resolve the line-of-sight velocity dispersion in this cluster. One of my unanswered questions from the study presented in Chapter 4 is: will this star cluster survive or dissolve in the future? By more accurately determining the mass and velocity dispersion profile of this cluster, this question could be resolved.

In addition to these areas of study mentioned above, I am also interested in further developing the analysis technique presented in Chapter 3. Studies in this area may include fitting for the [α/Fe] parameter (rather assuming Solar-like values), an important indicator of stellar evolution and in particular how this parameter depends upon metallicity. Expanding the wavelength range used to estimate stellar parameters and updating the line list would allow one to estimate

individual elemental abundances as well as overall metallicity. A potentially promising wavelength range to extend this technique is the $\sim$1.0 μm region.

Another interesting avenue to explore with this analysis technique would be to expand the parameter space of the model grid to apply this technique to other cool stars e.g. Cepheid variables and red giant stars.

Finally, great progress has been made in recent years using tools which aid the data reduction process of near-IR spectroscopy, e.g. MOLECFIT, SKYCORR. As near-IR spectroscopy becomes more important in our understanding of astrophysics, these tools will become increasingly relied upon to provide accurate and precise corrections (with the added benefit of significantly boosting observational efficiency). In this thesis I have taken the first steps using SKYCORR on KMOS data, where this tool has had great success above what can be achieved neglecting this procedure. In the future, I will supplement this by using MOLECFIT to perform telluric correction with the goal of optimising future observing strategies.

7.3 Closing Remarks

As near-IR observations becomes the weapon of choice for astronomers to study star-forming extra-galactic systems, RSGs are an obvious choice to probe chemical and dynamical structure, owing to their intrinsic brightness at these wavelengths. The European-Extremely Large Telescope and the James Webb Space Telescope will become operational in the near future and these facilities will be specialised for studies in the near-IR. By developing tools with which to analyse near-IR spectra, like the one presented and tested in this thesis, we put ourselves in the best possible position to make best use of the upcoming huge advancement in telescopes and instruments. Facilities, like the ones mentioned above, will certainly provide the community with "unknown, unknowns," and by having a large suite of tools already in place, we can fully exploit these facilities.

RSG research is gaining support on both the theoretical and observational sides and there is still much to learn about these fascinating objects. This thesis scratches the surface of the subject of RSGs and now I hope to delve deeper into it.

Appendix A

Acronyms

2MASS Two Micron All Sky Survey
ACS Advanced camera for surveys
AGB Asymptotic giant branch
ANGST ACS nearby galaxy survey treasury project
BH Black hole
BSG Blue supergiant
CCD Colour–colour diagram (not to be confused with CCD: Charged coupled device; not an acronym used in this thesis)
CCSN Core-collapse supernova
c.g.s Centimetre-gram-second measurement system
CMD Colour–magnitude diagram
CNO Carbon–nitrogen–oxygen
DKF Davies, Kudritzki & Figer (2010)
DSS Digital sky survey
ESO European southern observatory
FoV Field of view
G14 Gazak (2014)
GRB Gamma-ray burst
GTO Guaranteed time observations
H-R Hertzsprung–Russell
HST Hubble space telescope
IFS Integral field spectroscopy
IFU Integral field unit
IR Infrared

ISM Interstellar medium
JWST James Webb space telescope
KMOS *K*-band multi-object spectrograph (see Chapter 2)
LBV Luminous blue variable
LMC Large Magellanic cloud
LTE Local thermodynamic equilibrium (see Chapter 3)
MOSFIRE Multi-object spectrometer for infra-red exploration
MS Main sequence
MZR Mass-metallicity relationship
NGC New general catalogue
NS Neutron star
OB Observing block
OSIRIS Optical system for imaging and low-intermediate-resolution integrated spectroscopy
PISN Pair instability supernova
PSF Point spread function
RSG Red supergiant
RSGC Red supergiant cluster
SC Schönberg–Chandrasekhar
SED Spectral energy distribution
SDSS Sloan digital sky survey
SMC Small Magellanic cloud
SN Supernova
S/N Signal-to-noise ratio
SPARK Software package for astronomical reduction with KMOS
SV Science verification
VLT Very large telescope
WLT Wolf-Lundmark-Melotte
WR Wolf-Rayet
YMC Young massive cluster

Bibliography

Abbott B. P. et al., 2016, Physical Review Letters, 116, 061102

Aerts C., Rogers T. M., 2015, ApJ, 806, L33

Allington-Smith J., 2006, New Astronomy Reviews, 50, 244

Andrae R., Schulze-Hartung T., Melchior P., 2010, ArXiv e-prints

Andrews B. H., Martini P., 2013, ApJ, 765, 140

Asplund M., Grevesse N., Sauval A. J., Scott P., 2009, ARA&A, 47, 481

Bacon R. et al., 1995, A&AS, 113, 347

Ball W. H., Tout C. A., Żytkow A. N., 2012, MNRAS, 421, 2713

Battinelli P., Demers S., Kunkel W. E., 2006, A&A, 451, 99

Beasor E. R., Davies B., 2016, MNRAS

Bergemann M., Kudritzki R.-P., Gazak Z., Davies B., Plez B., 2015, ApJ, 804, 113

Bergemann M., Kudritzki R.-P., Plez B., Davies B., Lind K., Gazak Z., 2012a, ApJ, 751, 156

Bergemann M., Kudritzki R.-P., Würl M., Plez B., Davies B., Gazak Z., 2013, ApJ, 764, 115

Bergemann M., Lind K., Collet R., Magic Z., Asplund M., 2012b, MNRAS, 427, 27

Bestenlehner J. M. et al., 2011, A&A, 530, L14

Blum R. D. et al., 2006, AJ, 132, 2034

Böhm-Vitense E., 1958, ZAp, 46, 108

Böhm-Vitense E., 1989, Introduction to stellar astrophysics. Vol. 2. Stellar atmospheres.

Böhm-Vitense E., 1992, Introduction to stellar astrophysics. Volume 3. Stellar structure and evolution. Cambridge University Press

Bonnell I. A., Bate M. R., Clarke C. J., Pringle J. E., 2001, MNRAS, 323, 785

Bonnell I. A., Clark P., Bate M. R., 2008, MNRAS, 389, 1556

Bovy J., Rix H.-W., 2013, ApJ, 779

Boyer M. L. et al., 2015, ApJ, 800, 51

Bresolin F., Gieren W., Kudritzki R.-P., Pietrzyński G., Urbaneja M. A., Carraro G., 2009, ApJ, 700, 309

Bressert E. et al., 2012, A&A, 542, A49

Britavskiy N. E., Bonanos A. Z., Mehner A., Boyer M. L., McQuinn K. B. W., 2015, A&A, 584, A33

Britavskiy N. E., Bonanos A. Z., Mehner A., García-Álvarez D., Prieto J. L., Morrell N. I., 2014, A&A, 562, A75

Brott I. et al., 2011, A&A, 530, A115

Burrows A., 2013, Reviews of Modern Physics, 85, 245

Burrows A. et al., 1997, ApJ, 491, 856

Cabrera-Ziri I., Bastian N., Davies B., Magris G., Bruzual G., Schweizer F., 2014, MNRAS, 441, 2754

Cantiello M. et al., 2009, A&A, 499, 279

Castro N. et al., 2008, A&A, 485, 41

Castro N. et al., 2012, A&A, 542, A79

Chabrier G., Baraffe I., 2000, ARA&A, 38, 337

Charlot S., Longhetti M., 2001, MNRAS, 323, 887

Chiavassa A. et al., 2011, A&A, 528, A120

Ciardi B., Ferrara A., 2005, Space Sci. Rev., 116, 625

Cioni M.-R. L. et al., 2011, A&A, 527, A116

Cioni M.-R. L., Girardi L., Marigo P., Habing H. J., 2006, A&A, 452, 195

Cioni M.-R. L. et al., 2014, A&A, 562, A32

Clark J. S. et al., 2009, A&A, 498, 109

Clark J. S., Negueruela I., González-Fernández C., 2014, A&A, 561, A15

Comerón F., Pasquali A., 2005, A&A, 430, 541

Conselice C. J., 2014, ARA&A, 52, 291

Content R., 1997, in Society of Photo-Optical Instrumentation Engineers (SPIE) Conference Series, Vol. 2871, Optical Telescopes of Today and Tomorrow, Ardeberg A. L., ed., pp. 1295–1305

Crowther P., 2012, Astronomy and Geophysics, 53, 040000

Crowther P. A., 2007, ARA&A, 45, 177

Crowther P. A., Schnurr O., Hirschi R., Yusof N., Parker R. J., Goodwin S. P., Kassim H. A., 2010, MNRAS, 408, 731

Cullen F., 2014, PhD thesis, Institute for Astronomy, University of Edinburgh

Cullen F., Cirasuolo M., McLure R. J., Dunlop J. S., Bowler R. A. A., 2014, MNRAS, 440, 2300

Cunha K., Sellgren K., Smith V. V., Ramirez S. V., Blum R. D., Terndrup D. M., 2007, ApJ, 669, 1011

Cunha K. et al., 2015, ApJ, 798, L41

Currie T. et al., 2010, ApJS, 186, 191

Dalcanton J. J. et al., 2009, ApJS, 183, 67

Danchi W. C., Bester M., Degiacomi C. G., Greenhill L. J., Townes C. H., 1994, AJ, 107, 1469

Davidge T. J., 2005, ApJ, 622, 279

Davies B., Kudritzki R.-P., Figer D. F., 2010, MNRAS, 407, 1203

Davies B., Kudritzki R.-P., Gazak Z., Plez B., Bergemann M., Evans C., Patrick L., 2015, ApJ, 806, 21

Davies B., Origlia L., Kudritzki R.-P., Figer D. F., Rich R. M., Najarro F., 2009a, ApJ, 694, 46

Davies B., Origlia L., Kudritzki R.-P., Figer D. F., Rich R. M., Najarro F., Negueruela I., Clark J. S., 2009b, ApJ, 696, 2014

Davies, B., Figer D. F., Kudritzki R.-P., MacKenty J., Najarro F., Herrero A., 2007, ApJ, 671, 781

Davies, B. et al., 2013, ApJ, 767, 3

Davies, R. I. et al., 2013, A&A, 558, A56

de Blok W. J. G., Walter F., 2000, ApJ, 537, L95

de Blok W. J. G., Walter F., 2003, MNRAS, 341, L39

de Blok W. J. G., Walter F., 2006, AJ, 131, 343

de Grijs R., Wicker J. E., Bono G., 2014, AJ, 147, 122

de Vaucouleurs G., 1961, ApJ, 133, 405

de Vaucouleurs G., de Vaucouleurs A., Corwin, Jr. H. G., Buta R. J., Paturel G., Fouqué P., 1991, Third Reference Catalogue of Bright Galaxies. Volume I: Explanations and references. Volume II: Data for galaxies between 0^h and 12^h. Volume III: Data for galaxies between 12^h and 24^h.

de Wit W. J., Testi L., Palla F., Zinnecker H., 2005, A&A, 437, 247

Demers S., Battinelli P., Kunkel W. E., 2006, ApJ, 636, L85

Doherty C. L., Siess L., Lattanzio J. C., Gil-Pons P., 2010, MNRAS, 401, 1453

Doran E. I. et al., 2013, A&A, 558, A134

Efremova B. V. et al., 2011, ApJ, 730, 88

Ekström S. et al., 2012, A&A, 537, A146

Eldridge J. J., 2012, MNRAS, 422, 794

Eldridge J. J., Fraser M., Smartt S. J., Maund J. R., Crockett R. M., 2013, ArXiv e-prints

Eldridge J. J., Izzard R. G., Tout C. A., 2008, MNRAS, 384, 1109

Elias J. H., Frogel J. A., Humphreys R. M., 1985, ApJS, 57, 91

Elson R. A. W., 1991, ApJS, 76, 185

Engelbracht C. W. et al., 2004, ApJS, 154, 248

Evans C. J., Bresolin F., Urbaneja M. A., Pietrzyński G., Gieren W., Kudritzki R.-P., 2007, ApJ, 659, 1198

Evans C. J. et al., 2011a, A&A, 527, A50

Evans C. J., Howarth I. D., 2008, MNRAS, 386, 826

Evans C. J. et al., 2011b, A&A

Evans C. J., van Loon J. T., Hainich R., Bailey M., 2015, A&A, 584, A5

Fan X., Carilli C. L., Keating B., 2006, ARA&A, 44, 415

Feast M. W., 1979, MNRAS, 186, 831

Feldmeier-Krause A. et al., 2015, A&A, 584, A2

Ferguson A. M. N., Wyse R. F. G., Gallagher J. S., 1996, AJ, 112, 2567

Figer D. F., 2005, Nature, 434, 192

Figer D. F., MacKenty J. W., Robberto M., Smith K., Najarro F., Kudritzki R. P., Herrero A., 2006, ApJ, 643, 1166

Foglizzo T. et al., 2015, Publications of the Astron. Soc. of Austrailia, 32, e009

Foreman-Mackey D., Hogg D. W., Lang D., Goodman J., 2013, PASP, 125, 306

Fossati M., Fumagalli M., Boselli A., Gavazzi G., Sun M., Wilman D. J., 2016, MNRAS, 455, 2028

Freytag B., Steffen M., Dorch B., 2002, Astronomische Nachrichten, 323, 213

Fujii M. S., Portegies Zwart S., 2013, MNRAS, 430, 1018

Fukui Y., Kawamura A., 2010, ARA&A, 48, 547

Gazak J. K., 2014, PhD thesis, University of Hawaii

Gazak J. Z., Bastian N., Kudritzki R.-P., Adamo A., Davies B., Plez B., Urbaneja M. A., 2013, MNRAS, 430, L35

Gazak J. Z. et al., 2014a, ApJ, 787, 142

Gazak J. Z., Davies B., Kudritzki R., Bergemann M., Plez B., 2014b, ApJ, 788, 58

Gazak J. Z. et al., 2015, ApJ, 805, 182

Georgy C. et al., 2013, A&A, 558, A103

Giddings J. R., 1981, PhD thesis, , University of London, (1981)

Gieles M., Sana H., Portegies Zwart S. F., 2010, MNRAS, 402, 1750

Gieren W. et al., 2005, The Messenger, 121, 23

Gieren W., Pietrzyński G., Soszyński I., Bresolin F., Kudritzki R.-P., Storm J., Minniti D., 2008, ApJ, 672, 266

González-Fernández C., Dorda R., Negueruela I., Marco A., 2015, A&A, 578, A3

González-Fernández C., Negueruela I., 2012, A&A, 539, A100

Goodman J., Weare J., 2010, Comm. App. Math. Comp. Sci., 1, 65

Gratier P., Braine J., Rodriguez-Fernandez N. J., Israel F. P., Schuster K. F., Brouillet N., Gardan E., 2010, A&A, 512, A68

Gratton R. G., Carretta E., Bragaglia A., 2012, A&A Rev., 20, 50

Gray R., Corbally C., 2009, Stellar Spectral Classification, 1st edn. Oxford University Press

Groenewegen M. A. T., Sloan G. C., Soszyński I., Petersen E. A., 2009, A&A, 506, 1277

Groh J. H., Meynet G., Ekström S., 2013, ApJ, 550, L7

Gustafsson B., Bell R. A., Eriksson K., Nordlund A., 1975, A&A, 42, 407

Gustafsson B., Edvardsson B., Eriksson K., Jorgensen U. G., Nordlund Å., Plez B., 2008, A&A, 486, 951

Haiman Z., Loeb A., 1997, ApJ, 483, 21

Harper G. M., Brown A., Guinan E. F., 2008, AJ, 135, 1430

Harrison C. M. et al., 2016, MNRAS, 456, 1195

Hayashi C., Hoshi R., 1961, PASJ, 13, 442

Hénault-Brunet V. et al., 2012, A&A, 546, A73

Henyey L., Vardya M. S., Bodenheimer P., 1965, ApJ, 142, 841

Hernández-Martínez L., Peña M., Carigi L., García-Rojas J., 2009, A&A, 505, 1027

Herwig F., 2005, ARA&A, 43, 435

Ho I.-T., Kudritzki R.-P., Kewley L. J., Zahid H. J., Dopita M. A., Bresolin F., Rupke D. S. N., 2015, MNRAS, 448, 2030

Hopkins P. F., Quataert E., Murray N., 2011, MNRAS, 417, 950

Hopkins P. F., Quataert E., Murray N., 2012, MNRAS, 421, 3522

Houk N., 1978, Michigan catalogue of two-dimensional spectral types for the HD stars

Houk N., Smith-Moore M., 1988, Michigan Catalogue of Two-dimensional Spectral Types for the HD Stars. Volume 4, Declinations -26°.0 to -12°.0.

Hummel E., Dettmar R.-J., Wielebinski R., 1986, A&A, 166, 97

Humphreys R. M., 1978, ApJS, 38, 309

Humphreys R. M., 1979, ApJ, 231, 384

Humphreys R. M., 2013, in EAS Publications Series, Vol. 60, EAS Publications Series, pp. 185–190

Humphreys R. M., Davidson K., 1979, ApJ, 232, 409

Humphreys R. M., Graham J. A., 1986, AJ, 91, 522

Huxor A. P., Ferguson A. M. N., Veljanoski J., Mackey A. D., Tanvir N. R., 2013, MNRAS, 429, 1039

Hwang N., Lee M. G., Lee J. C., Park W.-K., Park H. S., Kim S. C., Park J.-H., 2011, ApJ, 738, 58

Hwang N., Park H. S., Lee M. G., Lim S., Hodge P. W., Kim S. C., Miller B., Weisz D., 2014, ApJ, 783, 49

Janka H.-T., 2012, Annual Review of Nuclear and Particle Science, 62, 407

Jasniewicz G., Thevenin F., 1994, A&A, 282, 717

Karachentsev I. D. et al., 2003, A&A, 404, 93

Karachentsev I. D., Karachentseva V. E., Huchtmeier W. K., Makarov D. I., 2004, AJ, 127, 2031

Kausch W. et al., 2015, A&A, 576, A78

Kennicutt R. C., Evans N. J., 2012, ARA&A, 50, 531

Kennicutt, Jr. R. C., 1998, ARA&A, 36, 189

Kervella P., Le Bertre T., Perrin G., eds., 2013, EAS Publications Series, Vol. 60, Betelgeuse Workshop 2012

Kewley L. J., Ellison S. L., 2008, ApJ, 681, 1183

King I. R., 1966, AJ, 71, 64

Kippenhahn R., Weigert A., Weiss A., 2012, Stellar Structure and Evolution

Kirby E. N., Cohen J. G., Guhathakurta P., Cheng L., Bullock J. S., Gallazzi A., 2013, ApJ, 779, 102

Komiyama Y. et al., 2003, ApJ, 590, L17

Koribalski B. S. et al., 2004, AJ, 128, 16

Kraus S. et al., 2010, Nature, 466, 339

Kudritzki R., Urbaneja M., Castro N., Ho I., Bresolin F., Gieren W., Pietrzynski G., Przybilla N., 2016, ArXiv e-prints

Kudritzki R.-P., 2010, Astronomische Nachrichten, 331, 459

Kudritzki R.-P., Ho I.-T., Schruba A., Burkert A., Zahid H. J., Bresolin F., Dima G. I., 2015, MNRAS, 450, 342

Kudritzki R.-P., Urbaneja M. A., Bresolin F., Przybilla N., Gieren W., Pietrzyński G., 2008, ApJ, 681, 269

Kudritzki R.-P., Urbaneja M. A., Gazak Z., Bresolin F., Przybilla N., Gieren W., Pietrzyński G., 2012, ApJ, 747, 15

La Barbera F., Vazdekis A., Ferreras I., Pasquali A., Cappellari M., Martín-Navarro I., Schönebeck F., Falcón-Barroso J., 2016, MNRAS, 457, 1468

Lada C. J., Lada E. A., 2003, ARA&A, 41, 57

Langer N., 2012, ARA&A, 50, 107

Langer N., El Eid M. F., Baraffe I., 1989, A&A, 224, L17

Langer N., Maeder A., 1995, A&A, 295, 685

Lanz T., Hubeny I., 2003, ApJS, 146, 417

Lapenna E., Origlia L., Mucciarelli A., Lanzoni B., Ferraro F. R., Dalessandro E., Valenti E., Cirasuolo M., 2015, ApJ, 798, 23

Lardo C., Davies B., Kudritzki R.-P., Gazak J. Z., Evans C. J., Patrick L. R., Bergemann M., Plez B., 2015, ApJ, 812, 160

Lawrence A., 2014, Astronomical Measurement: A Concise Guide

Lee H., Skillman E. D., Venn K. A., 2006, ApJ, 642, 813

Lequeux J., Peimbert M., Rayo J. F., Serrano A., Torres-Peimbert S., 1979, A&A, 80, 155

Letarte B., Demers S., Battinelli P., Kunkel W. E., 2002, AJ, 123, 832

Levesque E. M., Massey P., 2012, AJ, 144, 2

Levesque E. M., Massey P., Olsen K. A. G., Plez B., Josselin E., Maeder A., Meynet G., 2005, ApJ, 628, 973

Levesque E. M., Massey P., Olsen K. A. G., Plez B., Meynet G., Maeder A., 2006, ApJ, 645, 1102

Loeb A., 2016, ApJ, 819, L21

Luhman K. L., 2012, ARA&A, 50, 65

Mackey A. D., Gilmore G. F., 2003, MNRAS, 338, 85

Maeder A., Meynet G., 2001, A&A, 373, 555

Magdis G. E. et al., 2016, MNRAS, 456, 4533

Maiolino R. et al., 2008, A&A, 488, 463

Massey P., 1998, ApJ, 501, 153

Massey P., 2003, AR&A, 41, 15

Massey P., 2013, arXive e-prints

Massey P., Olsen K. A. G., 2003, AJ, 126, 2867

Massey P., Olsen K. A. G., Hodge P. W., Jacoby G. H., McNeill R. T., Smith R. C., Strong S. B., 2007, AJ, 133, 2393

Massey P., Olsen K. A. G., Hodge P. W., Strong S. B., Jacoby G. H., Schlingman W., Smith R. C., 2006, AJ, 131, 2478

McConnachie A. W., 2012, AJ, 144, 4

McKee C. F., Ostriker E. C., 2007, ARA&A, 45, 565

McLaughlin D. E., van der Marel R. P., 2005, ApJS, 161, 304

Mel'Nik A. M., Efremov Y. N., 1995, Astronomy Letters, 21, 10

Méndez-Abreu J. et al., 2011, PASP, 123, 1107

Messineo M., Menten K. M., Churchwell E., Habing H., 2012, A&A, 537, A10

Meynet G., Georgy C., Hirschi R., Maeder A., Massey P., Przybilla N., Nieva M.-F., 2011, Bulletin de la Societe Royale des Sciences de Liege, 80, 266

Meynet G., Maeder A., 2000, A&A, 361, 101

Miller B. W., Whitmore B. C., Schweizer F., Fall S. M., 1997, AJ, 114, 2381

Muschielok B. et al., 1999, A&A, 352, L40

Negueruela I., González-Fernández C., Marco A., Clark J. S., 2011, A&A, 528, A59

Negueruela I., González-Fernández C., Marco A., Clark J. S., Martínez-Núñez S., 2010, A&A, 513, A74

Neugent K. F., Massey P., Skiff B., Meynet G., 2012, ApJ, 749, 177

Newton I., 1704, Opticks: or, a Treatise of the reflexions, refractions, inflexions and colours of light. Also two treatises of the species and magnitude of curvilinear figures. London

Niederhofer F., Hilker M., Bastian N., Silva-Villa E., 2015, A&A, 575, A62

Nieva M. F., Przybilla N., 2007, A&A, 467, 295

Nieva M.-F., Przybilla N., 2012, A&A, 539, A143

Nikolaev S., Weinberg M. D., 2000, ApJ, 542, 804

Noll S., Kausch W., Kimeswenger S., Barden M., Jones A. M., Modigliani A., Szyszka C., Taylor J., 2014, A&A, 567, A25

Pagel B. E. J., Edmunds M. G., Smith G., 1980, MNRAS, 193, 219

Parker R. J., Goodwin S. P., 2007, MNRAS, 380, 1271

Parry I. R., Gray P. M., 1986, in Society of Photo-Optical Instrumentation Engineers (SPIE) Conference Series, Vol. 627, Instrumentation in astronomy VI, Crawford D. L., ed., pp. 118–124

Parviainen H., Aigrain S., Thatte N., Barstow J. K., Evans T. M., Gibson N., 2015, MNRAS, 453, 3875

Patrick L. R., Evans C. J., Davies B., Kudritzki R.-P., Gazak J. Z., Bergemann M., Plez B., Ferguson A. M. N., 2015, ApJ, 803, 14

Patrick L. R., Evans C. J., Davies B., Kudritzki R.-P., Hénault-Brunet V., Bastian N., Lapenna E., Bergemann M., 2016, MNRAS, 458, 3968

Pettini M., Pagel B. E. J., 2004, MNRAS, 348, L59

Pietrzyński G. et al., 2006, AJ, 132, 2556

Pietrzyński G. et al., 2013, Nature, 495, 76

Plez B., 2010, in Astronomical Society of the Pacific Conference Series, Vol. 425, Hot and Cool: Bridging Gaps in Massive Star Evolution, Leitherer C., Bennett P. D., Morris P. W., Van Loon J. T., eds., p. 124

Poelarends A. J. T., Herwig F., Langer N., Heger A., 2008, ApJ, 675, 614

Points S. D., Chu Y. H., Kim S., Smith R. C., Snowden S. L., Brandner W., Gruendl R. A., 1999, ApJ, 518, 298

Portegies Zwart S. F., McMillan S. L. W., Gieles M., 2010, ARA&A, 48, 431

Pritchet C. J., Schade D., Richer H. B., Crabtree D., Yee H. K. C., 1987, ApJ, 323, 79

Przybilla N., 2002, PhD thesis, Munich University Observatory, Ludwig-Maximilian-University Munich

Puche D., Carignan C., Wainscoat R. J., 1991, AJ, 101, 447

Rappenglück M., 2003, Uppsala Astronomical Observatory Reports, 59, 51

Rayleigh L., 1880, MNRAS, 40, 254

Reetz J., 1999, PhD thesis, LMU, Munich

Richards A. M. S., 2013, in EAS Publications Series, Vol. 60, EAS Publications Series, pp. 207–217

Richer M. G., McCall M. L., 1995, ApJ, 445, 642

Rieke G. H., Lebofsky M. J., 1985, ApJ, 288, 618

Robertson J. W., 1974, A&AS, 15, 261

Robinson B. J., van Damme K. J., 1964, in IAU Symposium, Vol. 20, The Galaxy and the Magellanic Clouds, Kerr F. J., ed., p. 276

Saio H., Georgy C., Meynet G., 2013, ArXiv e-prints

Salaris M., Cassisi S., 2005, Evolution of Stars and Stellar Populations. John Wiley & Sons Ltd

Sana H. et al., 2012, ArXiv e-prints

Sanders R. L. et al., 2015, ApJ, 799, 138

Schaller G., Schaerer D., Meynet G., Maeder A., 1992, A&AS, 96, 269

Schlegel D. J., Finkbeiner D. P., Davis M., 1998, ApJ, 500, 525

Schneider P., 2015, Extragalactic Astronomy and Cosmology: An Introduction

Schroder K.-P., Pols O. R., Eggleton P. P., 1997, MNRAS, 285, 696

Schuster M. T., Humphreys R. M., Marengo M., 2006, AJ, 131, 603

Sharples R., 2015, in IAU Symposium, Vol. 309, Galaxies in 3D across the Universe, Ziegler B. L., Combes F., Dannerbauer H., Verdugo M., eds., pp. 11–16

Sharples R. et al., 2013, The Messenger, 151, 21

Sharples R. et al., 2006, New Astron. Rev, 50, 370

Shenoy D. et al., 2016, AJ, 151, 51

Sibbons L. F., Ryan S. G., Cioni M.-R. L., Irwin M., Napiwotzki R., 2012, A&A, 540, A135

Skrutskie M. F. et al., 2006, AJ, 131, 1163

Smartt S. J., 2009, ARA&A, 47, 63

Smette A. et al., 2015, A&A, 576, A77

Smith N., 2014, ARA&A, 52, 487

Smith N., Humphreys R. M., Davidson K., Gehrz R. D., Schuster M. T., Krautter J., 2001, AJ, 121, 1111

Stancliffe R. J., Chieffi A., Lattanzio J. C., Church R. P., 2009, Publications of the Astron. Soc. of Austrailia, 26, 203

Steidel C. C. et al., 2014, ApJ, 795, 165

Sugimoto D., Fujimoto M. Y., 2000, ApJ, 538, 837

Tolstoy E., Irwin M. J., Cole A. A., Pasquini L., Gilmozzi R., Gallagher J. S., 2001, MNRAS, 327, 918

Tremonti C. A. et al., 2004, ApJ, 613, 898

Tubbs E. F., Goss W. C., Cohen J. G., 1982, in Society of Photo-Optical Instrumentation Engineers (SPIE) Conference Series, Vol. 331, Instrumentation in Astronomy IV, p. 289

van de Steene G. C., Jacoby G. H., Praet C., Ciardullo R., Dejonghe H., 2006, A&A, 455, 891

Venn K. A. et al., 2001, ApJ, 547, 765

Vílchez J. M., Iglesias-Páramo J., 1998, ApJ, 508, 248

Vink J. S., 2009, ArXiv e-prints

Webster B. L., Smith M. G., 1983, MNRAS, 204, 743

Wegner M., Muschielok B., 2008, in Society of Photo-Optical Instrumentation Engineers (SPIE) Conference Series, Vol. 7019, Society of Photo-Optical Instrumentation Engineers (SPIE) Conference Series, p. 70190T

Weidner C., Kroupa P., Bonnell I. A. D., 2010, MNRAS, 401, 275

Weiss A., Hillebrandt W., Thomas H.-C., Ritter H., 2004, Cox and Giuli's Principles of Stellar Structure

Weisz D. R., Dolphin A. E., Skillman E. D., Holtzman J., Gilbert K. M., Dalcanton J. J., Williams B. F., 2014, ApJ, 789, 147

Westmeier T., Koribalski B. S., Braun R., 2013, MNRAS, 434, 3511

Whitmore B. C., Schweizer F., 1995, AJ, 109, 960

Williams S. J., Bonanos A. Z., Whitmore B. C., Prieto J. L., Blair W. P., 2015, A&A, 578, A100

Wittkowski M., Hauschildt P. H., Arroyo-Torres B., Marcaide J. M., 2012, A&A, 540, L12

Wolfire M. G., McKee C. F., Hollenbach D., Tielens A. G. G. M., 2003, ApJ, 587, 278

Woo J., Courteau S., Dekel A., 2008, MNRAS, 390, 1453

Wood P. R., Bessell M. S., Fox M. W., 1983, ApJ, 272, 99

Woosley S. E., 2016, ApJ, 824, L10

Woosley S. E., Heger A., Weaver T. A., 2002, Reviews of Modern Physics, 74, 1015

Wright N. J. et al., 2014, MNRAS, 437, L1

Wu S.-W., Bik A., Henning T., Pasquali A., Brandner W., Stolte A., 2014, A&A, 568, L13

Yabe K. et al., 2014, MNRAS, 437, 3647

Yorke H. W., Sonnhalter C., 2002, ApJ, 569, 846

Young T., 1802, Phil. Trans. R. Soc. Lond., 92, 12

Zahid H. J., Kewley L. J., Bresolin F., 2011, ApJ, 730, 137

Zepf S. E., Ashman K. M., English J., Freeman K. C., Sharples R. M., 1999, AJ, 118, 752

Zhang B., Reid M. J., Menten K. M., Zheng X. W., 2012, ApJ, 744, 23

Zinnecker H., Yorke H. W., 2007, ARA&A, 45, 481